Title
First-Principles Studies of Phonons and Electrons in Bulk Thermoelectrics

Author
Xia, Yi

Publication Date
2016

Peer reviewed|Thesis/dissertation

UNIVERSITY OF CALIFORNIA

Los Angeles

First-Principles Studies of Phonons and Electrons in Bulk Thermoelectrics

A dissertation submitted in partial satisfaction

of the requirements for the degree

Doctor of Philosophy in Department of Materials Science and Engineering

by

Yi Xia

2016

ABSTRACT OF THE DISSERTATION

First-Principles Studies of Phonons and Electrons in Bulk Thermoelectrics

by

Yi Xia

Doctor of Philosophy in Department of Materials Science and Engineering

University of California, Los Angeles, 2016

Professor Vidvuds Ozoliņš, Chair

Thermoelectric materials, which enable direct conversion between thermal and electrical energy, provide an alternative for power generation and refrigeration. The key parameter that defines the efficiency of thermoelectric materials is the 'dimensionless figure of merit' $ZT = S^2\sigma T/\kappa$, where S, σ, κ are the Seebeck coefficient, electrical conductivity and total thermal conductivity respectively. Ideally, to achieve high ZT both the Seebeck coefficient and electrical conductivity should be large, while total thermal conductivity must be minimized. In this thesis, first-principles calculations of the Seebeck coefficient, lattice thermal conductivity and electrical conductivity are performed to study mechanisms and factors that gives rise to high ZT.

One effective way to enhance ZT is through direct reduction of lattice thermal conductivity. We perform calculation and analysis of lattice thermal conductivity for thermoelectric materials by solving the Boltzmann transport equation iteratively in the framework of perturbation theory. The second- and third-order interatomic force constants are extracted using the recently developed CSLD (compressive sensing lattice dynamics) method. Afterwards, we evaluate opportunities to achieve further reduction of lattice thermal conductivity. Our first study of ternary

zinc-blende-based compounds Cu_3SbS_4 and Cu_3SbSe_4 shows that optical modes in these two compounds contribute a sizable portion of the total lattice thermal conductivity and thus cannot be neglected. Due to the fact that phonon modes with mean free paths larger than 10 nm carry about 80% of the heat, nanostructuring, which reduces the mean free path, is a promising way to reduce the lattice thermal conductivity by reducing the characteristic length. In addition, our simple alloying model including mass disorder reproduces experimental findings that forming solid solutions rapidly decreases the lattice thermal conductivity. An alternative way to reduce lattice thermal conductivity is to introduce guest atoms in host cage structures. Our study of type-I Si clathrates containing guest atoms Na and Ba shows that Na tends to form incoherent localized phonon mode while Ba coherently couples with the host cages. The low lattice thermal conductivities of Na- and Ba-filled Si clathrates should be attributed to the dramatic reductions in both phonon lifetime and group velocity. Analysis of phonon scattering process reveals that localized modes can be effectively emitted and absorbed, thus dramatically enhancing overall scattering rates.

Another widely adopted approach to achieve high ZT is through maintaining a high power factor $S^2\sigma$. To accurately determine the Seebeck coefficient and electrical conductivity, we estimate carrier lifetime due to electron-phonon interaction under relaxation time approximation using the electron-phonon Wannier interpolation technique. Our study of noble metals Cu and Ag shows that their positive Seebeck coefficients can be mostly attributed to the negative energy dependence of carrier lifetime. In contrast to the previous study of positive Seebeck in Li, which is due to the deviation of electronic behavior from that in free electron model, it is the nontrivial energy dependence of electron-phonon interaction vertex that leads to the positive Seebeck coefficient. Intermetallic compound B20-type CoSi has drawn considerable attention due to its exceptionally high power factor and large Seebeck coefficient. Our study shows that the large negative Seebeck coefficient of the pristine CoSi is mostly due to the strong energy dependence

of carrier lifetime, which together with the high electrical conductivity leads to the high power factor. For heat transport, both electron-phonon and phonon-phonon interactions contribute significantly to phonon scattering at temperatures lower than 200 K. While at temperatures higher than 300 K, phonon-phonon interaction dominates over electron-phonon interaction. Based on the optimized power factor with properly adjusted carrier concentration, we predict that the maximum ZTs at 300 and 600 K are about 0.11 and 0.25 respectively without further reducing the total thermal conductivity.

Known good thermoelectric materials often are comprised of elements that are in low abundance, toxic and require careful doping and complex synthesis procedures. High performance thermoelectricity has been reported in earth-abundant compounds based on natural mineral tetrahedrite ($Cu_{12}Sb_4S_{13}$). Our first-principles electronic structure calculations of $Cu_{12}Sb_4S_{13}$ show that Cu atoms are all in the monovalent Cu^+ state, creating two free hole states per formula unit of the pristine compound. Optimal thermoelectric performance can be achieved via electron doping. Substituting transition metals on Cu 12d sites does the job. Detailed analysis shows that Zn and Fe substitutions tend to fill the empty hole states, while Ni substitution introduces an additional hole to the valence band by forming ferromagnetic configuration. Experimentally observed extremely low lattice thermal conductivity can be attributed to the out-of-plane vibrations of the three-fold Cu ions. This is further verified by the large Grüneisen parameter calculated.

The dissertation of Yi Xia is approved.

Dwight Christopher Streit

Anastassia N. Alexandrova

Vidvuds Ozoliņš, Committee Chair

University of California, Los Angeles

2016

To my parents, friends and people who have supported me.

TABLE OF CONTENTS

LIST OF FIGURES

List of Tables

ACKNOWLEDGMENTS

Foremost, I would like to thank my advisor, Prof. Vidvuds Ozoliņš for support and guidance over the years, asking insightful questions and offering invaluable advice. You have set an example of excellence as a researcher, mentor, instructor, and role model.

I must thank Dr. Fei Zhou for endless help and innovative inspiration. And to all of my group members, Weston G. Nielson, Chi-Ping Liu, Biljana Rolih, Yu Chao, Hao Lin, Jiatong Chen, Yusheng Kuo, Daniel Eth, Junsoo Park and Brad Magnetta. I specially thank Junsoo Park and Daniel Eth for proofreading my thesis draft.

I would also like to thank our experimental collaborators Prof. Donald Morelli and Dr. Xu Lu. Thanks for realizing and verifying our theoretical predictions through experimental synthesis.

Thank you as well to my additional committee members, Prof. Anastassia N. Alexandrova, Prof. Dwight C. Streit and Prof. Jaime Marian.

To my girlfriend Xiyu Yi, thanks for always being supportive! Last but not least, thank you to my parents. I would not have gotten this far without their support and continual encouragement.

VITA

2011–present Graduate Student Researcher in Materials Science Engineering, University of California, Los Angeles (UCLA)

PUBLICATIONS

Xu Lu, Donald T. Morelli, Yi Xia, Fei Zhou, Vidvuds Ozoliņš, Hang Chi, Xiaoyuan Zhou and Ctirad Uher, "High Performance Thermoelectricity in Earth-Abundant Compounds Based on Natural Mineral Tetrahedrites", ***Advanced Energy Materials***, 2013, 3(3), 342-348

Fei Zhou, Weston Nielson, Yi Xia and Vidvuds Ozoliņš, "Lattice Anharmonicity and Thermal Conductivity from Compressive Sensing of First-Principles Calculations", ***Physical Review Letters***, 2014, 113(18), 185501

Xu Lu, Donald T. Morelli, Yi Xia and Vidvuds Ozoliņš, "Increasing the Thermoelectric Figure of Merit of Tetrahedrites by Co-Doping with Nickel and Zinc", ***Chemistry of Materials***, 2015, 27(2), 408-413

Xu Lu, Donald T. Morelli, Yuxing Wang, Wei Lai, Yi Xia and Vidvuds Ozoliņš, "Phase Stability, Crystal Structure, and Thermoelectric Properties of $Cu_{12}Sb_4S_{13-x}Se_x$ Solid Solutions", ***Chemistry of Materials***, 2016, 28(6), 1781-1786

Jiangang He, Maximilian Amsler, Yi Xia, S. Shahab Naghavi, Vinay I. Hegde, Shiqiang Hao,

Stefan Goedecker, Vidvuds Ozoliņš and Chris Wolverton, "Ultralow Thermal Conductivity in Full-Heusler Semiconductors", ***Physical Review Letters***, 2016, 117(4), 046602

Yi Xia, Fei Zhou, Weston Nielson and Vidvuds Ozoliņš, "First-Principles Study of Lattice Thermal Conductivity of Cu_3SbS_4 and Cu_3SbSe_4", in preparation (2016)

Yi Xia, Weston Nielson Fei Zhou and Vidvuds Ozoliņš, "First-Principles Study of the Impact of Guest Impurities (Na and Ba) on Lattice Thermal Conductivity of Type-I Si Clathrate", in preparation (2016)

Yi Xia and Vidvuds Ozoliņš, "Nontrivial Electron-Phonon Interactons Lead to Positive Seebeck Coefficients in Cu and Ag", in preparation (2016)

Yi Xia and Vidvuds Ozoliņš, "First-Principles Study of Thermoelectric Properties from Elecrton-Phonon and Phonon-Phonon Interactions in B20-type CoSi", in preparation (2016)

CHAPTER 1

Introduction

1.1 Motivation

With the ever increasing world's demand for energy and the detrimental impact on the environment due to combustion of fossil fuels, thermoelectric materials have drawn vast attention because the thermoelectric effect enables direct conversion between thermal and electrical energies. And it provides an alternative for power generation and refrigeration. Waste heat generated at homes, automotive exhaust and industrial processes can be harvested and converted into electricity using thermoelectric materials. In addition, thermoelectric refrigeration can be utilized for localized cooling in electronic components. Since thermoelectric devices are in solid-state forms with no moving parts, they are silent, reliable and scalable, making them ideal for small, distributed power generation. However, the low efficiency has long been a problem for thermoelectrics to be cost-effective for application in a global scale. In recent years, efforts have been made to either engineer some of the existing thermoelectrics to design higher efficiencies or discover completely new materials.

New thermoelectric materials with ZT values higher than unity has been developed and discovered, including thin film superlattices, complex bulk compounds (such as skutterudites, clathrates and Zintl phases) and bulk nanostructured chalcogenides. Unfortunately, most of the above materials are not suitable for large-scale application due to the complex and costly synthesis procedures or the use of rare or toxic elements. One of the current challenges is the discovery of new

bulk thermoelectric materials which are inexpensive, environment-friendly, easy to synthesize, and comprised of earth-abundant elements. To test candidate thermoelectric materials exhaustively only by experimental methods is costly and ineffective, if possible at all. This is where computational techniques and first-principles modeling come in handy for extensively characterizing and screening materials. In addition, accurate calculations of thermoelectric properties of existing materials not only explain experimental measurements, but also provide insights for the search of new thermoelectrics. In this work, density functional theory (DFT) and auxiliary methods have been utilized and developed to study the heat (phonon) and carrier (electron) transports to optimize and discover new high-performance thermoelectric materials.

1.2 Seebeck and Peltier Effects

Thermoelectric energy harvesting and cooling are deeply rooted in two interrelated phenomena, namely the Seebeck and Peltier effects. The Seebeck effect, first discovered by Thomas Johann Seebeck in the early 1800s [1], describes a phenomenon that if two dissimilar materials are joined together with the junctions held at different temperatures, a voltage proportional to the temperature gradient is established. This effect can be understood as a coupling between two different thermodynamic potentials induced by gradients of temperature and electrochemical potential. The proportionality between the voltage gradient $\mathbf{E}$ and temperature gradient $\boldsymbol{\nabla} T$ is defined as the Seebeck coefficient S

$$\mathbf{E} = -S\boldsymbol{\nabla} T. \tag{1.1}$$

Under this definition, the Seebeck coefficient is negative for electrons and positive for holes. The Seebeck coefficient may vary significantly across different materials, e.g., only a few microvolts per Kelvin for metals and a few hundred microvolts per Kelvin for semiconductors. The inverse

process, first discovered by Jean Charles Athanase Peltier, is called the Peltier effect and describes heating or cooling at the junctions when electrical current is forced through one of them [2]. Similar to the earlier case, the proportionality between generated (or removed) heat per unit time $\mathbf{J}_Q$ at the junctions and the electrical current $\mathbf{J}$ is defined as the Peltier coefficient Π

$$\mathbf{J}_Q = \Pi \mathbf{J}. \tag{1.2}$$

The Seebeck and Peltier effects are essentially two sides of the same coin and can be understood in the unifying picture: the Seebeck effect drives an electrical current when the thermoelectric circuit is closed and the induced current itself transfers heat via the Peltier effect. The explicit relation between the Seebeck and Peltier coefficients is [3]

$$\Pi = ST. \tag{1.3}$$

1.3 Thermodynamics of Thermoelectricity

The previous section has focused on experimental characterization of the Seebeck and Peltier effects. Theoretical formulation of thermoelectric phenomena was initiated by Onsager who proposed to describe the coupled heat and carrier transport under linear out-of-equilibrium thermodynamics [4]. Afterwards, a coherent thermodynamical description of thermoelectric processes was developed by Callen [5]. Thermoelectric processes thus can be overarchingly described by Onsager-Callen theory based on the assumption that the system evolution is governed by minimal production of entropy and microscopic reversibility. Under these assumptions, the processes are quasi-static and the intensive parameters are well defined at each time and location. By the Onsager-Callen theory, the coupling between heat flux $\mathbf{J}_Q$ and particle flux $\mathbf{J}_N$ and that between

chemical potential gradient $\nabla(\mu_e)$ and temperature gradient $\nabla(\frac{1}{T})$ can be expressed as

$$\begin{bmatrix} \mathbf{J}_N \\ \mathbf{J}_Q \end{bmatrix} = \begin{bmatrix} L_{11} & L_{12} \\ L_{21} & L_{22} \end{bmatrix} \begin{bmatrix} -\frac{1}{T}\nabla(\mu_e) \\ \nabla\left(\frac{1}{T}\right) \end{bmatrix}. \tag{1.4}$$

The crucial key here is that $L_{12} = L_{21}$. This is the Onsager reciprocal relation and implies the time-reversal symmetry of the process at the microscopic scale. Eq. (1.4) can be rewritten using Ohm's law under isothermal conditions, Fourier's law under zero electrochemical gradient and the definition of Seebeck coefficient as

$$\begin{bmatrix} \mathbf{J}_N \\ \mathbf{J}_Q \end{bmatrix} = \begin{bmatrix} \frac{T}{e^2}\sigma & \frac{T^2}{e^2}\sigma S \\ \frac{T^2}{e^2}\sigma S & T^2\kappa_E \end{bmatrix} \begin{bmatrix} -\frac{1}{T}\nabla(\mu_e) \\ \nabla\left(\frac{1}{T}\right) \end{bmatrix}, \tag{1.5}$$

where e and σ indicate carrier charge and isothermal electrical conductivity respectively. Two different thermal conductivities can be introduced: one under zero electrical current κ_J and another under zero electrochemical gradient κ_E. And they are related by a coupling term that contains Seebeck coefficient,

$$\kappa_E = TS^2\sigma + \kappa_J. \tag{1.6}$$

Further more κ_J contains only the conductive contribution, while κ_E also includes the convective contribution. They correspond to the thermal conductivities under open-circuit and short-circuit conditions respectively. Simplifying the entropy flux using Eq.(1.6) makes the physical meaning of the Seebeck coefficient very clear

$$\mathbf{J}_s = \frac{\mathbf{J}_Q}{T} = S\mathbf{J} - \kappa_J\nabla T, \tag{1.7}$$

where the Seebeck coefficient can be interpreted as entropy per charge carrier [3].

The efficiency of waste heat harvesting of a thermoelectric material generally depends on two factors: intrinsic material properties and working conditions. A reasonable argument for the definition of ZT of a thermoelectric material that characterizes the intrinsic properties can be made using the two thermal conductivity expressions in Eq. (1.6). Since κ_J is the open-circuit thermal conductivity, it needs to be minimized to maximize the open-circuit voltage through impeding the heat transport. While κ_E corresponds to the short-circuit thermal conductivity, it needs to be maximized to maximize the short-circuit current. As a result, $\frac{\kappa_E}{\kappa_J}$ should be maximized. From Eq. (1.6), we have

$$\frac{\kappa_E}{\kappa_J} = \frac{S^2\sigma}{\kappa_J}T + 1, \tag{1.8}$$

with

$$ZT = \frac{S^2\sigma}{\kappa_J}T. \tag{1.9}$$

Further including thermal conductivity contribution from the lattice part κ_l , ZT can be generally expressed as

$$ZT = \frac{S^2\sigma T}{\kappa_e + \kappa_l}, \tag{1.10}$$

where $S^2\sigma$ is defined as the thermoelectric power factor.

1.4 Optimization of Thermoelectric Properties

To enhance ZT, the Seebeck coefficient and electrical conductivity need to be maximized while the total thermal conductivity is minimized. For a good thermoelectric material, the Seebeck coefficient is usually larger than 100 μV/K, carrier conductivity is larger than 10^4 S/m and lattice thermal conductivity is less than 1.0 W/(m·K). Since these quantities are naturally interrelated, it is a nontrivial task to achieve an overall optimization. For instance, electrical conductivities are usually high in metals. However, their Seebeck coefficients are small. Semiconductors with wide band gaps have large Seebeck coefficients. However, their electrical conductivities are generally too low due to low carrier concentrations. This contradictory relation between the Seebeck coefficient and electrical conductivity makes enhancing the thermoelectric power factor $S^2\sigma$ a nontrivial task. The resulting $S^2\sigma$ typically reaches its peak value at carrier concentrations between 10^{19} and 10^{21} carriers per cm^3, which are generally found in heavily doped semiconductors and semimetals. Another counteraction is the proportionality between electrical conductivity and electrical thermal conductivity, as indicated by the Wiedemann-Franz law. Cleary lowering the latter entails lowering the former, which does not help ZT. Therefore, it is more reasonable to reduce lattice thermal conductivity because the transport mechanism is completely separate and does not hurt carrier transport. As a result, one must seek to maximize power factor and minimize lattice thermal conductivity in order achieve maximum ZT. The "phonon-glass electron-crystal" concept highlights this idea since amorphous glass scatters phonons while periodic crystal helps electron transport [6].

1.4.1 Phonon

Phonons play a critical role in heat and carrier transports. Interactions between phonons and electrons lead to finite electrical conductivity, and the interactions among phonons give rise to

finite lattice thermal conductivity. Due to the complexity of the interactions between phonons and electrons, a widely adopted strategy to enhance ZT is directly reducing lattice thermal conductivity. This strategy is typically realized by (1) finding thermoelectric materials with intrinsically low lattice thermal conductivity and (2) engineering lower lattice thermal conductivity. Two factors that mainly determine the lattice thermal conductivity of a crystalline compound are phonon group velocity and relaxation time. A larger group velocity and a longer relaxation time lead to a higher κ_l. As a result, complex crystal structures with heavy atoms, which often leads to small group velocity and structures with strong anharmonic phonons, are sought after. Examples include the Zintl phases [7], crystalline rocksalt structure I-V-VI_2 compounds (e.g. $AgSbTe_2$) [8], tetrahedrite ($Cu_{12}Sb_4S_{13}$) [9] and SnSe [10]. On the other hand, ways to engineer lower lattice thermal conductivity with solid solution, thin film superlattice, coherent interface, grain boundary, bulk nanostructure and rattling atom are introduced [11, 12, 13, 14, 7, 15].

1.4.2 Electron

The thermoelectric power factor and electrical thermal conductivity are fully governed by electron transport. The thermoelectric power factor needs to be optimized, which is usually done by (1) selecting crystal structures whose electronic band structures support both high Seebeck coefficient and electrical conductivity and (2) adjusting electron concentration. It is found that large Seebeck coefficient is associated with flat band edges while high electrical conductivity requires dispersive band pockets with large Fermi velocity. This indicates that band structures composed of both heavy and light bands near Fermi level are preferred [16]. Such a strategy is widely used to search for materials with high power factor. More advanced techniques include achieving band convergence by tuning composition and temperature [17]. It is also found that a steeply increasing of density of states, similar to a step function, is beneficial to power factor [18, 19]. Therefore, low-dimensional electronic structure is widely explored in both low-dimensional and

3D systems [20, 21]. In addition, enhancement of the Seebeck coefficient can be achieved by distorting density of states through introducing resonant impurities [22].

1.5 Thesis Objective and Organization

The major objective of this thesis is to understand the important roles of phonons and electrons in determining thermoelectric properties through utilizing and developing advanced methods based on first-principles density functional calculations. Afterwards, discovering new high-performance and environmentally friendly thermoelectric materials as well as optimizing existing thermoelectric materials are pursued.

Chapter 2 introduces various methods. After briefly laying out the foundations of density functional theory, we present detailed phonon and electron transport models explicitly considering electron-phonon and phonon-phonon interactions. To access two essential quantities required in transport models, namely, interatomic force constant and electron-phonon interaction vertex, a recently developed compressive sensing lattice dynamics method and electron-phonon Wannier interpolation are discussed in detail.

Chapter 3 and 4 are focused on phonon transport. We demonstrate the compressive sensing lattice dynamics is a very efficient method to extract accurate high order interatomic force constants which are used to calculate lattice thermal conductivity. Chapter 3 contains a detailed analysis of lattice thermal conductivity including mean free path dependence. The effects of forming nanostructure and solid solutions are shown for two promising thermoelectric materials: Cu_3SbS_4 and Cu_3SbSe_4. Chapter 4 explains another very effective strategy to reduce lattice thermal conductivity in cage structures such as Si-based Clathrates by inserting rattling atoms. This further clarifies the impact of rattling atoms on phonon group velocity and lifetime.

Chapter 5 and 6 are focused on electron transport. We start with simple but nontrivial example of

noble metals Cu and Ag in Chapter 5, and demonstrate the importance of accurately taking into account electron-phonon interaction in calculating both the Seebeck coefficient and electrical conductivity. Two factors, i.e., energy dependence of electron lifetime and electron-phonon interactions are found to be essential to explain the anomalous positive Seebeck coefficient in Cu and Ag. Chapter 6 deals with a real thermoelectric material: intermetallic B20-type CoSi. With both electron-phonon and phonon-phonon interactions considered, we calculated thermoelectric properties in excellent agreement with experiments, explaining the origin of anomalously high power factor.

Chapter 7 is dedicated to the study of our newly discovered high-performance thermoelectric material: tetrahedrite ($Cu_{12}Sb_4S_{13}$). Our study includes the structural stability, electronic band structure, transition metal dopants and lattice dynamics, most of which have been published in Ref. [9, 23, 24, 25].

References

[1] T.J. Seebeck. *Proc. Prussian Acad. Sci.*, pages 265–373, 1822.

[2] J.C. Peltier. *Ann. Chem. LVI*, pages 371–387, 1834.

[3] Christophe Goupil, Wolfgang Seifert, Knud Zabrocki, Eckhart Müller, and G. Jeffrey Snyder. Thermodynamics of thermoelectric phenomena and applications. *Entropy*, 13(8):1481, 2011.

[4] Lars Onsager. Reciprocal relations in irreversible processes. i. *Phys. Rev.*, 37:405–426, Feb 1931.

[5] Herbert B. Callen. The application of onsager's reciprocal relations to thermoelectric, thermomagnetic, and galvanomagnetic effects. *Phys. Rev.*, 73:1349–1358, Jun 1948.

[6] G. A. Slack. *CRC Handbook of Thermoelectrics*. CRC Press, Boca Raton, FL, 1995.

[7] G. Jeffrey Snyder and Eric S. Toberer. Complex thermoelectric materials. *Nat. Mater.*, 7(2):105–114, 2008.

[8] D. T. Morelli, V. Jovovic, and J. P. Heremans. Intrinsically minimal thermal conductivity in cubic I-V-VI_2 semiconductors. *Phys. Rev. Lett.*, 101:035901, Jul 2008.

[9] X. Lu, D.T. Morelli, Y. Xia, F. Zhou, V. Ozolins, H. Chi, X. Zhou, and C. Uher. High Performance Thermoelectricity in Earth-Abundant Compounds Based on Natural Mineral Tetrahedrites. *Adv. Energy Mater.*, doi: 10.1002/aenm.201200650., 2012.

[10] Li-Dong Zhao, Shih-Han Lo, Yongsheng Zhang, Hui Sun, Gangjian Tan, Ctirad Uher, C. Wolverton, Vinayak P. Dravid, and Mercouri G. Kanatzidis. Ultralow thermal conductivity and high thermoelectric figure of merit in snse crystals. *Nature*, 508(7496):373–377, 04 2014.

[11] Steven N. Girard, Jiaqing He, Changpeng Li, Steven Moses, Guoyu Wang, Ctirad Uher, Vinayak P. Dravid, and Mercouri G. Kanatzidis. In situ nanostructure generation and evolution within a bulk thermoelectric material to reduce lattice thermal conductivity. *Nano Letters*, 10(8):2825–2831, 2010. PMID: 20698594.

[12] Bed Poudel, Qing Hao, Yi Ma, Yucheng Lan, Austin Minnich, Bo Yu, Xiao Yan, Dezhi Wang, Andrew Muto, Daryoosh Vashaee, Xiaoyuan Chen, Junming Liu, Mildred S. Dresselhaus, Gang Chen, and Zhifeng Ren. High-thermoelectric performance of nanostructured bismuth antimony telluride bulk alloys. *Science*, 320(5876):634–638, 2008.

[13] Kanishka Biswas, Jiaqing He, Qichun Zhang, Guoyu Wang, Ctirad Uher, Vinayak P. Dravid, and Mercouri G. Kanatzidis. Strained endotaxial nanostructures with high thermoelectric figure of merit. *Nat Chem*, 3(2):160–166, 02 2011.

[14] Rama Venkatasubramanian, Edward Siivola, Thomas Colpitts, and Brooks O'Quinn. Thin-film thermoelectric devices with high room-temperature figures of merit. *Nature*, 413(6856):597–602, 10 2001.

[15] Toshiro Takabatake, Koichiro Suekuni, Tsuneyoshi Nakayama, and Eiji Kaneshita. Phonon-glass electron-crystal thermoelectric clathrates: Experiments and theory. *Rev. Mod. Phys.*, 86:669–716, Jun 2014.

[16] Kazuhiko Kuroki and Ryotaro Arita. Pudding mold band drives large thermopower in Na_xCoO_2. *Journal of the Physical Society of Japan*, 76(8):083707, 2007.

[17] Yanzhong Pei, Xiaoya Shi, Aaron LaLonde, Heng Wang, Lidong Chen, and G. Jeffrey Snyder. Convergence of electronic bands for high performance bulk thermoelectrics. *Nature*, 473(7345):66–69, 05 2011.

[18] L. D. Hicks and M. S. Dresselhaus. Thermoelectric figure of merit of a one-dimensional conductor. *Phys. Rev. B*, 47:16631–16634, Jun 1993.

[19] L. D. Hicks, T. C. Harman, X. Sun, and M. S. Dresselhaus. Experimental study of the effect of quantum-well structures on the thermoelectric figure of merit. *Phys. Rev. B*, 53:R10493–R10496, Apr 1996.

[20] David Parker, Xin Chen, and David J. Singh. High three-dimensional thermoelectric performance from low-dimensional bands. *Phys. Rev. Lett.*, 110:146601, Apr 2013.

[21] Daniel I. Bilc, Geoffroy Hautier, David Waroquiers, Gian-Marco Rignanese, and Philippe Ghosez. Low-dimensional transport and large thermoelectric power factors in bulk semiconductors by band engineering of highly directional electronic states. *Phys. Rev. Lett.*, 114:136601, Mar 2015.

[22] Joseph P. Heremans, Bartlomiej Wiendlocha, and Audrey M. Chamoire. Resonant levels in bulk thermoelectric semiconductors. *Energy Environ. Sci.*, 5:5510–5530, 2012.

[23] Fei Zhou, Weston Nielson, Yi Xia, and Vidvuds Ozoliņš. Lattice anharmonicity and thermal conductivity from compressive sensing of first-principles calculations. *Phys. Rev. Lett.*, 113:185501, Oct 2014.

[24] Xu Lu, Donald T. Morelli, Yi Xia, and Vidvuds Ozolins. Increasing the thermoelectric figure of merit of tetrahedrites by co-doping with nickel and zinc. *Chemistry of Materials*, 27(2):408–413, 2015.

[25] Xu Lu, Donald T. Morelli, Yuxing Wang, Wei Lai, Yi Xia, and Vidvuds Ozolins. Phase stability, crystal structure, and thermoelectric properties of $Cu_{12}Sb_4S_{13-x}Se_x$ solid solutions. *Chemistry of Materials*, 28(6):1781–1786, 2016.

CHAPTER 2

Methods

2.1 Density Functional Theory

2.1.1 Kohn-Sham Equation

Many material properties can be determined by solving the Schrödinger equation

$$\hat{H}\Psi = E\Psi, \tag{2.1}$$

where $\hat{H}$ is the Hamiltonian operator of the system composed of electrons and nuclei, which can be explicitly expressed in atomic units as

$$\hat{H} = -\frac{1}{2}\sum_i \nabla_i^2 - \frac{1}{2}\sum_I \frac{\nabla_I^2}{M_I} + \sum_{i<j} \frac{1}{|\mathbf{r}_i - \mathbf{r}_j|} - \sum_{i,I} \frac{Z_I}{|\mathbf{r}_i - \mathbf{R}_I|} + \sum_{I<J} \frac{Z_I Z_J}{|\mathbf{R}_I - \mathbf{R}_J|}, \tag{2.2}$$

where i, j and I, J are indices for electrons and nuclei. In this equation, the first two terms denote the kinetic energies for electrons and nuclei, the third term is the electron-electron Coulombic interaction, the fourth term is the electron-nucleus interaction and the last term is the nucleus-nucleus interaction. Under the Born-Oppenheimer approximation in which the electron degrees of freedom are decoupled from nucleic motion due to the large mass difference, the Hamiltonian

can be simplified for electrons as

$$\begin{aligned}\hat{H}_{\mathrm{e}} &= \hat{T} + \hat{V}_{\mathrm{ee}} + \hat{V}_{\mathrm{ext}}, \\ &= -\frac{1}{2}\sum_{i}\nabla^2 + \sum_{i<j}\frac{1}{|\mathbf{r}_i - \mathbf{r}_j|} + \sum_{i,I}V_I(|\mathbf{r}_i - \mathbf{R}_I|).\end{aligned} \tag{2.3}$$

This full many-body Schrödinger equation that involves $3N$ degrees for N electrons contained in the system is very difficult to solve. An effective approach is to use electron density as the basic variable instead of many-body wavefunctions. This method is called density functional theory (DFT). DFT is based on two theorems initially proven by Hohenberg and Kohn [1]. The first Hohenburg-Kohn theorem states that for any system of interacting particles in an external potential $V_{\mathrm{ext}}(\mathbf{r})$, the potential $V_{\mathrm{ext}}(\mathbf{r})$ is determined uniquely, up to a constant, by the ground state electron density $n_0(\mathbf{r})$**.** Since the Hamiltonian is thus fully determined up to a constant shift of the energy, the ground state and all excited states are determined. The second Hohenberg-Kohn theorem states that a universal functional for the energy $E(n)$ in terms of the density $n(\mathbf{r})$ can be defined, valid for any external potential $V_{\mathrm{ext}}(\mathbf{r})$. For any particular $V_{\mathrm{ext}}(\mathbf{r})$, the exact ground state energy of the system is the global minimum of this functional, and the density $n(\mathbf{r})$ that minimizes the functional is the exact ground state density $n_0(\mathbf{r})$. This leads to a conclusion that the ground state of a system can be found by minimizing the total energy with respect to particle density while conserving the total number of particles

$$E(n_0) = \min_{n}\left\{T(n) + E_{\mathrm{ee}}(n) + \int d\mathbf{r}V_{\mathrm{ext}}(\mathbf{r})n(\mathbf{r})\right\}, \int n(\mathbf{r})d\mathbf{r} = N. \tag{2.4}$$

To put the Hohenberg-Kohn theorems into practical use, Kohn and Sham proposed an approach to replace the original many-body problem with an independent particle problem [2]. It maps the original interacting system with real potential onto a non-interacting system in which the electrons experience an effective Kohn-Sham single-particle potential. The Kohn-Sham equation

derived from the variational principle can be written as

$$\left[-\frac{1}{2}\nabla^2 + V_{\text{eff}}(\mathbf{r}) \right] \psi_i(\mathbf{r}) = \varepsilon_i \psi_i(\mathbf{r}), \tag{2.5}$$

where $\psi_i(\mathbf{r})$ and ε_i are the effective Kohn-Sham orbitals and the corresponding energy eigenvalues. The effective potential is

$$\begin{aligned} V_{\text{eff}} &= V_{\text{ext}}(\mathbf{r}) + \frac{\delta E_{\text{H}}}{\delta n(\mathbf{r})} + \frac{\delta E_{\text{xc}}}{\delta n(\mathbf{r})} \\ &= V_{\text{ext}}(\mathbf{r}) + V_{\text{H}}(\mathbf{r}) + V_{\text{xc}}(\mathbf{r}), \end{aligned} \tag{2.6}$$

where $V_{\text{ext}}(\mathbf{r})$ is the external field of nuclei, $V_{\text{H}}(\mathbf{r})$ is the electron-electron Coulombic interaction, also known as the Hartree potential, and $V_{\text{xc}}(\mathbf{r})$ is the exchange-correlation potential derived from the derivative of the exchange-correlation energy with respective to electron density. All many-body effects of exchange and correlation are grouped into the exchange-correlation energy E_{xc}

$$E_{\text{xc}}(n) = T(n) - T_s(n) + E_{\text{ee}}(n) - E_{\text{H}}(n). \tag{2.7}$$

This equation shows that $E_{\text{xc}}(n)$ is the sum of two differences: one between single- and many-particle kinetic energies, and another between the Hartree energy and many-particle electron-electron interaction energy. The Kohn-Sham equation is a nonlinear equation whose potential depends on its own eigenfunctions through the electron-charge density distribution. Once the exchange-correlation functional is approximated properly, the Kohn-Sham equation can be solved in a self-consistent manner with a variety of methods.

2.1.2 Exchange-Correlation Functional

There are two common and popular approximations to the exchange-correlation functional, i.e., the local density approximation (LDA) [3] and the generalized gradient approximation (GGA) [4, 5]. The basic assumption in LDA states that the exchange-correlation energy at a point $\mathbf{r}$ equals to the exchange-correlation energy of a uniform electron gas with the same density. Thus the exchange-correlation energy can be written as

$$E_{\mathrm{xc}}^{\mathrm{LDA}}[n(\mathbf{r})] = \int \varepsilon_{\mathrm{xc}}^{\mathrm{LDA}}(\mathbf{r}) n(\mathbf{r}) d\mathbf{r}. \tag{2.8}$$

The corresponding exchange-correlation potential is

$$V_{\mathrm{xc}}(\mathbf{r}) = \frac{\delta E_{\mathrm{xc}}[n(\mathbf{r})]}{\delta n(\mathbf{r})} = \frac{\partial[\varepsilon_{\mathrm{xc}}^{\mathrm{LDA}}(\mathbf{r}) n(\mathbf{r})]}{\partial n(\mathbf{r})}, \tag{2.9}$$

with $\varepsilon_{\mathrm{xc}}(\mathbf{r})$ approximated by a local function $\varepsilon_{\mathrm{xc}}^{\mathrm{hom}}[n(\mathbf{r})]$ derived from homogeneous electron gas. The parametrization for $\varepsilon_{\mathrm{xc}}^{\mathrm{hom}}[n(\mathbf{r})]$ from Perdew and Zunger is commonly used [6], which is based on Monte Carlo simulations of uniform electron gas [7]. Though LDA ignores the corrections to the exchange-correlation energy due to the presence of local gradients in electron density, it is a successful approximation, especially for systems with slowly varying electron density. This is mainly due to the sum rule that LDA obeys, i.e., that exactly one electron is excluded from the vicinity of a given electron [8]. However, LDA typically underestimates the bond lengths in solids, leading to overbinding [9]. GGA incorporates the gradient of the electron density $\nabla n(\mathbf{r})$ so it is a semi-local method. The GGA exchange-correlation functional is

$$E_{\mathrm{xc}}^{\mathrm{GGA}}[n(\mathbf{r})] = \int \varepsilon_{\mathrm{xc}}^{\mathrm{GGA}}[n(\mathbf{r}), n'(\mathbf{r})] n(\mathbf{r}) d\mathbf{r}. \tag{2.10}$$

Unlike LDA, GGA has no unique form and is constructed under the constraints for exchange-correlation hole [10]. By including the density gradient, GGA is more successful than LDA in that reducing the effects of overbinding. The exchange-correlation functional can be generalized to be spin-dependent. The two most widely used GGA functionals are PW91 [4] and Perdew-Burke-Enzerhof (PBE) [5].

2.1.3 Pseudopotential

The Kohn-Sham equation, given approximated exchange-correlation functionals, are generally solved iteratively by expanding the Kohn-Sham orbitals in terms of basis. For periodic systems where Kohn-Sham orbitals can be further expressed in terms of Bloch waves, the wavefunctions are conveniently expanded using a plane-wave basis set [8]. Due to the fact that electrons in the core region exhibit rapid oscillations under the actual ionic potential, an extremely large amount of plane-wave basis set is required to perform accurate all-electron calculation. The pseudopotential approximation is based on the observation that the electrons in the core region are almost environment-independent and the majority of physical properties depend on the outermost valence electrons. Pseudopotential is thus introduced to replace the ionic potential and acts on a set of pseudo-wavefunctions instead of the true valence wavefunctions.

Pseudopotential is constructed to reduce the number of required plane-wave bases. The pseudo wavefunction should have no radial nodes within the core region and agree with the true wavefunction in the valence region outside a proper cutoff radius. In addition, it is required of pseudopotentials to preserve atomic scattering properties, or phase shifts, for the valence wavefunctions [8]. For each angular momentum component of the valence wavefunction, the produced

phase shift is different, which leads to a general form of pseudopotential

$$V_I = \sum_{lm} |lm\rangle V_l \langle lm| , \tag{2.11}$$

where $|lm\rangle$ are spherical harmonics, and V_l is the pseudopotential for angular momentum l. This generalized form of pseudopotential is non-local in the sense that each angular momentum feels a different potential. In contrast, the local pseudopotential uses the same potential for all angular momentum components of the wavefunctions.

2.1.4 Density Functional Perturbation Theory

Though many useful quantities such as total energy, volume and stress can be obtained through directly solving the Kohn-Sham equation, many other interesting physical properties are response function to an external perturbation experienced by the system under investigation. Response functions are second, third or higher order derivatives of the total energy with respect to various perturbations. A typical perturbation is atomic displacement, whose first- and second-order response functions are the induced force and the interatomic force constants (IFCs), the latter of which plays a key role in determining thermodynamic properties in solids. Within the formalism of density functional perturbation theory (DFPT) [11, 12, 13], these quantities can be analytically computed.

According to the Hellmann-Feynman theorem, the first-order derivative of the ground state energy with respect to atomic displacements within DFT is

$$\mathbf{F}_I = -\frac{\partial E[n(\mathbf{r})]}{\partial \mathbf{R}_I} = -\int n(\mathbf{r}) \frac{\partial V_I(\mathbf{r})}{\partial \mathbf{R}_I} d\mathbf{r} - \frac{\partial E_{IJ}}{\partial \mathbf{R}_I}, \tag{2.12}$$

where $V_I(\mathbf{r})$ equals the external potential $V_{\text{ext}}(\mathbf{r})$ due to nuclei and E_{IJ} is the energy due to

nucleus-nucleus interaction. The second-order derivative of the energy with respect to atomic displacement is

$$\frac{\partial E[n(\mathbf{r})]}{\partial \mathbf{R}_I \partial \mathbf{R}_J} = \int \frac{\partial n(\mathbf{r})}{\partial \mathbf{R}_J} \frac{\partial V_I(\mathbf{r})}{\partial \mathbf{R}_I} d\mathbf{r} + \int n(\mathbf{r}) \frac{\partial^2 V_I(\mathbf{r})}{\partial \mathbf{R}_I \partial \mathbf{R}_J} d\mathbf{r} + \frac{\partial^2 E_{IJ}}{\partial \mathbf{R}_I \partial \mathbf{R}_J}. \tag{2.13}$$

Calculating the DFT forces only requires the knowledge of ground state charge density, while the calculation of IFCs also requires to computation of its first-order derivative with respect to atomic displacements. Note that the derivative of external potential and the ionic energy can be explicitly evaluated once the small perturbations are known. Since the charge density can be evaluated using the DFT orbitals $\psi(\mathbf{r})$, a simple linearization leads to

$$\frac{\partial n(\mathbf{r})}{\partial \mathbf{R}_I} = 4 \,\mathrm{Re} \sum_{n=1}^{N/2} \psi_n^*(\mathbf{r}) \frac{\partial \psi_n(\mathbf{r})}{\partial \mathbf{R}_I}, \tag{2.14}$$

where N is the total number of electrons. The orbital derivative $\frac{\partial \psi_n(\mathbf{r})}{\partial \mathbf{R}_I}$ is obtained by the standard first-order perturbation theory

$$(H_{\mathrm{eff}} - \varepsilon_n) \frac{\partial \psi_n(\mathbf{r})}{\partial \mathbf{R}_I} = -\left(\frac{\partial V_{\mathrm{eff}}(\mathbf{r})}{\partial \mathbf{R}_I} - \frac{\partial \varepsilon_n}{\partial \mathbf{R}_I} \right) \psi_n(\mathbf{r}), \tag{2.15}$$

where

$$\frac{\partial \varepsilon_n}{\partial \mathbf{R}_I} = \langle \psi_n | \frac{\partial V_{\mathrm{eff}}(\mathbf{r})}{\partial \mathbf{R}_I} | \psi_n \rangle, \tag{2.16}$$

$$\frac{\partial V_{\mathrm{eff}}(\mathbf{r})}{\partial \mathbf{R}_I} = \frac{V_I(\mathbf{r})}{\partial \mathbf{R}_I} + \int \frac{1}{|\mathbf{r} - \mathbf{r}'|} \frac{\partial n(\mathbf{r}')}{\partial \mathbf{R}_I} d\mathbf{r}' + \frac{dV_{\mathrm{xc}}(n)}{dn} \frac{\partial n(\mathbf{r})}{\partial \mathbf{R}_I}. \tag{2.17}$$

Equations (2.14) -(2.17) form a set of self-consistent linear equations and can be solved iteratively just like Kohn-sham equations. Eq. (2.15) is often referred as Sternheimer equation [14].

2.2 Phonon Transport

2.2.1 Phonon

Phonon is a concept that generalizes the simple harmonic oscillator to a periodic system describing the collective movement of atoms [15]. Phonon dispersion relation can be calculated by solving the classical equations of motion of atoms under a small displacement from their equilibrium positions. A frequently adopted assumption is that the displacement is so small that the potential surface can be described within the harmonic approximation, in which the spring constants connecting different atoms are represented by second-order interatomic force constants (IFCs) $\Phi^{\alpha\beta}_{lb,l'b'}$. The physical meaning of the $\Phi^{\alpha\beta}_{0b,l'b'}$ is the ratio between the induced force in α direction experienced by atom b in reference unit cell l and the small displacement of atom b' in unit cell l' along β direction. Considering the translational symmetry of lattice, the index of the reference unit cell, l, can be set to 0. Knowing $\Phi^{\alpha\beta}_{0b,l'b'}$, phonon dispersion can be readily calculated at a given wavevector $\mathbf{q}$ by diagonalizing dynamical matrix constructed as follows

$$D^{\alpha\beta}_{bb'}(\mathbf{q}) = \frac{1}{\sqrt{m_b m_{b'}}} \sum_{l'} \Phi^{\alpha\beta}_{0b,l'b'} \exp\left[i\mathbf{q}\cdot(\mathbf{r}_{0b} - \mathbf{r}_{l'b'})\right], \tag{2.18}$$

$$\sum_{\alpha\beta bb'} e^{\lambda}_{\alpha b}{}^{*} D^{\alpha\beta}_{bb'}(\mathbf{q})\, e^{\lambda'}_{\beta b'} = \omega^2_{\lambda}\delta_{\lambda\lambda'}, \tag{2.19}$$

where λ is used to distinguish each phonon mode, $\lambda \equiv (\nu, \mathbf{q})$, ν is the branch index and $\mathbf{q}$ is the wavevector. $e^{\lambda}_{\alpha b}$ is the component of polarization eigenvector which denotes the α component of the displacement of atom b in the polarization eigenvector of mode λ. The group velocity $\mathbf{v}_{\lambda}$ of mode λ can be analytically computed by taking the derivative of the dynamical matrix with respect to wavevector $\mathbf{q}$

$$\mathbf{v}_{\lambda} = \frac{1}{2\omega_{\lambda}} \langle \mathbf{e}_{\lambda} | \frac{\partial D(\mathbf{q})}{\partial \mathbf{q}} | \mathbf{e}_{\lambda} \rangle, \tag{2.20}$$

where the Cartesian index are omitted for clarity.

2.2.2 Lattice Thermal Conductivity

Phonon transport properties can be modeled using the Boltzmann transport equation (BTE) [16]. In the presence of a temperature gradient ∇T, the generalized steady-sate phonon distribution function f_λ can be obtained from the BTE [16, 17]

$$\left.\frac{\partial f_\lambda}{\partial t}\right|_{\text{scattering}} = \nabla T \cdot \mathbf{v}_\lambda \frac{\partial f_\lambda}{\partial T}. \tag{2.21}$$

Assuming a small temperature gradient, the generalized phonon distribution function can be linearized and the resulting BTE can be written as [17, 18, 19]

$$f_\lambda = f_0(\omega_\lambda) - \tau_\lambda \mathbf{v}_\lambda \cdot \nabla T \frac{\partial f_0}{\partial T}, \tag{2.22}$$

$$\tau_\lambda = \tau_\lambda^0 (1 + \Delta_\lambda), \tag{2.23}$$

where f_0 is the equilibrium Bose-Einstein distribution function, ω_λ and τ_λ^0 are the phonon mode frequency and single mode phonon relaxation time (lifetime), respectively. Δ_λ accounts for the deviation from the single mode relaxation time due to nonequilibrium distribution of interacting phonons, which is obtained by solving the linearized BTE iteratively. The key quantity that determines the finite lattice thermal conductivity is the single mode phonon relaxation time, which can be obtained using the first-order perturbation theory taking into account three-phonon scattering processes [16]. The single mode relaxation time can be written as [20, 21, 22]

$$\frac{1}{\tau_\lambda^0} = \sum_{\lambda' \lambda''}^{+} \Gamma^{+}_{\lambda\lambda'\lambda''} + \frac{1}{2} \sum_{\lambda' \lambda''}^{-} \Gamma^{-}_{\lambda\lambda'\lambda''} + \sum_{\lambda'} \Gamma^{\text{ext}}_{\lambda\lambda'}, \tag{2.24}$$

and

$$\begin{aligned}\Delta_\lambda = &\sum_{\lambda'\lambda''}^{+}\Gamma^{+}_{\lambda\lambda'\lambda''}\left(\xi_{\lambda\lambda''}\tau_{\lambda''}-\xi_{\lambda\lambda'}\tau_{\lambda'}\right)\\ &+\sum_{\lambda'\lambda''}^{-}\frac{1}{2}\Gamma^{-}_{\lambda\lambda'\lambda''}\left(\xi_{\lambda\lambda''}\tau_{\lambda''}+\xi_{\lambda\lambda'}\tau_{\lambda'}\right)\\ &+\sum_{\lambda'}\Gamma^{\mathrm{ext}}_{\lambda\lambda'}\xi_{\lambda\lambda'}\tau_{\lambda'},\end{aligned} \tag{2.25}$$

where $\xi_{\lambda\lambda'} \equiv \omega_{\lambda'} v^z_{\lambda'}/\omega_\lambda v^z_\lambda$, λ, λ' and λ'' are indices for phonon modes that enter the three-phonon scattering processes, namely, absorption (Γ^+: $\lambda+\lambda'\rightarrow\lambda''$) and emission ($\Gamma^-$: $\lambda-\lambda'\rightarrow\lambda''$). $\Gamma^{\mathrm{ext}}_{\lambda\lambda'}$ are extrinsic scattering rates from defects, mass-disorder and grain boundaries. $\Gamma^{\pm}_{\lambda\lambda'\lambda''}$ are the intrinsic scattering rates due to phonon-phonon interaction taking into account both momentum and energy conservation laws. $\Gamma^{\pm}_{\lambda\lambda'\lambda''}$ can be expressed as [17]

$$\begin{aligned}\Gamma^{\pm}_{\lambda\lambda'\lambda''} = &\frac{\hbar\pi}{4N}\left\{\begin{array}{c} f^0_{\lambda'}-f^0_{\lambda''}\\ f^0_{\lambda'}+f^0_{\lambda''}+1\end{array}\right\}\times\left|V^{(3)}_{\pm\lambda\lambda'\lambda''}\right|^2\\ &\times\frac{\delta\left(\omega_\lambda\pm\omega_{\lambda'}-\omega_{\lambda''}\right)}{\omega_\lambda\omega_{\lambda'}\omega_{\lambda''}},\end{aligned} \tag{2.26}$$

$$\begin{aligned}V^{(3)}_{\pm\lambda\lambda'\lambda''} = &\sum_{bl'b'l''b''}\sum_{\alpha\beta\gamma}\Phi^{\alpha\beta\gamma}_{0b,l'b',l''b''}\frac{e^{\lambda}_{\alpha b}e^{\pm\lambda'}_{\beta b'}e^{-\lambda''}_{\gamma b''}}{\sqrt{m_b m_{b'} m_{b''}}}\\ &\times e^{\pm i\mathbf{q}'\cdot\mathbf{r}_{l'}}e^{-i\mathbf{q}''\cdot\mathbf{r}_{l''}},\end{aligned} \tag{2.27}$$

where N is the number of sampled $\mathbf{q}$-points in the reciprocal space, $V^{(3)}_{\pm\lambda\lambda'\lambda''}$ and $\Phi^{\alpha\beta\gamma}_{0b,l'b',l''b''}$ are the scattering matrix elements and third-order IFCs, respectively. Indices b and l label the basis atoms and unit cells, while α, β, and γ represent the Cartesian directions. By integrating over the first Brillouin zone we obtain the following expression for the lattice thermal conductivity

tensor [17]

$$\kappa_l^{\alpha\beta} = \frac{1}{k_B T^2 \Omega N} \sum_{\lambda} f_0(f_0+1)(\hbar\omega_\lambda)^2 v_\lambda^\alpha v_\lambda^\beta \tau_\lambda. \tag{2.28}$$

2.2.3 Cumulative Lattice Thermal Conductivity

From Eq. (2.28) it can be seen that lattice thermal conductivity contains contributions from various phonon modes with different mean free paths (MFPs) which is defined as $\Lambda_\lambda = |v_\lambda| \cdot \tau_\lambda$. The cumulative κ_l can be calculated by summing over phonon modes with MFPs less than a given maximum MFP $\Lambda_{\max}$

$$\kappa_l^{\alpha\beta}(\Lambda_{\max}) = \frac{1}{k_B T^2 \Omega N} \sum_{\lambda}^{\Lambda_\lambda < \Lambda_{\max}} f_0(f_0+1)(\hbar\omega_\lambda)^2 v_\lambda^\alpha v_\lambda^\beta \tau_\lambda. \tag{2.29}$$

The cumulative κ_l explicitly shows the MFP dependence of κ_l and can be used as a simplified model to estimate the impact on κ_l of nanostructuring and grain boundary formation.

2.2.4 Isotopic Impurity and Alloy Scattering

Effects of isotopic impurity and alloying on the phonon spectra are taken into account using the virtual crystal method together with additional phonon scattering due to mass disorder [23]. Within this approximation, one neglects the strain effect and the disorder of IFCs, and assumes that all force constants are linearly interpolated between the pure compounds. The scattering due to mass disorder can be derived via treating the fluctuating mass in a perturbative way and including it as an external elastic scattering in BTE [24]

$$\Gamma_{\lambda\lambda'}^{\text{ext}} = \frac{\pi\omega_\lambda^2}{2} \sum_{a \in \text{u.c.}} g(a) \left| \mathbf{e}_a^{\lambda *} \cdot \mathbf{e}_a^{\lambda'} \right|^2 \delta(\omega_\lambda - \omega_{\lambda'}), \tag{2.30}$$

$$g(a) = \sum_s x_s(a)[1 - M_s(a)/\bar{M}(a)]^2, \tag{2.31}$$

where $x_s(a)$ and $M_s(a)$ are, respectively, the concentration and the atomic mass of the s-th species on the atomic site a in the unit cell.

2.2.5 Electron Scattering

The effect of electron scattering on phonon transport is generally weak in conventional semiconductors. However, for well optimized thermoelectric materials including both heavily doped semiconductors and intermetallics, the electron-phonon interaction could play an important role [25]. The scattering rate due to electron-phonon interaction can be estimated using the imaginary part of the phonon self-energy Π''_λ calculated from the first-order electron-phonon diagrams [26, 27]

$$\Gamma^{\mathrm{el}}_\lambda = \frac{2}{\hbar}\Pi''_\lambda, \tag{2.32}$$

$$\Pi''_\lambda \equiv \Pi''_{\nu,\mathbf{q}} = 2\pi \sum_{ij} \int_{\mathrm{BZ}} \frac{d\mathbf{q}}{\Omega_{\mathrm{BZ}}} \left| g^{\mathrm{SE}}_{ij,\nu}(\mathbf{k},\mathbf{q}) \right|^2 \times \left(f_{i,\mathbf{k}} - f_{j,\mathbf{k}+\mathbf{q}} \right) \delta\left(\omega_{\nu,\mathbf{q}} + \varepsilon_{i,\mathbf{k}} - \varepsilon_{j,\mathbf{k}+\mathbf{q}} \right), \tag{2.33}$$

where i and j run through electronic bands, and $g^{\mathrm{SE}}_{ij,\nu}(\mathbf{k},\mathbf{q})$ is electron-phonon interaction (EPI) vertex entering the self-energy calculation, which will be discussed in detail in the following sections.

2.3 Electron Transport

2.3.1 Seebeck Coefficient and Electrical Conductivity

The Boltzmann transport theory is a useful tool to calculate various transport properties of real materials [16]. The electrical current in α direction J_α in the presence of electrochemial and thermal gradients can be generally written in terms of transport tensors

$$J_\alpha = \sigma_{\alpha\beta} E_\beta + \xi_{\alpha\beta} \nabla_\beta T. \tag{2.34}$$

Within the band transport scenario, the transport tensors can be explicitly formulated under relaxation time approximation (RTA) [28]. In practice it is simple, general and effective, which has been verified for various materials [29, 30, 31]. It should be emphasized that the key quantity that enters into the calculation of various thermoelectric properties is the spectral conductivity $\sigma_{\alpha\beta}(\varepsilon)$

$$\sigma_{\alpha\beta}(\varepsilon) = \frac{1}{N}\sum_{i,\mathbf{k}} e^2 \tau_{i,\mathbf{k}} v^{\alpha}_{i,\mathbf{k}} v^{\beta}_{i,\mathbf{k}} \delta(\varepsilon - \varepsilon_{i,\mathbf{k}}), \tag{2.35}$$

where N, $\varepsilon_{i,\mathbf{k}}$, $\tau_{i,\mathbf{k}}$ and $v_{i,\mathbf{k}}$ are number of $\mathbf{k}$-points sampled, electronic energy, electronic lifetime and Fermi velocity for state (i, $\mathbf{k}$). The Fermi velocity (group velocity) can be obtained by calculating the derivatives of smoothed Fourier interpolated electronic bands [29]. The Seebeck coefficient at temperature T and chemical potential μ is

$$S_{\alpha\beta}(T,\mu) = -\frac{1}{eT}\frac{\int \sigma_{\alpha\beta}(\varepsilon)(\varepsilon-\mu)\left(\frac{-\partial f(T,\,\varepsilon)}{\partial \varepsilon}\right) d\varepsilon}{\int \sigma_{\alpha\beta}(\varepsilon)\left(\frac{-\partial f(T,\,\varepsilon)}{\partial \varepsilon}\right) d\varepsilon}, \tag{2.36}$$

where e, $f(T,\varepsilon)$ are absolute charge of an electron and Fermi-Dirac distribution respectively. Since it is computationally difficult to obtain converged lifetime $\tau_{i,\mathbf{k}}$ due to various possible scattering events such as electron-phonon interaction, ionized impurity and defect scattering, simplified approximations are usually adopted. One of the widely used approximations is called constant relaxation time approximation (CRTA), in which the relaxation time is treated as a global constant . An improved version is the DOS^{-1} approximation in which the relaxation time is assumed to be inversely proportional to the density of states (DOS). Note that in CRTA, the calculated Seebeck coefficient is independent of adopted relaxation time, reflecting the static properties of band structure.

Carrier conductivity $\sigma(T,\mu)$ can be calculated as

$$\sigma_{\alpha\beta}(T,\mu) = \frac{1}{\Omega}\int \sigma_{\alpha\beta}(\varepsilon)\left[-\frac{\partial f(T,\varepsilon)}{\partial \varepsilon}\right] d\varepsilon, \tag{2.37}$$

where Ω is the volume of unit cell. Electronic thermal conductivity at zero electric current (open-circuit) κ_{ij}^{el} can be obtained by subtracting the coupling term that contains the Seebeck coefficient from the electrical thermal conductivity at zero chemical potential (short-circuit) κ_{ij}^{0}

$$\kappa_{ij}^{el} = \kappa_{ij}^{0} - T\xi_{i\alpha}\left(\sigma^{-1}\right)_{\beta\alpha}\xi_{\beta j}, \tag{2.38}$$

where κ_{ij}^{0} is

$$\kappa_{\alpha\beta}^{0}(T,\mu) = \frac{1}{e^2 T\Omega}\int \sigma_{\alpha\beta}(\varepsilon)(\varepsilon-\mu)^2\left[-\frac{\partial f(T,\varepsilon)}{\partial \varepsilon}\right] d\varepsilon, \tag{2.39}$$

and $\xi_{\alpha\beta}$ is

$$\xi_{\alpha\beta}(T,\mu) = \frac{1}{eT\Omega}\int \sigma_{\alpha\beta}(\varepsilon)(\varepsilon-\mu)\left[-\frac{\partial f(T,\varepsilon)}{\partial \varepsilon}\right] d\varepsilon. \tag{2.40}$$

2.3.2 Phonon Scattering

Beyond CRTA and DOS^{-1} approximation, electron lifetime can be explicitly calculated by taking into account various scattering rates due to the presence of lattice vibrations, ionized impurities and defects. For a metallic single crystal compound at elevated temperatures, electrons are dominantly scattered by lattice vibrations. The corresponding lifetime $\tau_{i,\mathbf{k}}$ can be estimated using the imaginary part of the electron self-energy ($\Sigma''_{i,\mathbf{k}}$) from the first-order electron-phonon diagram [26, 27]

$$\frac{1}{\tau_{i,\mathbf{k}}} = \frac{2}{\hbar}\Sigma''_{i,\mathbf{k}}, \tag{2.41}$$

with

$$\begin{aligned}\Sigma''_{i,\mathbf{k}} =& \pi \sum_{j,\nu} \int_{BZ} \frac{d\mathbf{q}}{\Omega_{BZ}} \left| g^{\mathrm{SE}}_{ji,\nu}(\mathbf{k},\mathbf{q}) \right|^2 \left(1 - \frac{\mathbf{v}_{\mathbf{k}} \cdot \mathbf{v}_{\mathbf{k}+\mathbf{q}}}{|\mathbf{v}_{\mathbf{k}}| \left| \mathbf{v}_{\mathbf{k}+\mathbf{q}} \right|} \right) \\ & \times \left[\left(n_{\nu,\mathbf{q}} + f_{j,\mathbf{k}+\mathbf{q}} \right) \delta \left(\varepsilon_{i,\mathbf{k}} + \omega_{\nu,\mathbf{q}} - \varepsilon_{j,\mathbf{k}+\mathbf{q}} \right) \right. \\ & \left. + \left(n_{\nu,\mathbf{q}} + 1 - f_{j,\mathbf{k}+\mathbf{q}} \right) \delta \left(\varepsilon_{i,\mathbf{k}} - \omega_{\nu,\mathbf{q}} - \varepsilon_{j,\mathbf{k}+\mathbf{q}} \right) \right],\end{aligned} \tag{2.42}$$

where λ, $\mathbf{q}$, n and ω are phonon mode index, wave vector, population and frequency respectively. The factor $\left(1 - \frac{\mathbf{v}_{\mathbf{k}} \cdot \mathbf{v}_{\mathbf{k}+\mathbf{q}}}{|\mathbf{v}_{\mathbf{k}}| \left| \mathbf{v}_{\mathbf{k}+\mathbf{q}} \right|} \right)$ takes into account momentum relaxation in the Boltzmann transport equation [26].

2.4 Compressive Sensing Lattice Dynamics

2.4.1 Taylor Expansion of Potential Energy Surface

Interatomic force constants (IFCs) plays a vital role in general lattice dynamics, i.e., second- and third-order IFCs can be used to determine full phonon dispersion and estimate phonon scattering rates through emission and absorption processes as described in previous sections. For very anharmonic crystals which could exhibit dynamic instability, higher order terms beyond third-order IFCs are needed to model accurate lattice transport properties [32]. In general, obtaining IFCs within DFT requires to calculate total energy derivatives with respect to atomic displacements. Though second-order IFCs are well formulated within density functional perturbation theory (DFPT), accurate determination of higher-order IFCs is still a non-trivial task due to the complexity involved in implementation and the exponentially increasing number of combinations of displacements. Simple estimation of higher-order IFCs can be done using the central finite difference method, however, this formulation needs enormous number of single and multiple atomic displacements, making it extremely inefficient for crystal structures with

little symmetry. Compressive sensing lattice dynamics (CSLD) is a recently developed method to extract IFCs well beyond the harmonic approximation and up to six-order IFCs [32]. CSLD relies on the Taylor expansion of the Born-Oppenheimer potential energy E in terms of atomic displacements

$$E = E_0 + \Phi_{\mathbf{a}} u_{\mathbf{a}} + \frac{1}{2!}\Phi_{\mathbf{ab}} u_{\mathbf{a}} u_{\mathbf{b}} + \frac{1}{3!}\Phi_{\mathbf{abc}} u_{\mathbf{a}} u_{\mathbf{b}} u_{\mathbf{c}} + \cdots, \tag{2.43}$$

where E_0 is the ground-state energy, $u_{\mathbf{a}} \equiv u_{a,\alpha}$ is the displacement of atom a in the Cartesian direction α, and $\Phi_{\mathbf{ab}} \equiv \Phi_{ab}^{\alpha\beta}$, $\Phi_{\mathbf{abc}} \equiv \Phi_{abc}^{\alpha\beta\gamma}$ are the second- and third-order IFCs. The linear term with $\Phi_{\mathbf{a}}$ is absent if the reference lattice sites represent equilibrium, and the Einstein summation convention over repeated indices is used. CSLD belongs to the class of direct supercell methods where DFT forces are used to "invert" Eq. (2.43) using the force-displacement relation

$$F_{\mathbf{a}} = -\Phi_{\mathbf{a}} - \Phi_{\mathbf{ab}} u_{\mathbf{b}} - \frac{1}{2}\Phi_{\mathbf{abc}} u_{\mathbf{b}} u_{\mathbf{c}} - \cdots. \tag{2.44}$$

The determination of IFCs can be rewritten as a linear problem

$$\mathbf{F} = \mathbb{A}\mathbf{\Phi}, \tag{2.45}$$

if the unknown IFCs are arranged in a column vector $\mathbf{\Phi}$ and $\mathbf{F}$ is a column vector of the calculated atomic forces on individual atoms in a set of training configurations with displaced atoms. $\mathbb{A}$ is a matrix formed by the products of the atomic displacements in the chosen set of training configurations and is referred as the sensing matrix

$$\mathbb{A} = \begin{bmatrix} -1 & -u_{\mathbf{b}}^1 & -\frac{1}{2}u_{\mathbf{b}}^1 u_{\mathbf{c}}^1 & \cdots \\ & \cdots & & \\ -1 & -u_{\mathbf{b}}^L & -\frac{1}{2}u_{\mathbf{b}}^L u_{\mathbf{c}}^L & \cdots \end{bmatrix}, \tag{2.46}$$

where the superscripts represent combined indices labeling different atoms in the selected supercells; here we use one supercell with M atoms and generate N_{conf} displacement configurations, so that $L = MN_{\text{conf}}$.

2.4.2 Compact Representation of Interacting Clusters

In general, the summation of products between IFCs and atomic displacements in Eq. (2.43) is infinite. In order to make it computationally affordable and efficient, its symmetry properties can be explored. For simplicity, a group of atoms involved in IFCs $\Phi_{\mathbf{abc}\cdots}$ are referred as interacting cluster $\zeta \equiv \{\mathbf{a}, \mathbf{b}, \mathbf{c} \cdots\}$, where $\mathbf{a}, \mathbf{b}, \mathbf{c}$ are atoms belong to various lattice points. The interacting distance is further defined as the maximum interatomic distance among all atoms in an interacting cluster ζ. Note that the interacting distance can be zero when all the atoms in an interaction cluster sit on the same site. Also, we refer to an interacting cluster as an improper interacting cluster when there are at least two atoms on the same site, otherwise, a proper interacting cluster. Since the potential energy is invariant under the space group symmetry operations S for a crystalline solid, the interacting clusters can be divided into orbits $\{\zeta\}$ in the context of general group theory

$$\{\zeta\} \equiv \{\hat{s}\zeta | \hat{s} \in S\}, \tag{2.47}$$

where the space group symmetry operator $\hat{s}$ is composed of a rotational matrix θ and a translation $\boldsymbol{\tau}$. The symmetry operator transforms atomic position $\mathbf{r}$ as

$$\mathbf{r}' \equiv \hat{s}\mathbf{r} = \theta \cdot \mathbf{r} + \boldsymbol{\tau}. \tag{2.48}$$

Since interacting clusters in an orbit can be transformed into each other through space group symmetry operations, a representative interacting cluster ζ_{rep} can be used to generate all the symmetry-equivalent interacting clusters. Therefore we arrive at a compact representation of

interacting clusters using a set of representative interacting clusters $\{\zeta_{\text{rep}}\}$ by eliminating the symmetry equivalence. As a result, the summation in Eq. (2.43) can be simplified to run over these representative interacting clusters with space group symmetry explicitly included. To make the problem more tractable, finite cutoffs for interacting distances are used.

2.4.3 Independent Interatomic Force Constants

Though compact representation of interacting clusters can be derived by exploring the space group symmetry and adopting finite cutoff, the number of unknown parameters in $\mathbf{\Phi}$ still grow exponentially as high-order terms are included, which needs to be further reduced by exploring the symmetry operations that transform IFCs into themselves.

In the representation of interacting clusters, the order of taking the partial derivatives is uniquely determined and thus the commutative constraint on proper interacting clusters is trivial. However, if an interacting cluster is improper, there exists non-trivial permutation operation $\hat{\eta}$ that transforms a representative interacting cluster into itself

$$\hat{\eta}\zeta_{\text{rep}} = \zeta_{\text{rep}}. \tag{2.49}$$

In addition, there also exists space group symmetry operations that make ζ_{rep} invariant

$$\hat{s}\zeta_{\text{rep}} = \zeta_{\text{rep}}. \tag{2.50}$$

Enforcing these invariant constraints on the IFCs can be realized via linear transformation. Both the non-trivial permutation and space group symmetry operations can be represented in matrix forms. Derivation based on the energy invariant constraint shows the relation between IFCs and

transformed IFCs

$$\Phi_{\hat{s}\zeta}^{\alpha'\beta'\gamma'\cdots} = \sum_{\alpha\beta\gamma\cdots} \theta_{\alpha'\alpha}^{\mathrm{T}} \theta_{\beta'\beta}^{\mathrm{T}} \theta_{\gamma'\gamma}^{\mathrm{T}} \cdots \Phi_{\zeta}^{\alpha\beta\gamma\cdots}. \tag{2.51}$$

Translation symmetry constraint generalized from the acoustic sum rule in the harmonic approximation can be realized by enforcing the summation of IFCs of relevant interacting clusters to be zero

$$\sum_{\mathbf{a}} \Phi_{\mathbf{abc}\cdots} = \mathbf{0}. \tag{2.52}$$

Therefore, each symmetry operation that makes $\mathbf{\Phi}$ invariant can be written as a linear constraint on $\mathbf{\Phi}$ as

$$\mathbb{B}\mathbf{\Phi} = \mathbf{0}, \tag{2.53}$$

and these physical constraintts can be strictly enforced by finding the basis vectors of the null-space ($\mathbb{C}$) of matrix $\mathbb{B}$. If the null-space dimension of $\mathbb{B}$ is $N_{\boldsymbol{\phi}}$, we are left with $N_{\boldsymbol{\phi}}$ independent parameters in the resultant $\boldsymbol{\phi}$. The original $\mathbf{\Phi}$ can be expressed as the product of $\mathbb{C}$ and $\boldsymbol{\phi}$

$$\mathbf{\Phi} = \mathbb{C}\boldsymbol{\phi}, \tag{2.54}$$

where $\mathbb{C}$ is a $N_{\mathbf{\Phi}} \times N_{\boldsymbol{\phi}}$ matrix.

2.4.4 Convex Optimization via Compressive Sampling

Two practical difficulties are encountered when inverting Eq. (2.45) via least-squares fitting. First, the number of unknown IFC elements can be larger than the number of linearly independent rows of $\mathbb{A}$, resulting in an ill-posed underdetermined problem. This requires increasing the number of configurations N_{conf} until $\text{rank}(\mathbb{A}) > \dim(\mathbf{\Phi})$. Second, the matrix $\mathbb{A}^T\mathbb{A}$ is often ill-conditioned with a typical eigenvalue distribution spanning many orders of magnitude, especially if one desires to fit IFCs beyond the 3$^{\text{rd}}$-order. Acquiring additional data can solve the

first problem, but it is seldom a practical remedy for the second because the condition number is difficult to improve significantly.

CSLD is based on the intuitive notion that lattice dynamical forces are "near-sighted" and can be expressed in terms of short-ranged ("sparse") IFCs; this is especially true for the anharmonic terms, which usually act between close neighbors. Long-range electrostatic forces, responsible for LO/TO splitting of optical modes in polar crystals, can be dealt with separately using the calculated Born effective charges and dielectric tensors as in Ref. [33]. Pairwise IFCs in metals can also be long-ranged due to Friedel oscillations caused by the presence of a sharp Fermi surface; they manifest in the harmonic phonon spectra as the well-known Kohn anomalies. Finite temperature reduces the long-range behavior from a power law to exponential decay and smooths out the derivative discontinuities associated with the Kohn anomalies. If low-temperature phonon properties are of interest, DFT linear response calculations formulated in Ref. [11] appear to be the only practical way to obtain long-range pair IFCs.

The question is how to pick out the relevant IFCs from the formally infinite series given by Eq. (2.45). Compressive sensing, developed by Candés, Romberg, and Tao [34, 35, 36] in the context of information theory, solves this problem in a mathematically rigorous way. Their work proves that, with overwhelming probability, sparse signals can be reconstructed exactly from a small set of randomly sampled measurements. The required number of such measurements is proportional to the number of non-zero coefficients, as a rule of thumb, by a factor of 4 to 6 [37] and usually much smaller than the total number of unknown parameters, in our case, $\dim(\mathbf{\Phi})$.

Mathematically, the solution of Eq. (2.45) is obtained from a convex optimization problem that minimizes a weighted sum of the root-mean-square fitting error and the ℓ_1 norm of the IFC

vector $\mathbf{\Phi}$

$$\begin{aligned}\mathbf{\Phi}^{\mathrm{CS}} &= \arg\min_{\mathbf{\Phi}} \mu\|\mathbf{\Phi}\|_1 + \frac{1}{2}\|\mathbf{F} - \mathbb{A}\mathbf{\Phi}\|_2^2 \\ &\equiv \arg\min_{\mathbf{\Phi}} \mu\sum_I |\Phi_I| + \frac{1}{2}\sum_{a\alpha}\left(F_{a\alpha} - \sum_J A_{a\alpha,J}\Phi_J\right)^2,\end{aligned} \tag{2.55}$$

where I is a composite index representing the collection of atomic sites and the Cartesian indices defining the IFC tensor elements, $I \equiv (\mathbf{a}, \mathbf{b}, \ldots)$ and μ is a parameter that adjusts the relative weights of the fitting error versus the absolute magnitude of the nonzero-IFCs represented by the term with the ℓ_1 norm; large values of μ favor solutions with very few nonzero IFCs at the expense of the accuracy of the fitted forces ("underfitting"), while very small μ will give a dense solution with many large nonzero IFCs that fits the DFT forces well, but may have poor predictive accuracy due to numerical noise, both random and systematic ("overfitting"). There is an optimal range of μ values between these two extremes where a sparse IFC vector $\mathbf{\Phi}$ can be obtained with an excellent predictive accuracy. The addition of the ℓ_1 term solves both difficulties of the least-squares fitting approach described above: the linear problem Eq. (2.45) can be underdetermined and the ill-conditioned nature of the sensing matrix does not present a problem because the ℓ_1 norm suppresses the numerical noise stemming from the small eigenvalues of $\mathbb{A}^T\mathbb{A}$.

2.5 Electron-Phonon Wannier Interpolation

2.5.1 Electronic Wannier Function

Wannier functions were first introduced by Wannier in order to study the excitonic levels of polar insulators using a localized representation [38]. Generalized Wannier functions $|j, \mathbf{R}_e\rangle$ can be

defined through the Fourier transform of Bloch functions $|i,\mathbf{k}\rangle$ including band mixing [39]

$$|j,\mathbf{R}_e\rangle = \sum_{i,\mathbf{k}} e^{-i\mathbf{k}\cdot\mathbf{R}_e} U_{ij,\mathbf{k}} |i,\mathbf{k}\rangle, \tag{2.56}$$

where i, j and $\mathbf{R}_e$ are electronic band indices and lattice vector. The Wannier functions can be further made to be orthonormal when the mixing matrix $U_{ij,\mathbf{k}}$ is a unitary matrix

$$\langle j',\mathbf{R}'_e| |j,\mathbf{R}_e\rangle = \delta\left(\mathbf{R}_e,\mathbf{R}'_e\right)\delta\left(j',j\right). \tag{2.57}$$

The inverse Fourier transform gives the Bloch functions

$$|i,\mathbf{k}\rangle = \frac{1}{N_e}\sum_{j,\mathbf{R}_e} e^{i\mathbf{k}\cdot\mathbf{R}_e} U^{\dagger}_{ji,\mathbf{k}} |j,\mathbf{R}_e\rangle, \tag{2.58}$$

where N_e is the number of primitive cells in the supercell, corresponding to the number of $\mathbf{k}$ points. The freedom of arbitrary unitary matrix $U_{ij,\mathbf{k}}$ can be utilized to construct spatially localized Wannier functions. The most popular scheme to find a set of unitary matrices that lead to well localized Wannier functions is *maximally localized Wannier functions* [39]. This method determines the unitary transform by minimizing the Berry-phase spatial spread operator defined within the framework of the modern theory of polarization [39, 40]. The resulting Wannier functions exhibit exponential localization [41]. The unitary transform matrix is well defined for an insulator where the interesting bands form an isolated composite. In the case of a metal, such an isolated composite manifold can be extracted using a *disentanglement* strategy, in which the electronic Hamiltonian is projected onto an appropriate subspace [42]. The localized properties of Wannier functions are very useful and can be used to accurately and efficiently interpolate electronic band structure.

2.5.2 Electron and Phonon in Wannier Representation

The matrix elements of the single-particle Kohn-Sham Hamiltonian in the Bloch representation are in a diagonal form

$$H^{\mathrm{el}}_{ij,\mathbf{k}} = \langle i,\mathbf{k}|\,\hat{H}^{\mathrm{el}}\,|j,\mathbf{k}\rangle = \delta_{ij}\varepsilon_{i,\mathbf{k}}. \tag{2.59}$$

With the obtained unitary transform matrix, the Hamiltonian can be transformed into the Wannier representation

$$H^{\mathrm{el}}_{\mathbf{R}_e,\mathbf{R}'_e} = \langle \mathbf{R}_e|\,\hat{H}^{\mathrm{el}}\,|\mathbf{R}'_e\rangle = \sum_{\mathbf{k}} e^{-i\mathbf{k}\cdot\left(\mathbf{R}'_e-\mathbf{R}_e\right)} U^{\dagger}_{\mathbf{k}} H^{\mathrm{el}}_{\mathbf{k}} U_{\mathbf{k}}, \tag{2.60}$$

where band indices are omitted for clarity. Note that here the localization of electron Hamiltonian is governed by the spatial decay of the overlap between the electron Wannier functions at $\mathbf{R}_e$ and $\mathbf{R}'_e$ [27]. In contrast to electron, the atomic local displacements used as phonon Wannier basis are infinitely localized. The phonon Hamiltonian $D^{\mathrm{ph}}_{\mathbf{R}_p,\mathbf{R}'_p}$ in the phonon Wannier representation, which is transformed from dynamical matrix in the Bloch representation $D^{\mathrm{ph}}_{\mathbf{q}}$, is physically related to the IFCs. As a result, the spatial decay of IFCs determines the localization of $D^{\mathrm{ph}}_{\mathbf{R}_p,\mathbf{R}'_p}$

$$D^{\mathrm{ph}}_{\mathbf{R}_p,\mathbf{R}'_p} = \langle \mathbf{R}_p|\,\hat{D}^{\mathrm{ph}}\,|\mathbf{R}'_p\rangle = \sum_{\mathbf{q}} e^{-i\mathbf{q}\cdot\left(\mathbf{R}'_p-\mathbf{R}_p\right)} \mathbf{e}^{\dagger}_{\mathbf{q}} D^{\mathrm{ph}}_{\mathbf{q}} \mathbf{e}_{\mathbf{q}}. \tag{2.61}$$

The EPI vertex $g^{\mathrm{SE}}_{ji,\nu}(\mathbf{k},\mathbf{q})$ in Eq. (2.42) and (2.33) is given by

$$g^{\mathrm{SE}}_{ji,\nu}(\mathbf{k},\mathbf{q}) = \left(\frac{\hbar}{2m_0\omega_{\nu,\mathbf{q}}}\right)^{1/2} \langle j,\mathbf{k}+\mathbf{q}|\,\partial_{\nu,\mathbf{q}}V\,|i,\mathbf{k}\rangle, \tag{2.62}$$

where m_0 is a convenient reference mass, and $\partial_{\nu,\mathbf{q}}V$ is the derivative of the effective potential with respect to a collective phonon state (ν, $\mathbf{q}$). The bare EPI vertex is further defined as $g_{ji,\nu}(\mathbf{k},\mathbf{q}) = \langle j,\mathbf{k}+\mathbf{q}|\,\partial_{\nu,\mathbf{q}}V\,|i,\mathbf{k}\rangle$. It is well known that it is a non-trivial task to converge the self-energy through integral in Eq. (2.42) and (2.33), which needs extremely fine sampling of

electron, phonon states and EPI vertex [43, 44]. The accurate and efficient interpolation of EPI vertex can be realized via exploring the spatial localization in the Wannier representation. By projecting the collective atomic displacments onto the real space $\langle \boldsymbol{\tau}_{\mathbf{R}_p,a} | \nu, \mathbf{q} \rangle = e^{i\mathbf{q}\cdot\mathbf{R}_p} \mathbf{e}^{\nu}_{\mathbf{q},a}$, the derivative of the effective potential with respect to collective vibrations can be expressed by the Fourier transform of the derivative of the effective potential with respect to a localized atomic displacement

$$\partial_{\nu,\mathbf{q}} V = \sum_{a,\mathbf{R}_p} e^{i\mathbf{q}\cdot\mathbf{R}_p} \mathbf{u}^{\nu}_{\mathbf{q},a} \cdot \partial_{a,\mathbf{R}_p} V(\mathbf{r}), \tag{2.63}$$

where N_p is the number of unit cells in the supercell. The displacement field $\mathbf{u}^{\nu}_{\mathbf{q},a}$ is expressed in terms of phonon eigenmode $\mathbf{e}_{\mathbf{q}}$

$$\mathbf{u}^{\nu}_{\mathbf{q},a} = (m_0/m_\kappa)^{1/2} \mathbf{e}^{\nu}_{\mathbf{q},a}, \tag{2.64}$$

where a is the atomic index in the unit cell.The bare EPI vertex without prefactor $g_{ji,\nu}(\mathbf{k},\mathbf{q})$ can be transformed into the Wannier representation

$$g(\mathbf{R}_e, \mathbf{R}_p) = \langle \mathbf{0}_e | \, \partial_{\mathbf{R}_p} V \, | \mathbf{R}_e \rangle = \frac{1}{N_p} \sum_{\mathbf{k},\mathbf{q}} e^{-i\left(\mathbf{k}\cdot\mathbf{R}_e + \mathbf{q}\cdot\mathbf{R}_p\right)} U^{\dagger}_{\mathbf{k}+\mathbf{q}} g(\mathbf{k},\mathbf{q}) \, U_{\mathbf{k}} \mathbf{u}^{-1}_{\mathbf{q}}. \tag{2.65}$$

As we can see in Eq. (2.60) and (2.61), the spatial localization of the Hamiltonian in the Wannier representation can be achieved by constructing unitary transform matrix that leads to localized Wannier functions, while the spatial localization of the dynamical matrix in the Wannier representation can be achieved if IFC is short-ranged. Thus the spatial localization of EPI vertex can be explored by examining the spatial decay of Wannier functions and phonon perturbations. Detailed analysis by Giustino *et al.* indicates that the localization of bare EPI vertex is bound by two limiting cases $g(\mathbf{R}_e, \mathbf{0}_p)$ and $g(\mathbf{0}_e, \mathbf{R}_p)$ [27]. In the case of $g(\mathbf{R}_e, \mathbf{0}_p)$, its spatial decay is controlled by the localization of the electronic Wannier functions, while in the case of $g(\mathbf{0}_e, \mathbf{R}_p)$, its spatial decay is determined by the localization of phonon perturbations. This is illustrated

in Fig. 2.1. The slowest decay among these two limiting cases sets the size of the real-space supercell or the **k**-point sampling [27].

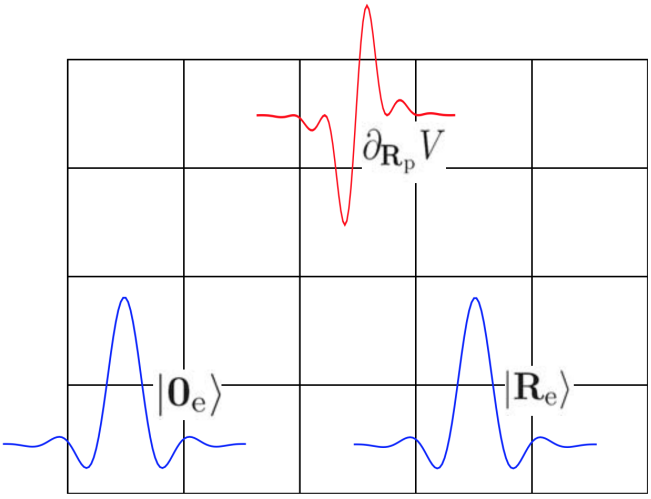

Figure 2.1: A schematic to demonstrate the spatial localization of electron-phonon interaction vertex by constructing localized Wannier functions and assuming phonon perturbations are localized. The square lattice indicates the unit cells of the crystal, the blue lines the electron Wannier functions $|\mathbf{0}_e\rangle$ and $|\mathbf{R}_e\rangle$ and the red line the phonon perturbation in the Wannier representation $\partial_{\mathbf{R}_p} V$. The electron-phonon matrix element is localized whenever two of these functions are centered on distant unit cells.

2.5.3 Wannier-Fourier Interpolation

Once the fast spatial decay of $g(\mathbf{R}_e, \mathbf{0}_p)$ and $g(\mathbf{0}_e, \mathbf{R}_p)$ has been verified, efficient and accurate interpolation of Hamiltonian and bare EPI vertex can be carried out by summing over a small set of lattice vectors with respect to both $\mathbf{R}_e$ and $\mathbf{R}_p$ where the matrix elements have large values. By extending to arbitrary electron $\mathbf{k}'$ and phonon $\mathbf{q}'$ wavevectors, we obtain

$$H^{\mathrm{el}}_{\mathbf{k}'} = U_{\mathbf{k}'} \left(\frac{1}{N_e} \sum_{\mathbf{R}_e} e^{i\mathbf{k}'\cdot\mathbf{R}_e} H^{\mathrm{el}}_{\mathbf{0}_e, \mathbf{R}_e} \right) U^{\dagger}_{\mathbf{k}'}, \tag{2.66}$$

$$D^{\mathrm{ph}}_{\mathbf{q}'} = \mathbf{e}^{\dagger}_{\mathbf{q}'} \left(\frac{1}{N_p} \sum_{\mathbf{R}_p} e^{i\mathbf{q}'\cdot\mathbf{R}_p} D^{\mathrm{ph}}_{\mathbf{0}_p,\mathbf{R}_p} \right) \mathbf{e}_{\mathbf{q}'}, \tag{2.67}$$

where $U_{\mathbf{k}'}\ \mathbf{e}_{\mathbf{q}'}$ can be obtained by directly diagonalizing the corresponding Hamiltonian, which can be further used to find the bare EPI vertex in the Bloch representation

$$g\left(\mathbf{k}',\mathbf{q}'\right) = \frac{1}{N_e} \sum_{\mathbf{R}_e,\mathbf{R}_p} e^{i\left(\mathbf{k}'\cdot\mathbf{R}_e + \mathbf{q}'\cdot\mathbf{R}_p\right)} \cdot U_{\mathbf{k}'+\mathbf{q}'} g\left(\mathbf{R}_e,\mathbf{R}_p\right) U^{\dagger}_{\mathbf{k}'} \mathbf{u}_{\mathbf{q}'}. \tag{2.68}$$

References

[1] P. Hohenberg and W. Kohn. Inhomogeneous electron gas. *Phys. Rev.*, 136:B864–B871, Nov 1964.

[2] W. Kohn and L. J. Sham. Self-consistent equations including exchange and correlation effects. *Phys. Rev.*, 140:A1133–A1138, Nov 1965.

[3] R. O. Jones and O. Gunnarsson. The density functional formalism, its applications and prospects. *Rev. Mod. Phys.*, 61:689–746, Jul 1989.

[4] John P. Perdew and Yue Wang. Accurate and simple analytic representation of the electron-gas correlation energy. *Phys. Rev. B*, 45:13244–13249, Jun 1992.

[5] JP Perdew, K. Burke, and M. Ernzerhof. Generalized gradient approximation made simple. *Phys. Rev. Lett.*, 78(7):1396–1396, 1997.

[6] J. P. Perdew and Alex Zunger. Self-interaction correction to density-functional approximations for many-electron systems. *Phys. Rev. B*, 23:5048–5079, May 1981.

[7] D. M. Ceperley and B. J. Alder. Ground state of the electron gas by a stochastic method. *Phys. Rev. Lett.*, 45:566–569, Aug 1980.

[8] M. C. Payne, M. P. Teter, D. C. Allan, T. A. Arias, and J. D. Joannopoulos. Iterative minimization techniques for *ab initio* total-energy calculations: molecular dynamics and conjugate gradients. *Rev. Mod. Phys.*, 64:1045–1097, Oct 1992.

[9] A. van de Walle and G. Ceder. Correcting overbinding in local-density-approximation calculations. *Phys. Rev. B*, 59:14992–15001, Jun 1999.

[10] John P. Perdew and Wang Yue. Accurate and simple density functional for the electronic exchange energy: Generalized gradient approximation. *Phys. Rev. B*, 33:8800–8802, Jun 1986.

[11] Stefano Baroni, Stefano de Gironcoli, Andrea Dal Corso, and Paolo Giannozzi. Phonons and related crystal properties from density-functional perturbation theory. *Rev. Mod. Phys.*, 73:515–562, Jul 2001.

[12] Xavier Gonze. Perturbation expansion of variational principles at arbitrary order. *Phys. Rev. A*, 52:1086–1095, Aug 1995.

[13] Xavier Gonze. Adiabatic density-functional perturbation theory. *Phys. Rev. A*, 52:1096–1114, Aug 1995.

[14] R. M. Sternheimer. Electronic polarizabilities of ions from the hartree-fock wave functions. *Phys. Rev.*, 96:951–968, Nov 1954.

[15] W. Jones and N.H. March. *Theoretical Solid State Physics: Perfect lattices in equilibrium*. Dover Books on Physics Series. Dover Publications, 1973.

[16] J.M. Ziman. *Electrons and Phonons: The Theory of Transport Phenomena in Solids*. International series of monographs on physics. OUP Oxford, 1960.

[17] Wu Li, L. Lindsay, D. A. Broido, Derek A. Stewart, and Natalio Mingo. Thermal conductivity of bulk and nanowire $Mg_2Si_xSn_{1-x}$ alloys from first principles. *Phys. Rev. B*, 86:174307, Nov 2012.

[18] M Omini and A Sparavigna. An iterative approach to the phonon boltzmann equation in the theory of thermal conductivity. *Physica B: Condensed Matter*, 212(2):101 – 112, 1995.

[19] M. Omini and A. Sparavigna. Beyond the isotropic-model approximation in the theory of thermal conductivity. *Phys. Rev. B*, 53:9064–9073, Apr 1996.

[20] D. A. Broido, M. Malorny, G. Birner, Natalio Mingo, and D. A. Stewart. Intrinsic lattice thermal conductivity of semiconductors from first principles. *Appl. Phys. Lett.*, 91(23):–, 2007.

[21] A. Ward, D. A. Broido, Derek A. Stewart, and G. Deinzer. *Ab initio* theory of the lattice thermal conductivity in diamond. *Phys. Rev. B*, 80:125203, Sep 2009.

[22] L Lindsay and D A Broido. Three-phonon phase space and lattice thermal conductivity in semiconductors. *J. Phys.: Condens. Matter*, 20(16):165209, 2008.

[23] B. Abeles. Lattice thermal conductivity of disordered semiconductor alloys at high temperatures. *Phys. Rev.*, 131:1906–1911, Sep 1963.

[24] Shin-ichiro Tamura. Isotope scattering of dispersive phonons in ge. *Phys. Rev. B*, 27:858–866, Jan 1983.

[25] Bolin Liao, Bo Qiu, Jiawei Zhou, Samuel Huberman, Keivan Esfarjani, and Gang Chen. Significant reduction of lattice thermal conductivity by the electron-phonon interaction in silicon with high carrier concentrations: A first-principles study. *Phys. Rev. Lett.*, 114:115901, Mar 2015.

[26] G.D. Mahan. *Many-Particle Physics*. Physics of Solids and Liquids. Springer, 2000.

[27] Feliciano Giustino, Marvin L. Cohen, and Steven G. Louie. Electron-phonon interaction using wannier functions. *Phys. Rev. B*, 76:165108, Oct 2007.

[28] J.M. Ziman. *Electrons and Phonons: The Theory of Transport Phenomena in Solids*. International series of monographs on physics. OUP Oxford, 1960.

[29] Georg K.H. Madsen and David J. Singh. Boltztrap. a code for calculating band-structure dependent quantities. *Comput. Phys. Commun.*, 175(1):67 – 71, 2006.

[30] David J. Singh. Doping-dependent thermopower of pbte from boltzmann transport calculations. *Phys. Rev. B*, 81:195217, May 2010.

[31] David Parker and David J. Singh. Potential thermoelectric performance from optimization of hole-doped bi_2se_3. *Phys. Rev. X*, 1:021005, Oct 2011.

[32] Fei Zhou, Weston Nielson, Yi Xia, and Vidvuds Ozoliņš. Lattice anharmonicity and thermal conductivity from compressive sensing of first-principles calculations. *Phys. Rev. Lett.*, 113:185501, Oct 2014.

[33] Xavier Gonze and Changyol Lee. Dynamical matrices, born effective charges, dielectric permittivity tensors, and interatomic force constants from density-functional perturbation theory. *Phys. Rev. B*, 55:10355–10368, Apr 1997.

[34] E. J. Candes and T. Tao. Decoding by linear programming. *IEEE Transactions on Information Theory*, 51(12):4203–4215, Dec 2005.

[35] Emmanuel J. Candès, Justin K. Romberg, and Terence Tao. Stable signal recovery from incomplete and inaccurate measurements. *Communications on Pure and Applied Mathematics*, 59(8):1207–1223, 2006.

[36] E. J. Candes, J. Romberg, and T. Tao. Robust uncertainty principles: exact signal reconstruction from highly incomplete frequency information. *IEEE Transactions on Information Theory*, 52(2):489–509, Feb 2006.

[37] E. J. Candes and M. B. Wakin. An introduction to compressive sampling. *IEEE Signal Processing Magazine*, 25(2):21–30, March 2008.

[38] Gregory H. Wannier. The structure of electronic excitation levels in insulating crystals. *Phys. Rev.*, 52:191–197, Aug 1937.

[39] Nicola Marzari and David Vanderbilt. Maximally localized generalized wannier functions for composite energy bands. *Phys. Rev. B*, 56:12847–12865, Nov 1997.

[40] R. D. King-Smith and David Vanderbilt. Theory of polarization of crystalline solids. *Phys. Rev. B*, 47:1651–1654, Jan 1993.

[41] Lixin He and David Vanderbilt. Exponential decay properties of wannier functions and related quantities. *Phys. Rev. Lett.*, 86:5341–5344, Jun 2001.

[42] Ivo Souza, Nicola Marzari, and David Vanderbilt. Maximally localized wannier functions for entangled energy bands. *Phys. Rev. B*, 65:035109, Dec 2001.

[43] M. A. L. Marques, M. Lüders, N. N. Lathiotakis, G. Profeta, A. Floris, L. Fast, A. Continenza, E. K. U. Gross, and S. Massidda. *Ab initio* theory of superconductivity. ii. application to elemental metals. *Phys. Rev. B*, 72:024546, Jul 2005.

[44] Deepa Kasinathan, K. Koepernik, J. Kuneš, H. Rosner, and W.E. Pickett. Origin of strong coupling in lithium under pressure. *Physica C*, 460:133 – 136, 2007.

CHAPTER 3

First-Principles Study of Lattice Thermal Conductivity of Cu_3SbS_4 and Cu_3SbSe_4

3.1 Introduction

Recently, good thermoelectric properties have been identified in several compounds composed of earth-abundant and non-toxic elements [1, 2, 3, 4, 5, 6]. Ternary zincblende-based compounds Cu_3SbS_4 and Cu_3SbSe_4 are two examples of such materials. Skoug *et al.* achieved high thermoelectric figures of merit ($zT \approx 0.9$ at 650 K) in Cu_3SbS_4-Cu_3SbSe_4 solid solutions with Sb substituted by Ge [2]. Yang *et al.* studied Cu_3SbSe_4 by doping Sn on the Sb site and obtained $ZT = 0.75$ at 673 K [7]. Bismuth doping on the Sb site performed by Li *et al.* achieved a maximum ZT of 0.7 at 600 K [8]. In Cu_3SbS_4, an improvement in the thermoelectric properties of Se-free compounds can be accomplished by substituting Ag for Cu and Ge for Sb [9].

One of the main factors holding back further improvement in the thermoelectric efficiencies of Cu_3SbS_4 and Cu_3SbSe_4 is their relatively high thermal conductivity. The measured room temperature lattice thermal conductivity of Cu_3SbSe_4 [3], $\kappa_l = 3.1$ W m^{-1} K^{-1}, is significantly above its theoretical minimum value [10], $\kappa_{\text{min}} = 0.47$ W m^{-1} K^{-1}, suggesting that significant reduction of κ_l is possible. In an effort to understand thermal transport properties, lattice thermal conductivity in Cu_3SbS_4-Cu_3SbSe_4 solid solutions has been experimentally measured and analyzed with the Debye model [11, 12] by taking into account mass scattering and size difference

between S and Se [3]. Transport mechanisms in Sn-doped p-type Cu_3SbSe_4 have been further investigated by Wei *et al* [13]. Zhang *et al.* used first-principles density-functional theory (DFT) calculations of the phonon dispersion and mode Grüneisen parameters in conjunction with the Debye-Callaway model to predict κ_l of Cu_3SbSe_4 [14]. They found that the calculated κ_l was underestimated by more than 30% and attributed this discrepancy to the neglect of contributions from optical phonon modes in the Debye-Callaway model.

We provide a theoretical study of phonon scattering and lattice thermal conductivity for Cu_3SbS_4 and Cu_3SbSe_4 and evaluate opportunities to achieve further reduction of κ_l in these materials by doping, alloying, and nanostructuring. First-principles DFT calculations in conjunction with the compressive sensing lattice dynamics (CSLD) method [15] are used to obtain the second and third-order anharmonic force constants. The first-order phonon perturbation theory [16] and the self-consistent Boltzmann transport equation [17, 18] are used to calculate phonon mode lifetimes, phonon mean free paths (MFPs), and their contributions to κ_l. The calculated κ_l values are in good agreement with experimental measurements for both compounds. We show that optical phonon modes account for a sizable ($\approx 25\%$) fraction of the total κ_l in both compounds, confirming the conclusions of Zhang *et al* [14]. Spectral analysis of the cumulative κ_l in terms of MFP shows that approximately 80% of total κ_l in both compounds is due to phonons with MFPs above 10 nanometers. We suggest that further improvement in the thermoelectric properties can be realized by nanostructuring—forming coherent nanoscale precipitates of another phase or reducing the average grain size. Calculations using anharmonic force constants obtained from the virtual crystal approximation and including mass disorder show strong reduction of κ_l in $Cu_3SbS_{4x}Se_{4(1-x)}$ solid solutions. This reduction is particularly pronounced at both ends of the composition spectrum, where the theoretical model is in very good agreement with experimental data, suggesting that mass disorder accounts for most of the additional phonon scattering. However, at intermediate compositions (with x between 20% and 80%) the calculated κ_l significantly

overestimates experimental values, which we attribute to inadequate treatment of the force constant disorder due to S/Se substitution, neglect of defect scattering and strain effect. Our results underscore the need for developing theoretical methods that can accurately predict vibrational and thermal transport properties of disordered alloys.

3.2 Computational Details

3.2.1 DFT Calculations

Structure relaxation and self-consistent calculations were performed by Vienna *Ab initio* simulation package (VASP) [19, 20, 21, 22, 23] with the projector-augmented wave (PAW) [24] method using the Perdew-Becke-Ernzerhof (PBE) [25] generalized gradient approximation (GGA) [26] for the exchange-correlation (xc) functional [19]. For the structure relaxation a plane wave basis with cutoff energy of 800 eV and a Monkhorst-Pack **k**-point mesh of $7\times7\times7$ were used. The energy convergence threshold was set to 10^{-7} eV per primitive cell and forces were converged to be less than 10^{-3} eV/Å. IFCs are fitted using fifteen supercell structures. It is important to note that the PBE and other GGA functionals predict metallic band structures for Cu_3SbS_4 and Cu_3SbSe_4, while experimentally both are narrow band gap semiconductors [27, 28]. The process of band gap formation in these compounds is subtle and can be understood using non-local hybrid exchange functionals [29, 30, 31]: the band gap is related to hybridization between the Sb 5*s* and neighboring chalcogen (S, Se) valence *s* and *p* orbitals, which in turn depends on the interatomic bond lengths and interactions with the Cu 3*d* states [32]. Since hybrid exchange calculations for large supercells are computationally prohibitive and the effect of nonlocal exchange on κ_l is expected to be small because it is not expected to affect the acoustic phonons significantly, we used the GGA functional instead. Hence, the LO/TO splitting is absent in the calculated phonon dispersion curves due to the fact that both compounds are metallic within

GGA.

3.2.2 Fitting IFCs

We included up to 25 and 6 neighbor shells for second- and third-order interactions respectively, which give rise to 1,146 symmetrically distinct elements out of 2,118 IFCs. Fifteen supercell structures each containing a total of 512 atoms for each compound with random atomic displacements ranging from 0.01 to 0.05 Å were used as training and validation sets. The optimal μ in Eq. (2.55) was selected from a list of values in which the minimum value gives rise to overfitting while the maximum value leads to underfitting using random sub-sampling validation, in which randomly selected $\approx$70% of forces were used for training and the rest for validation. Afterwards, multiple independent fittings of IFCs were carried out using optimized μ and training set of randomly selected $\approx$90% of forces. Fig. 3.1 shows the comparison between our predicted forces and those directly calculated by VASP for Cu_3SbS_4 and Cu_3SbSe_4. Small relative errors of 2.34% and 2.58% verify the utilized cutoffs for second- and third-order interactions and indicate good accuracy of fitted IFCs as well. Fig. 3.2 shows the Frobenius norm of calculated second- and third-order IFCs with increasing interaction distances, both of which exhibit spatial localization. Second-order IFCs are vanishing with interaction distance larger than 6 Å while considerable third-order IFCs are restricted within 3 Å. Detailed analysis and comparison of third-order IFCs are shown in Fig. 3.3. Since there are two symmetrically distinctive Cu atoms in a primitive cell, they are denoted as Cu_1 and Cu_2 respectively. Third-order IFCs with Frobenius norm larger than 5 eV $Å^{-3}$ are all associated with one- (onsite $\Phi_{\mathbf{aaa}}$) or two-body (nearest-neighbor $\Phi_{\mathbf{abb}}$) interactions. To calculate κ_l, a range of phonon wave vector $\mathbf{q}$ mesh sizes were used to check the convergence with respect to Brillouin zone sampling. It was found that the results achieved good convergency of 3% using a mesh size of $11\times11\times11$ and $scalebroad = 0.6$ [33]. Fig. 3.4 shows the calculated κ_l at 300 K for Cu_3SbS_4 and Cu_3SbSe_4 using IFCs obtained from 10 independent

fittings. The averaged values are 4.1 and 3.1 W m^{-1} K^{-1} respectively. The deviations from different fittings are all within $\pm 3\%$.

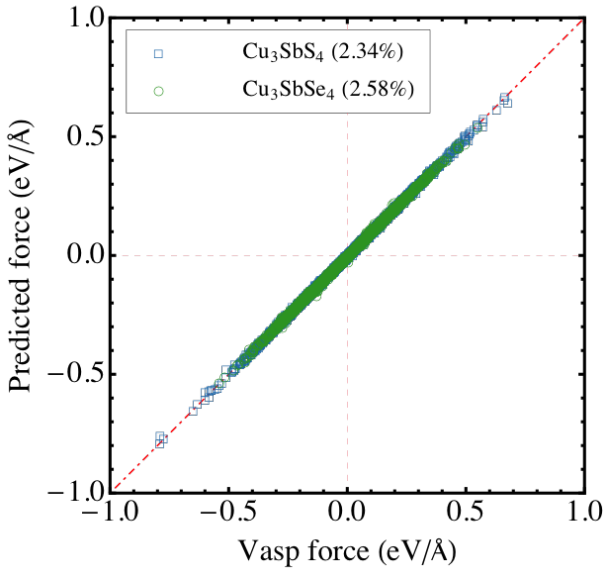

Figure 3.1: Comparison between forces predicted by fitted IFCs and those directly from VASP calculation. The red dot dashed line is a diagonal representing exact fit. Relative error for predicted forces is indicated in the legends.

3.3 Results and Discussion

3.3.1 Crystal Structure

Cu_3SbS_4 and Cu_3SbSe_4 belong to the chalcopyrite class of compounds (Fig. 3.5) with tetragonal (space group $I\bar{4}2m$) cation-ordered crystal structures based on the zincblende lattice [34, 35]. All cations are tetrahedrally coordinated by anions (and vice versa), and there are two inequivalent Cu atoms in a unit cell. The relaxed DFT (experimental [34, 35]) lattice constants for Cu_3SbS_4 and Cu_3SbSe_4 are $a = 5.43$ (5.39) Å, $c = 10.85$ (10.75) Å and $a = 5.73$ (5.66) Å, $c = 11.42$ (11.28) Å, respectively, showing that they are slightly overestimated by the PBE exchange-correlation functional. The Se-Sb bond length predicted by PBE, $d = 2.65$ Å differs from the value $d =$

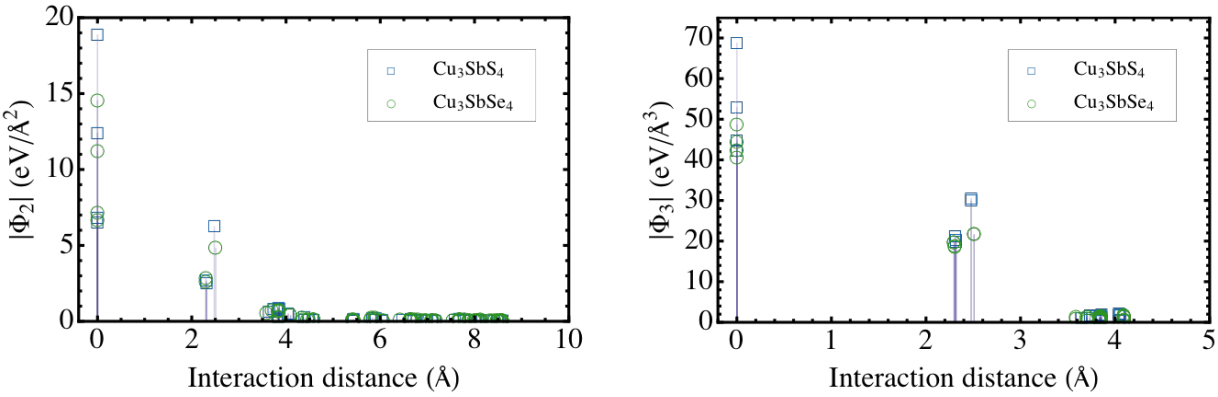

Figure 3.2: Frobenius norm of calculated second- and third-order IFCs versus interaction distance defined as the maximum distance between atoms.

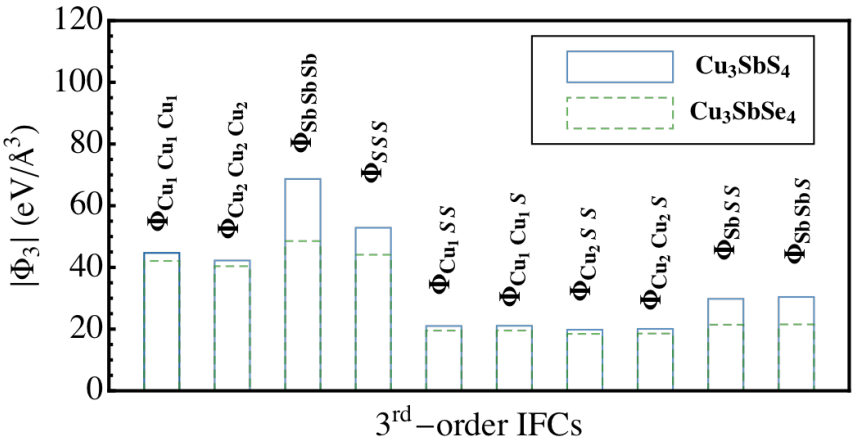

Figure 3.3: Comparison of third-order IFCs between Cu_3SbS_4 and Cu_3SbSe_4.

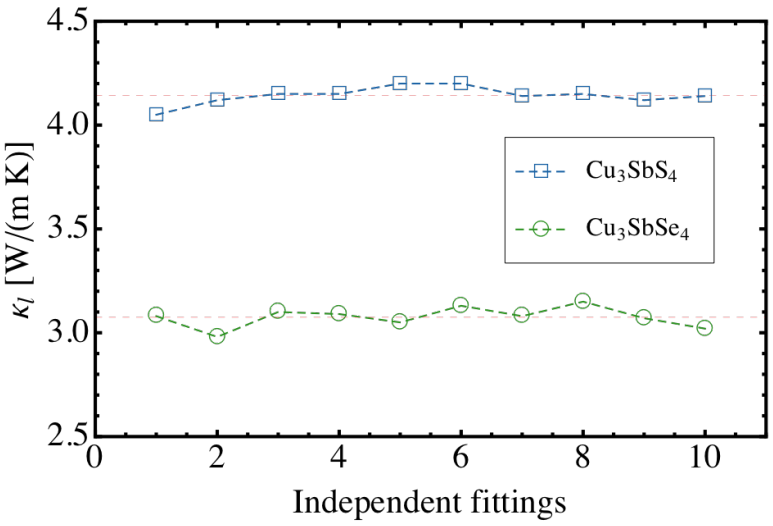

Figure 3.4: Calculated lattice thermal conductivities for Cu_3SbS_4 (blue square) and Cu_3SbSe_4 (green circle) from 10 independent fittings. The red dashed lines denote the corresponding averaged lattice thermal conductivities.

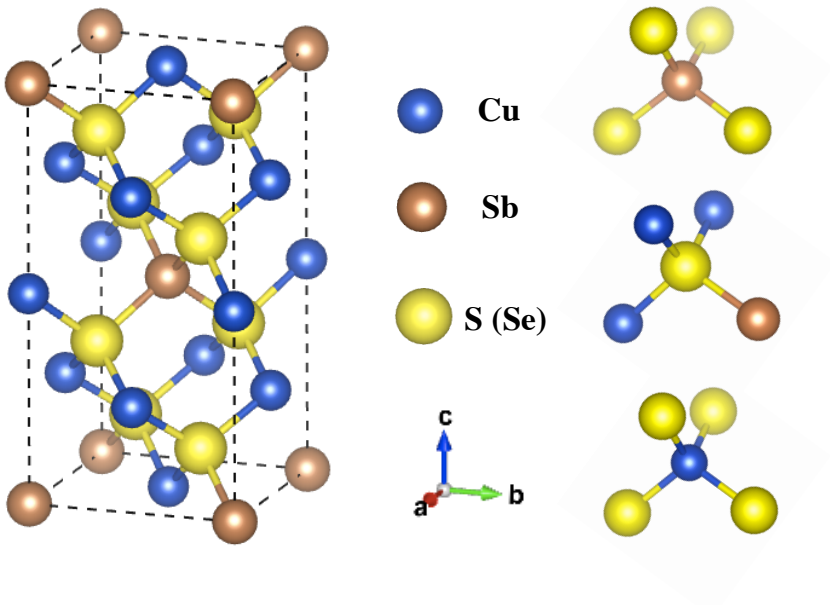

Figure 3.5: Crystal structures of Cu_3SbS_4 and Cu_3SbSe_4. Cu, Sb and S (Se) atoms are indicated by blue, brown and yellow solid spheres.

2.53 Å obtained using the hybrid exchange functional in Ref. [32]. Since the hybrid functional correctly predicts the formation of a band gap, we consider the latter to be more accurate. This discrepancy may affect the calculated S-Sb and Se-Sb IFCs and therefore change the optical mode frequencies and anharmonic terms that involve stretching of these bonds; we consider this to be the main source of systematic error in the present study. However, based on the good agreement between the calculated and measured κ_l, it appears that PBE correctly captures the main features of phonon-phonon scattering in these compounds.

3.3.2 IFCs and Phonon Dispersion

The adopted finite cutoffs for second- and third-order interaction distances are verified by examining the spatial decay of Frobenius norm of IFCs with increased interaction distance in Fig. 3.2. An important feature is that both second- and third-order IFCs are quite short-ranged and vanishing with interaction distance larger than 6.0 Å and 3.0 Å respectively for both compounds. Comparison of the calculated IFCs shows that most second- and third-order IFCs of Cu_3SbS_4 are larger than those of Cu_3SbSe_4, which probably can be attributed to the difference in chemical environment between S and Se. Detailed analysis of third-order IFCs in Fig. 3.3 indicates: (1) one-body interactions ($\Phi_{Cu_1Cu_1Cu_1}, \Phi_{Cu_2Cu_2Cu_2}, \Phi_{SbSbSb}, \Phi_{SSS}$) are all stronger than two-body interactions ($\Phi_{Cu_1Cu_1S}$, Φ_{Cu_1SS}, $\Phi_{Cu_2Cu_2S}$, Φ_{Cu_2SS}, Φ_{SbSS}, Φ_{SbSbS}); (2) both one- and two-body interactions involving displacements of Sb have larger values. The latter indicates that the s^2 lone pairs of Sb [32] play a key part in reducing κ_l in these compounds; similar lone pair effects have been suggested to cause anharmonic phonon-phonon interactions in other systems [36, 37, 38].

The calculated harmonic phonon dispersion curves and atom projected density of states are shown in Fig. 3.6. Phonon dispersions of these two compounds resemble each other in the acoustic and low-frequency optical region from 0 to 20 meV, in which the vibrations involve Cu, Sb and S(Se). As expected, the acoustic frequencies and group velocities are slightly lower in the

Se compound, and the bulk of this effect can be attributed to the total mass difference between the atoms in these two unit cells ($\approx 16\%$); the stiffer interatomic bonds in the S compound play a minor role. This conclusion has been verified comparing the phonon dispersion of Cu_3SbSe_4 and the recalculated phonon dispersion of Cu_3SbS_4 by replacing the mass of S with that of Se while keeping the IFCs of the former. In contrast, the group of high-frequency optical modes involving mostly vibrations of the chalcogen anions show a much more pronounced difference: in Cu_3SbS_4 there is a large phonon band gap of about 8 meV, whereas for Cu_3SbSe_4 the gap is very small (≈ 1 meV). The effect of mass difference on these high-frequency optical modes is more profound because their frequencies scale with the inverse square root of the mass of the anion. This phonon band gap is responsible for a significant difference in the Debye temperatures of these two compounds. Furthermore, since the acoustic modes of acoustic modes usually contribute more to heat conduction than optical modes, larger group velocities in Fig. 3.6 suggest that κ_l in Cu_3SbS_4 is higher, in agreement with the full calculations described below. Optical modes with frequencies above 20 meV are relatively flat and expected to have less influence on the total κ_l, which is also verified by the our calculation.

3.3.3 Lattice Thermal Conductivity

Fig. 3.7 shows the calculated and experimental κ_l for Cu_3SbS_4 and Cu_3SbSe_4. Small anisotropy is present in both compounds: κ_{xx} along the shorter lattice vectors of unit cell (see Fig. 3.5) is 0.44 (0.18) W m^{-1} K^{-1} higher than κ_{zz} along the longer lattice vector at 300 K for Cu_3SbS_4 (Cu_3SbSe_4). In general, we see very good agreement with experimental measurements, suggesting that the deficiencies of the GGA predictions for the band gaps in these compounds have a minor effect on κ_l. Our calculated κ_l is slightly underestimated for Cu_3SbSe_4 below 300 K, while exhibit systematic overestimation at high temperatures ($\geqslant 400$ K) for both compounds. The overestimation probably can be attributed to two major factors: (1) increasing phonon scattering

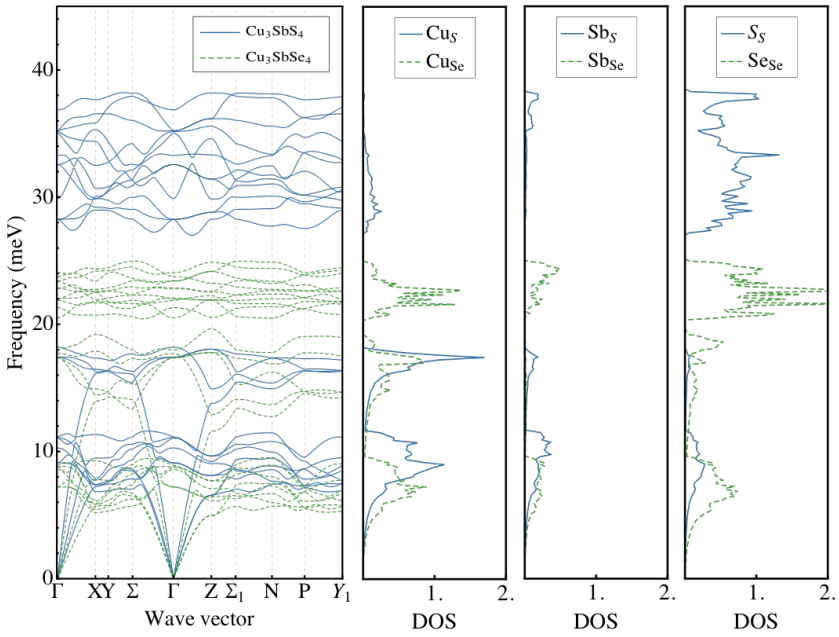

Figure 3.6: Calculated phonon dispersion curves and atom-projected phonon density of states for Cu_3SbS_4 (solid blue line) and Cu_3SbSe_4 (dashed green line). Dashed vertical lines indicate high-symmetry points in the first Brillouin zone.

by charge carriers and (2) increasing importance of phonon-phonon interactions arising from higher-order anharmonicity (renormalization of both harmonic and anharmonic IFCs); these effects are not included in this study.

In order to understand the difference in κ_l between Cu_3SbS_4 and Cu_3SbSe_4, we compare the phonon mode group velocities, lifetimes, and MFPs in Fig. 3.8 (a), (b) and (c) respectively. From Fig. 3.8 (a) we see that phonon modes with group velocities larger than 1.0 k m s^{-1} mainly consist of acoustic and low-frequency optical modes ($\leqslant$ 20 meV). In this frequency window, slightly larger group velocities are found in Cu_3SbS_4 except a narrow frequency interval around 11 meV, where Cu_3SbS_4 retains flat dispersion while Cu_3SbSe_4 exhibit dispersive character. Meanwhile, Cu_3SbS_4 also has slightly longer lifetimes below 10 meV and shows a sharp decrease around 11 meV in Fig. 3.8 (b). The phonon MFPs, shown in Fig. 3.8 (c), illustrate the combined effect of lifetime and group velocity. Overall longer MFPs for acoustic and low-frequency optical

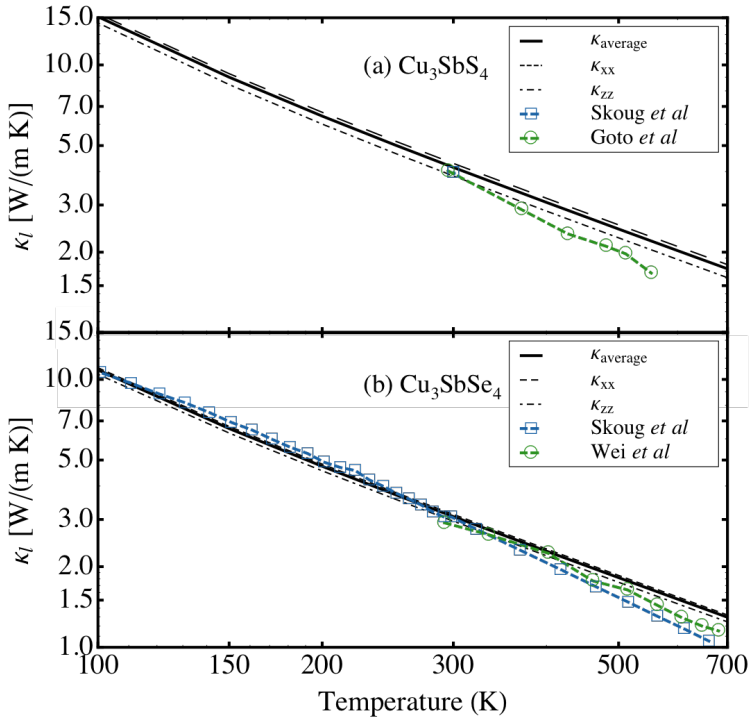

Figure 3.7: Calculated lattice thermal conductivities versus temperatures for Cu_3SbS_4 and Cu_3SbSe_4, compared with experimental data of Skoug *et al.* (Ref. [2, 3]), Wei *et al.* (Ref. [13]) and Goto *et al.* (Ref. [28]).

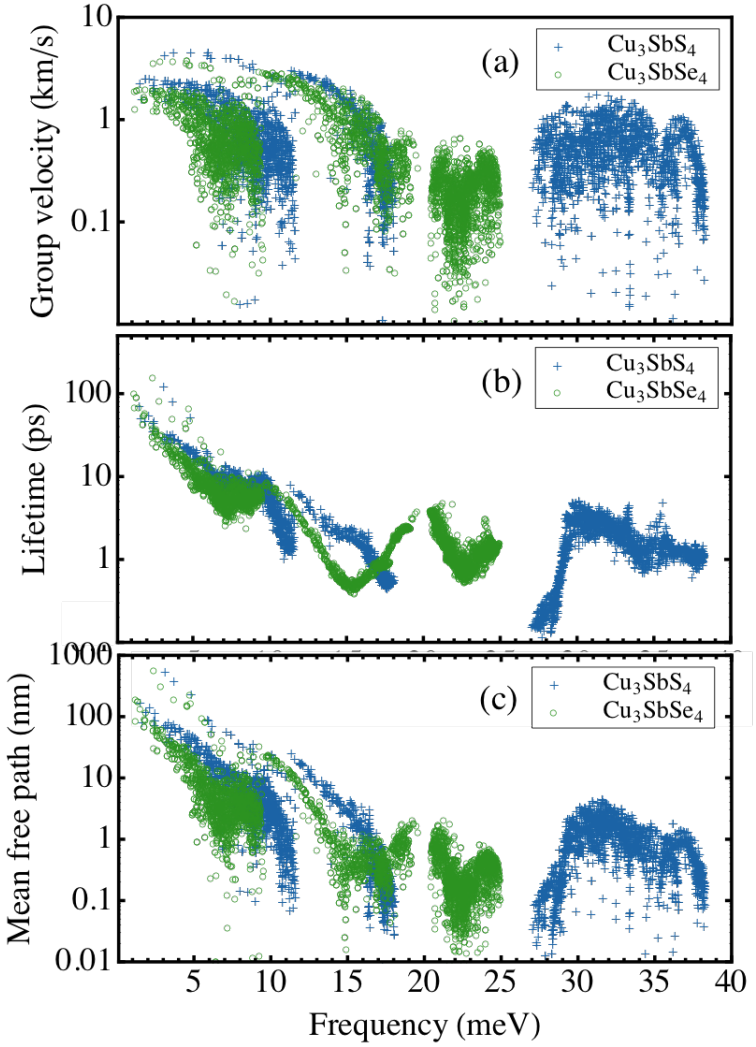

Figure 3.8: Calcualted phonon group velocity, lifetime and mean free path versus frequency for Cu_3SbS_4 (blue cross) and Cu_3SbSe_4 (green circle).

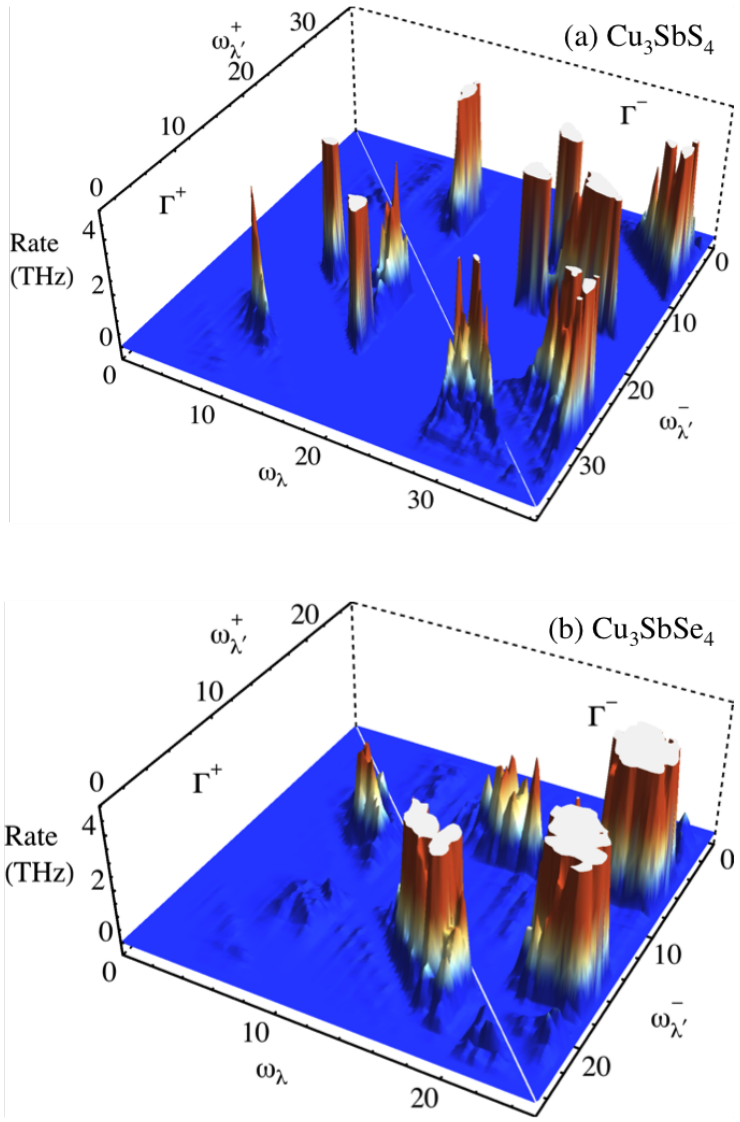

Figure 3.9: Scattering rares Γ^+ and Γ^- for (a) Cu_3SbS_4 and (b) Cu_3SbSe_4 at 300 K. The left segment shows the absorption rates, whereas the right panel indicates the rates for emission processes. The corresponding phonon frequency ω are in units of meV.

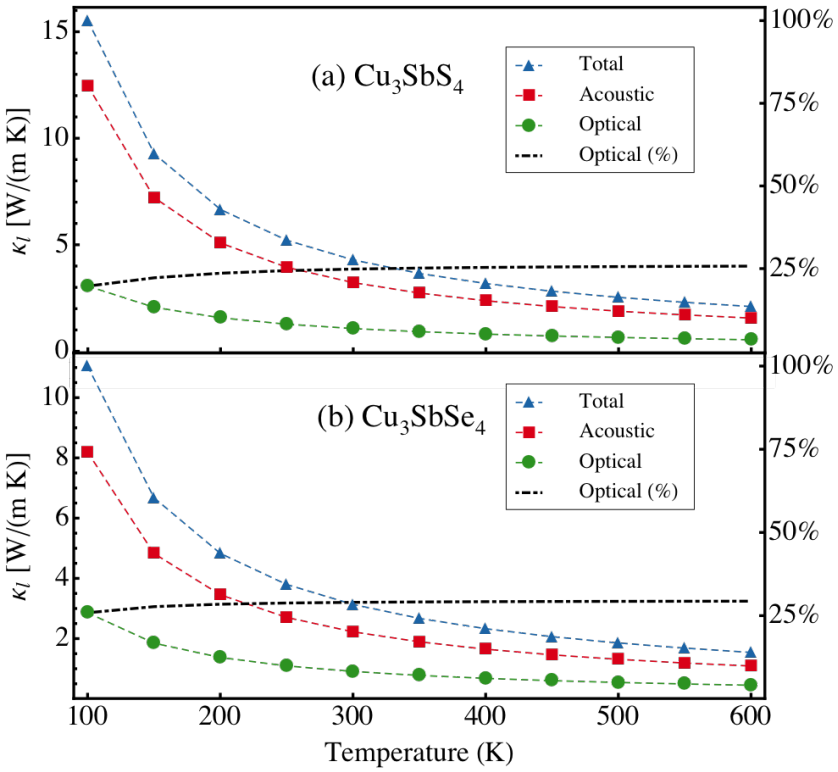

Figure 3.10: Acoustic and optical modes decomposed lattice thermal conductivities versus temperature for Cu_3SbS_4 and Cu_3SbSe_4. Solid triangle denotes the total lattice thermal conductivity while the solid square and solid circle represent the contribution from acoustic and optical phonons respectively. Black dot dashed line shows the percentage contribution from optical modes.

modes are found in Cu_3SbS_4. MFPs of high-frequency optical phonon modes (> 20 meV) drop below 5 nm due to both reduced group velocity and lifetime. Because of strong anharmonic interactions, MFPs of some high-frequency optical modes are underestimated by the first-order perturbation theory, even dropping below the theoretical minimum given by the interatomic distance. Their contributions to κ_l are therefore underestimated by the perturbation theory, which could be a contributing factor to the slight underestimation of κ_l below 300 K in Cu_3SbSe_4. The calculated κ_l of Cu_3SbS_4 is higher than that of Cu_3SbSe_4 over the whole temperature range, as suggested by the slightly larger phonon group velocities and longer lifetimes below 20 meV in the former. Overall, our results agree with the assumption that the slightly larger group velocities and lifetimes of the acoustic and low-frequency optical modes lead to higher κ_l in Cu_3SbS_4.

To further understand the calculated lifetimes, we examine the scattering events in Fig. 3.9. The energy conservation constraint restricts the absorption and emission processes in the lower and upper triangular panels. In general, phonon modes with frequencies smaller than roughly 10 meV are mostly scattered in the absorption processes while high-frequency modes are also heavily scattered in emission processes. For Cu_3SbS_4, there are two major scattering rate peaks with $\omega_\lambda < 12$ meV, which correspond to absorptions involving ($\omega_\lambda \approx 8$ meV, $\omega_{\lambda'} \approx 8$ meV) and ($\omega_\lambda \approx 11$ meV, $\omega_{\lambda'} \approx 17$ meV). The latter is responsible for the sharp decrease of phonon mode lifetime around 11 meV. While Cu_3SbSe_4 has only one major scattering rate peak due to absorption involving ($\omega_\lambda \approx 7$ meV, $\omega_{\lambda'} \approx 15$ meV) in the same frequency window. For both compounds, the phonon modes with frequency range from 12 to 20 meV not only emit but also absorb low-frequency phonons ($\leqslant 10$ meV) and therefore have rather short lifetimes ($\leqslant 5$ ps). Compared with Cu_3SbSe_4, Cu_3SbS_4 additionally absorbs phonons with higher frequencies (≈ 16 meV). Scattering of high-frequency phonon modes (> 20 meV) are dominated by heavy emission processes, giving rise to short lifetimes.

In order to clarify the contributions to κ_l from acoustic and optical modes, we plot the polarization-

decomposed κ_l in Fig. 3.10. Absolute contributions from both acoustic and optical modes decrease with increasing temperature due to the enhanced scattering rates with larger phonon population at higher temperatures. We can see in Fig. 3.10 that for Cu_3SbS_4 contribution to total κ_l from optical modes increases approximately from 20% at 100 K to 25% at 600 K and for Cu_3SbSe_4 increases approximately from 26% at 100 K to 29% at 600 K. This indicates that over the whole temperature range, the contribution from optical modes cannot be neglected. This naturally explains the roughly 30% underestimation of κ_l calculated using the Debye-Callaway model in Ref. [14]. In addition, detailed analysis reveals that contribution from low-frequency optical modes ($\leqslant$ 20 meV) dominate over that from high-frequency optical modes.

3.3.4 Nanostructure

In crystals, heat is conducted via phonon modes with various MFPs [see Eq. (2.28)]. As a result, a simple estimation of the effect from nanostructures with given average size can be described by Eq. (2.29). In order to elucidate the effect of nanostructuring on κ_l, normalized cumulative κ_l at 300 K is shown in Fig. 3.11. Though Cu_3SbS_4 has larger κ_l than Cu_3SbSe_4, they share the same MFP range from about 1 to 900 nm. Compared to PbSe and PbTe, Cu_3SbS_4 and Cu_3SbSe_4 have a much wider range of MFP values. Nanostructuring with MFP less than 10 nm can reduce κ_l in Cu_3SbS_4 and Cu_3SbSe_4 to roughly 0.94 and 0.68 W m^{-1} K^{-1} respectively, while in PbSe and PbTe only about 25% of κ_l is reduced with the same scale [39]. Surprisingly, for both compounds κ_l is reduced by roughly 80% via suppressing the contribution from acoustic contribution with long MFPs. This indicates that nanostructuring is an effective and promising way to further reduce κ_l and achieve a higher ZT if carrier mobility is not heavily reduced at the same time.

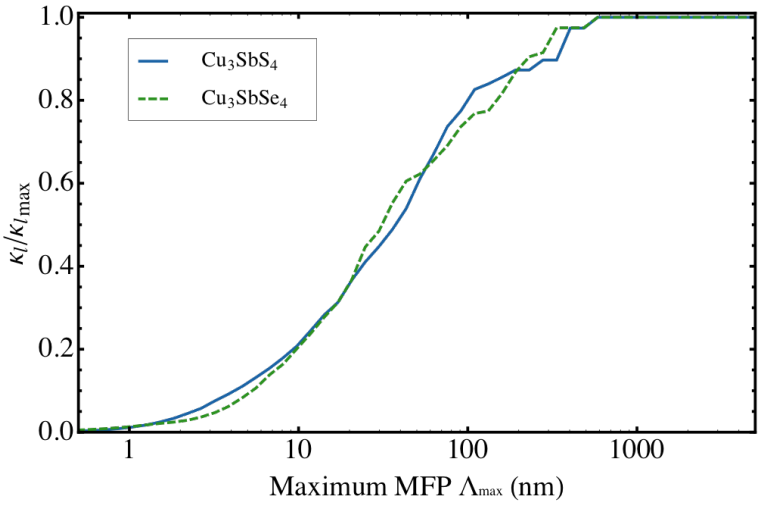

Figure 3.11: Calculated cumulative lattice thermal conductivities for Cu_3SbS_4 (solid line) and Cu_3SbSe_4 (dashed line) with respect to maximum mean free path at 300 K.

3.3.5 Alloy

Forming solid solution is another method that is capable of effectively reducing κ_l. Skoug *et al.* showed that a 76% reduction in κ_l at 80 K and 40% at 300 K for $Cu_3SbS_{4x}Se_{4(1-x)}$ can be achieved over a wide range of concentration [3] We use the virtual crystal model in which mass disorder and anharmonicity are treated as first-order perturbations [40, 39, 41, 42]. Calculated κ_l at different concentrations at 80 and 300 K is shown in Fig. 3.12. Good agreement with experimental results is found only at concentrations near 20% and 80%. Overestimations of κ_l as large as 67% and 27% are found at intermediate concentrations at 80 and 300 K respectively. We attribute the overestimation mainly to the neglect of defect scattering, strain effect and force constant disorder [43]. In addition, the large difference in fractional coordinates of S and Se in the relaxed structures of Cu_3SbSe_4 and Cu_3SbS_4 indicates that linearly interpolated IFCs is not an appropriate method for studying concentrated disordered alloys. However, rapid decrease in κ_l due to alloying is well reproduced, thus indicating the dominance of mass disorder over other scattering effects in dilute solid solution and low κ_l can be achieved in a relatively wide range of

concentrations (30 to 70%).

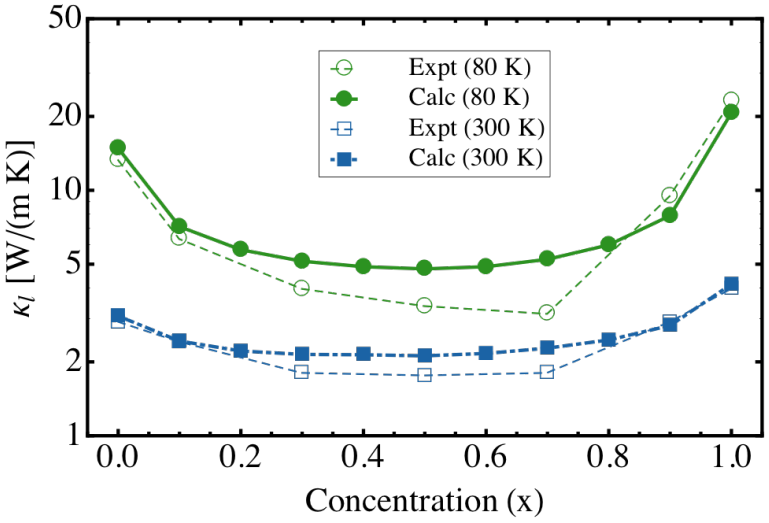

Figure 3.12: Calculated lattice thermal conductivities for $Cu_3SbS_{4x}Se_{4(1-x)}$ solid solution at 80 and 300 K, compared with experimental data of Skoug *et al* [3]. Solid squares and disks were calculated with linearly interpolated IFCs including mass disorder.

3.4 Conclusions

Interatomic force constants obtained by compressive sensing lattice dynamics were used to perform lattice thermal conductivity calculation and analysis of Cu_3SbS_4 and Cu_3SbSe_4 by solving the linearized Boltzmann transport equation iteratively. The total lattice thermal conductivity agrees well with experiments. κ_l of Cu_3SbS_4 is larger than that of Cu_3SbS_4 mainly due to the larger group velocities of low-frequency phonon modes because of lighter mass of the S atom and slightly longer lifetimes. Optical modes in these two compounds play an important role in total lattice thermal conductivity and thus cannot be neglected. Nanostructuring is promising in reducing κ_l for both systems up to 80% if characteristical length is less than 10 nm. Our simple alloying model including mass disorder reproduces rapid decrease in κ_l by forming solid solutions which is confirmed by experimental findings. These findings with respect to thermal transport properties may help in designing materials with high ZT by reducing lattice thermal

conductivity.

3.5 Acknowledgement

This work was supported by the Office of Naval Research (Grant No. N00014-14-1-0444) and used computing resources at the National Energy Research Scientific Computing Center (NERSC), which is supported by the US DOE under contract DE-AC02-05CH11231. The work by Fei Zhou was performed under the auspices of the US DOE by Lawrence Livermore National Laboratory under contract DE-AC52-07NA27344.

References

[1] Xu Lu, Donald T. Morelli, Yi Xia, Fei Zhou, Vidvuds Ozolins, Hang Chi, Xiaoyuan Zhou, and Ctirad Uher. High performance thermoelectricity in earth-abundant compounds based on natural mineral tetrahedrites. *Adv. Energy Mater.*, 3(3):342–348, 2013.

[2] Eric J. Skoug, Jeffrey D. Cain, and Donald T. Morelli. High thermoelectric figure of merit in the Cu_3SbSe_4-Cu_3SbS_4 solid solution. *Applied Physics Letters*, 98(26), 2011.

[3] Eric J. Skoug, Jeffrey D. Cain, Donald T. Morelli, Melanie Kirkham, Paul Majsztrik, and Edgar Lara-Curzio. Lattice thermal conductivity of the Cu_3SbSe_4-Cu_3SbS_4 solid solution. *Journal of Applied Physics*, 110(2), 2011.

[4] Huili Liu, Xun Shi, Fangfang Xu, Linlin Zhang, Wenqing Zhang, Lidong Chen, Qiang Li, Ctirad Uher, Tristan Day, and G. Jeffrey Snyder. Copper ion liquid-like thermoelectric. *Nat. Mater.*, 11(5):422–425, 2012.

[5] Koichiro Suekuni, Kojiro Tsuruta, Tomoki Ariga, and Mikio Koyano. Thermoelectric properties of mineral tetrahedrites $Cu_{10}Tr_2Sb_4S_{13}$ with low thermal conductivity. *Appl. Phys. Express*, 5(5):051201, 2012.

[6] Koichiro Suekuni, Kojiro Tsuruta, Masaru Kunii, Hirotaka Nishiate, Eiji Nishibori, Sachiko Maki, Michihiro Ohta, Atsushi Yamamoto, and Mikio Koyano. High-performance thermoelectric mineral $Cu_{12-x}Ni_xSb_4S_{13}$ tetrahedrite. *J. Appl. Phys.*, 113(4):–, 2013.

[7] Chongyin Yang, Fuqiang Huang, Liming Wu, and Ke Xu. New stannite-like p-type thermoelectric material Cu_3SbSe_4. *J. Phys. D*, 44(29):295404, 2011.

[8] X.Y. Li, D. Li, H.X. Xin, J. Zhang, C.J. Song, and X.Y. Qin. *Journal of Alloys and Compounds*, 561(0):105–108, 2013.

[9] Akitoshi Suzumura, Masaki Watanabe, Naoyuki Nagasako, and Ryoji Asahi. Improvement in thermoelectric properties of Se-Free Cu_3SbS_4 compound. *Journal of Electronic Materials*, 43(6):2356–2361, 2014.

[10] David G. Cahill, S. K. Watson, and R. O. Pohl. Lower limit to the thermal conductivity of disordered crystals. *Phys. Rev. B*, 46:6131–6140, Sep 1992.

[11] Joseph Callaway. Model for lattice thermal conductivity at low temperatures. *Phys. Rev.*, 113:1046–1051, Feb 1959.

[12] D. T. Morelli, J. P. Heremans, and G. A. Slack. Estimation of the isotope effect on the lattice thermal conductivity of group IV and group III-V semiconductors. *Phys. Rev. B*, 66:195304, Nov 2002.

[13] Tian-Ran Wei, Heng Wang, Zachary M. Gibbs, Chao-Feng Wu, G. Jeffrey Snyder, and Jing-Feng Li. Thermoelectric properties of sn-doped p-type Cu_3SbSe_4: a compound with large effective mass and small band gap. *J. Mater. Chem. A*, 2:13527–13533, 2014.

[14] Yongsheng Zhang, Eric Skoug, Jeffrey Cain, Vidvuds Ozoliņš, Donald Morelli, and C. Wolverton. First-principles description of anomalously low lattice thermal conductivity in thermoelectric Cu-Sb-Se ternary semiconductors. *Phys. Rev. B*, 85:054306, Feb 2012.

[15] Fei Zhou, Weston Nielson, Yi Xia, and Vidvuds Ozoliņš. Lattice anharmonicity and thermal conductivity from compressive sensing of first-principles calculations. *Phys. Rev. Lett.*, 113:185501, Oct 2014.

[16] J.M. Ziman. *Electrons and Phonons: The Theory of Transport Phenomena in Solids*. International series of monographs on physics. OUP Oxford, 1960.

[17] M. Omini and A. Sparavigna. *Physica B*, 212(2):101–112, 1995.

[18] M. Omini and A. Sparavigna. Beyond the isotropic-model approximation in the theory of thermal conductivity. *Phys. Rev. B*, 53:9064–9073, Apr 1996.

[19] W. Kohn and L. J. Sham. Self-consistent equations including exchange and correlation effects. *Phys. Rev.*, 140:A1133–A1138, Nov 1965.

[20] G. Kresse and J. Hafner. *Ab initio* molecular dynamics for liquid metals. *Phys. Rev. B*, 47:558–561, Jan 1993.

[21] G. Kresse and J. Hafner. *Ab initio* molecular-dynamics simulation of the liquid-metal–amorphous-semiconductor transition in germanium. *Phys. Rev. B*, 49:14251–14269, May 1994.

[22] G. Kresse and J. Furthmüller. Efficiency of ab-initio total energy calculations for metals and semiconductors using a plane-wave basis set. *Computational Materials Science*, 6(1):15 – 50, 1996.

[23] G. Kresse and J. Furthmüller. Efficient iterative schemes for *ab initio* total-energy calculations using a plane-wave basis set. *Phys. Rev. B*, 54:11169–11186, Oct 1996.

[24] P. E. Blöchl. Projector augmented-wave method. *Phys. Rev. B*, 50:17953–17979, Dec 1994.

[25] John P. Perdew, Kieron Burke, and Matthias Ernzerhof. Generalized gradient approximation made simple. *Phys. Rev. Lett.*, 77:3865–3868, Oct 1996.

[26] John P. Perdew, Kieron Burke, and Matthias Ernzerhof. Generalized gradient approximation made simple. *Phys. Rev. Lett.*, 77:3865–3868, Oct 1996.

[27] Eric J. Skoug, Jeffrey D. Cain, Paul Majsztrik, Melanie Kirkham, Edgar Lara-Curzio, and Donald T. Morelli. Doping effects on the thermoelectric properties of Cu_3SbSe_4. *Science of Advanced Materials*, 3(4):602–606, 2011-08-01T00:00:00.

[28] Yosuke Goto, Yuki Sakai, Yoichi Kamihara, and Masanori Matoba. Effect of Sn-Substitution on thermoelectric properties of copper-based sulfide, famatinite Cu_3SbS_4. *Journal of the Physical Society of Japan*, 84(4):044706, 2015.

[29] Jochen Heyd, Gustavo E. Scuseria, and Matthias Ernzerhof. Hybrid functionals based on a screened coulomb potential. *J. Chem. Phys.*, 118(18):8207–8215, 2003.

[30] Jochen Heyd and Gustavo E. Scuseria. Efficient hybrid density functional calculations in solids: Assessment of the heyd–scuseria–ernzerhof screened coulomb hybrid functional. *J. Chem. Phys.*, 121(3):1187–1192, 2004.

[31] Jochen Heyd, Gustavo E. Scuseria, and Matthias Ernzerhof. Erratum: "hybrid functionals based on a screened coulomb potential" [j. chem. phys.118, 8207 (2003)]. *The Journal of Chemical Physics*, 124(21), 2006.

[32] Dat Do, Vidvuds Ozolins, S D Mahanti, Mal-Soon Lee, Yongsheng Zhang, and C Wolverton. Physics of bandgap formation in Cu-Sb-Se based novel thermoelectrics: the role of sb valency and cu d levels. *J. Phys.: Condens. Matter*, 24(41):415502, 2012.

[33] Wu Li, Jesús Carrete, Nebil A. Katcho, and Natalio Mingo. Shengbte: A solver of the boltzmann transport equation for phonons. *Computer Physics Communications*, 185(6):1747 – 1758, 2014.

[34] J. Garin, E. Parthe, and H.R. Oswald. The crystal structure of Cu_3PSe_4 and other ternary normal tetrahedral structure compounds with composition IB_3-VA-VIA_4. *Acta Crystallographica B*, 28:3672–3674, 1972.

[35] A. Pfitzner. Crystal structure of tricopper tetraselenoantimonate (V), Cu_3SbSe_4. *Zeitschrift fuer Kristallographie*, 209:685–685, 1994.

[36] Michele D. Nielsen, Vidvuds Ozolins, and Joseph P. Heremans. Lone pair electrons minimize lattice thermal conductivity. *Energy Environ. Sci.*, 6:570–578, 2013.

[37] Wei Lai, Yuxing Wang, Donald T. Morelli, and Xu Lu. From bonding asymmetry to anharmonic rattling in $Cu_{12}Sb_4S_{13}$ tetrahedrites: When lone-pair electrons are not so lonely. *Advanced Functional Materials*, 25(24):3648–3657, 2015.

[38] Eric J. Skoug and Donald T. Morelli. Role of lone-pair electrons in producing minimum thermal conductivity in nitrogen-group chalcogenide compounds. *Phys. Rev. Lett.*, 107:235901, Nov 2011.

[39] Zhiting Tian, Jivtesh Garg, Keivan Esfarjani, Takuma Shiga, Junichiro Shiomi, and Gang Chen. Phonon conduction in PbSe, PbTe, and $PbTe_{1-x}Se_x$ from first-principles calculations. *Phys. Rev. B*, 85:184303, May 2012.

[40] B. Abeles. Lattice thermal conductivity of disordered semiconductor alloys at high temperatures. *Phys. Rev.*, 131:1906–1911, Sep 1963.

[41] Wu Li, L. Lindsay, D. A. Broido, Derek A. Stewart, and Natalio Mingo. Thermal conductivity of bulk and nanowire $Mg_2Si_xSn_{1-x}$ alloys from first principles. *Phys. Rev. B*, 86:174307, Nov 2012.

[42] Jivtesh Garg, Nicola Bonini, Boris Kozinsky, and Nicola Marzari. Role of disorder and anharmonicity in the thermal conductivity of silicon-germanium alloys: A first-principles study. *Phys. Rev. Lett.*, 106:045901, Jan 2011.

[43] A. Kundu, N. Mingo, D. A. Broido, and D. A. Stewart. Role of light and heavy embedded nanoparticles on the thermal conductivity of SiGe alloys. *Phys. Rev. B*, 84:125426, Sep 2011.

CHAPTER 4

First-Principles Study of the Impact of Guest Impurities (Na and Ba) on Lattice Thermal Conductivity of Type-I Si Clathrate

4.1 Introduction

Two effective strategies to enhance ZT are through maximization of power factor σS^2 and direct minimization of κ_l. To achieve this, an approach called "phonon-glass electron-crystal" (PGEC) was proposed by Slack [1], which states that materials with crystalline electrical conductivity and glass-like lattice thermal conductivity could have potentially high thermoelectric performance. To date, glass-like κ_l has been best realized by filling inherent voids in certain atomic structures with guest atoms. Skutterudites and clathrates are examples of such guest-host systems which contain empty cages and supporting frameworks [2, 3, 4, 5, 6]. Practically useful $ZT > 1$ has been achieved in both compounds by filling or partially filling the voids and optimizing the atomic configurations in the frameworks [7]. According to the so-called following Zintl concept, the electrical transport properties can be attributed to the framework atoms. The mechanism underneath the extremely low κ_l is still under debate [7, 8].

The strongly localized modes associated with the loosely bonded guest atoms have been used to explain the extremely low κ_l along with the resonant scattering model [9, 10]. The resonant scattering model states that the coupling between localized guest phonon modes and framework

acoustic phonon modes causes inelastic scattering, thus reducing acoustic mode lifetime. In this way, resonant scattering is introduced as an additional scattering mechanism beyond intrinsic anharmonic Umklapp processes. However, one assumption in this model, namely, that these guest atoms are uncorrelated with the framework, cannot explain their coherent coupling with acoustic modes found in the case of filled Fe_4Sb_{12}-type skutterudites [11]. On the other hand, if coherent coupling is considered, reduction in group velocity provides an reasonable explanation for the low κ_l, which in turn contradicts the resonant scattering picture [12]. In addition, supposedly, harmonic phonon modes and anharmonic phonon-phonon interactions ought to fully explain lattice dynamics. Therefore it may seem rather unphysical to introduce an extra, separate mode of scattering that is resonant scattering. Most recently, phononic filter effect has been used to interpret the abrupt spectral weight transfer from acoustic modes to guest optical modes. This has been extended to explain ultralow κ_l in intermetallic clathrates based on experimental observations of the absence of acoustic mode broadening [13, 14]. First-principles studies carried out by Li *et al*. and Terumasa *et al*. show that dramatic reduction (roughly 10-fold) in phonon mode lifetimes is responsible for ultraslow κ_l in skutterudites and type-I clathrates, respectively[15, 16]. One issue is that, there are many potential guest atoms for all framework materials. It is not fully studied which guest atoms in a given framework lead to which type of coupling, coherent or incoherent. Another issue is to firmly establish the importance of reduction in group velocity as well as lifetime.

In this chapter, we do not consider other variables such as partial filling, disorder or off-center rattling atoms in order to estimate the fundamental impacts of guest atoms on κ_l. In light of these acknowledgments, we decide to choose type-I Si clathrates, namely Si_{46}, and it fully filled with Na and Ba, to investigate the impact of guest atoms on phonon dispersion, mode lifetime, group velocity and κ_l. In the following sections, we start with the analysis of CSLD fitted IFCs and then explain coherent and incoherent couplings between guest and host atoms with calculated

phonon dispersions and density of states. Afterwards, calculated κ_l is compared to and validated with experimental measurements. To explain the dramatic reduction of κ_l due to guest atoms, we analyze phonon mode group velocity and lifetime in these three compounds. In addition, scattering rates due to phonon absorption and emission are discussed in detail. Contributions to total lattice thermal conductivity from different phonon modes are further explained. Finally, we summarize our findings by establishing the importance of reduction in both group velocity and lifetime.

4.2 Computational Details

4.2.1 DFT Calculations

Vienna *Ab initio* simulation package (VASP) was used to perform both structural relaxation and self-consistent calculations [17, 18, 19, 20]. The projector-augmented wave (PAW) [21] method utilizing the Perdew-Becke-Ernzerhof (PBE) [22] generalized gradient approximation (GGA) [23] was used for the exchange-correlation (xc) functional [24]. For the structural relaxation a Monkhorst-Pack $4\times4\times4$ **k**-point mesh and a plane wave basis with cutoff energy of 600 eV were used. The force and energy convergence thresholds were set to 10^{-3} eV Å^{-1} and 10^{-7} eV per primitive cell, respectively. Self-consistent calculations were performed on fifteen $2\times2\times2$ supercell structures with randomly perturbed atomic positions from 0.01 Å to 0.05 Å with the same convergence settings. IFCs were fitted from these structures using CSLD.

4.2.2 Fitting IFCs

We included up to 13 ($\sim$10 Å cutoff) and 3 ($\sim$4 Å cutoff) neighbor shells for second- and third-order interactions respectively. This yields 1,083, 1,706 and 1778 symmetrically distinct IFC elements. The optimal parameters used in the convex optimization within CSLD [25] were se-

lected from a set of values based on random sub-sampling validation, in which randomly selected $\approx$70% of forces were used for training and the rest for validation. Afterwards, multiple independent fittings of IFCs were carried out using optimized parameters and training set of randomly selected $\approx$90% of forces. Fig. 4.1 shows the comparison between our predicted forces and those directly calculated by VASP. Small relative errors verify the utilized cutoffs for second- and third-order interactions and indicate the good accuracy of fitted IFCs as well. Fig. 4.2 shows the Frobenius norm of the calculated second- and third-order IFCs with increasing interaction distances. Second-order IFCs are already very small for interaction distances larger than 6 Å. Most third-order IFCs are restricted within 4 Å. Comparison between second- and third-order one-body interactions are shown in Fig. 4.3 and Fig. 4.4. Fitted second-order IFCs were further verified and compared with those calculated using density functional perturbation theory (DFPT) [26, 27, 28] implemented in VASP. Constructed $2 \times 2 \times 2$ supercells were used in DFPT calculation with the same convergence settings. Dispersions obtained from CSLD are in excellent agreement with those obtained from DFPT. To calculate κ_l, a various sizes of phonon wavevector $\mathbf{q}$-meshes were used to check the convergence with respect to Brillouin zone sampling. It was found that within our available computational resource a mesh size of $9\times9\times9$ and $scalebroad = 0.1$ lead to relatively good convergence [29]. Fig. 4.8 shows the calculated κ_l at 300 K for Si_{46}, Na_8Si_{46} and Ba_8Si_{46} using IFCs obtained from 5 independent fittings. The averaged values are 42.3, 2.2 and 1.3 W m^{-1} K^{-1} respectively. The standard deviations are 0.03, 0.06 and 0.02 W m^{-1} K^{-1} respectively.

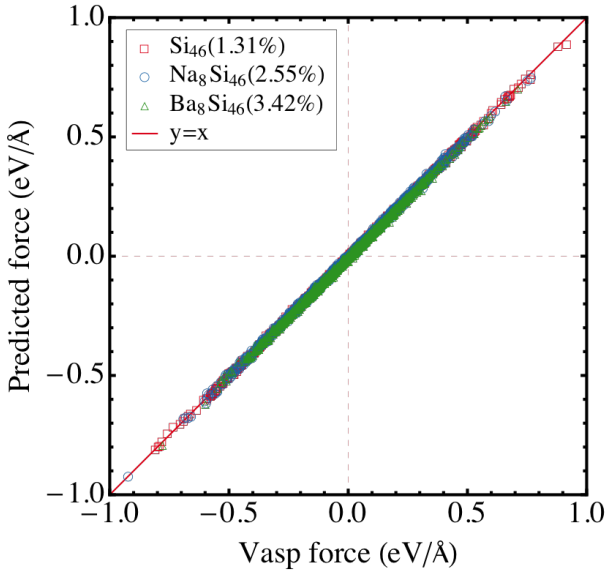

Figure 4.1: Comparison between forces predicted by fitted IFCs and those directly from VASP calculation. The red solid line is a diagonal representing exact fit. Relative error for predicted forces is indicated in the legends.

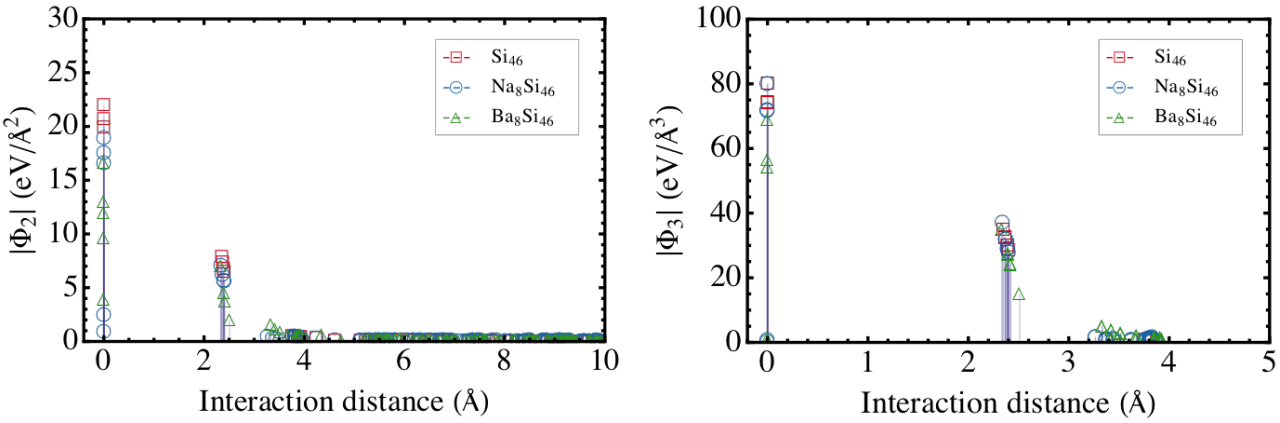

Figure 4.2: Frobenius norm of calculated second- and third-order IFCs versus interaction distance defined as the maximum distance between atoms.

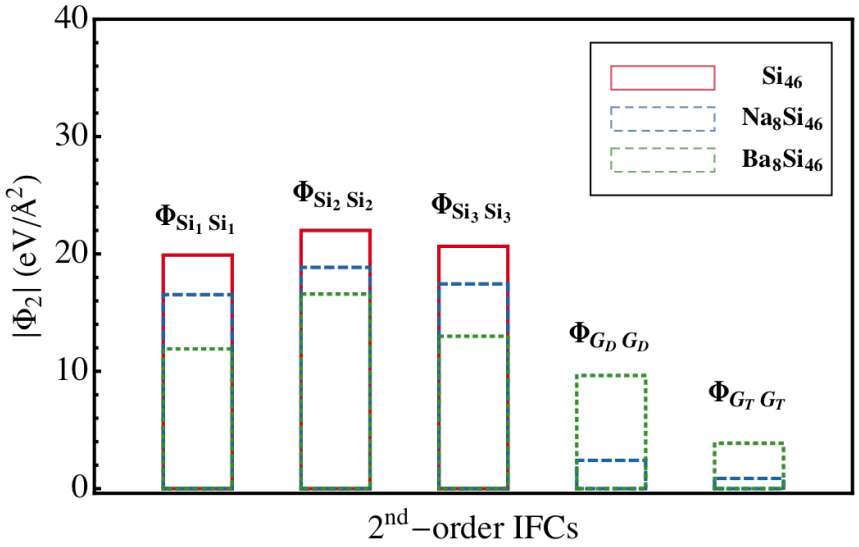

Figure 4.3: Comparison of second–order IFCs for one-body interactions between Si_{46}, Na_8Si_{46} and Ba_8Si_{46}.

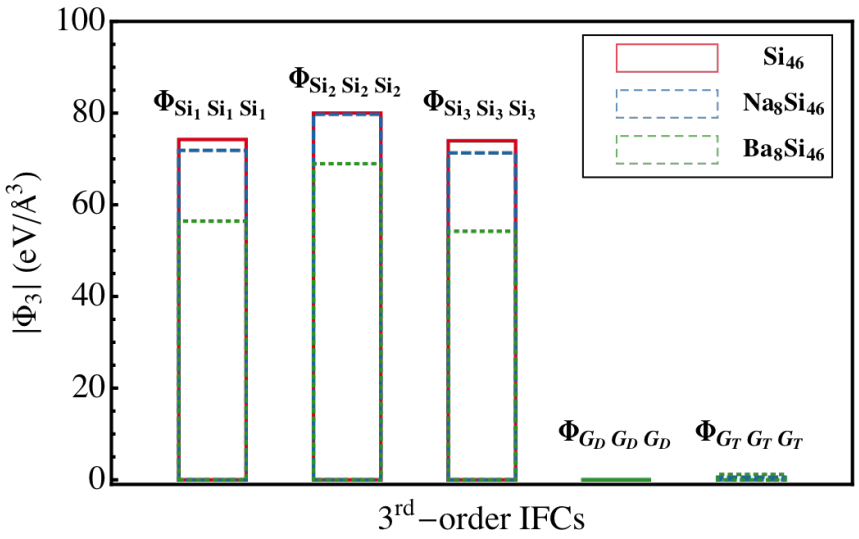

Figure 4.4: Comparison of third-order IFCs for one-body interactions between Si_{46}, Na_8Si_{46} and Ba_8Si_{46}.

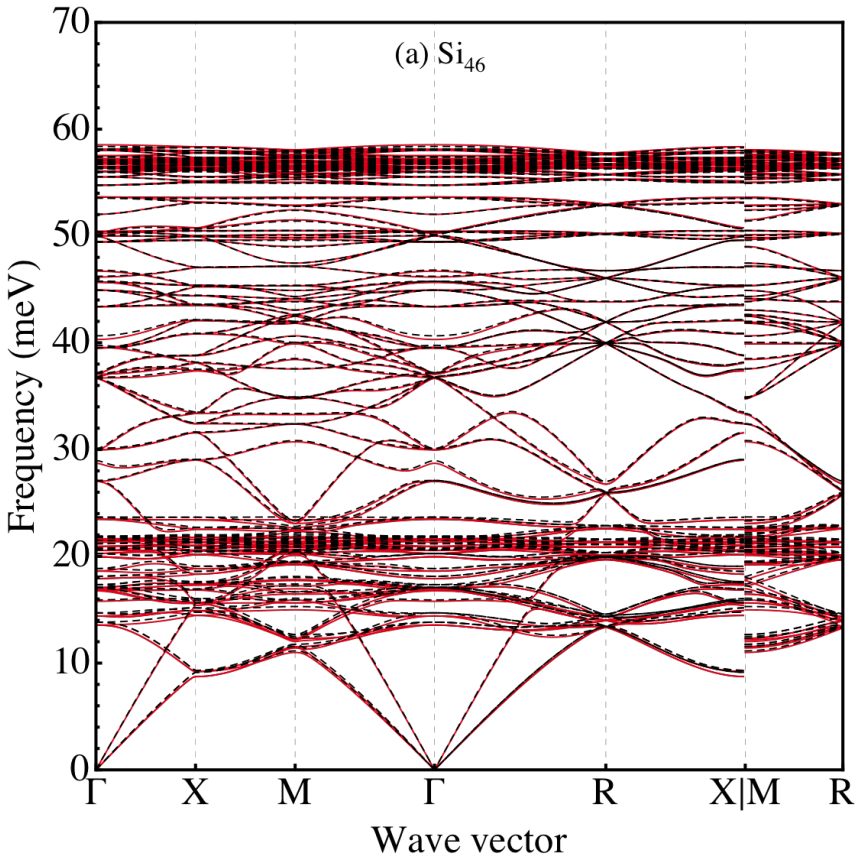

Figure 4.5: Comparison of phonon dispersions calculated by CSLD (red solid line) and DFPT (black dashed line) for Si_{46}

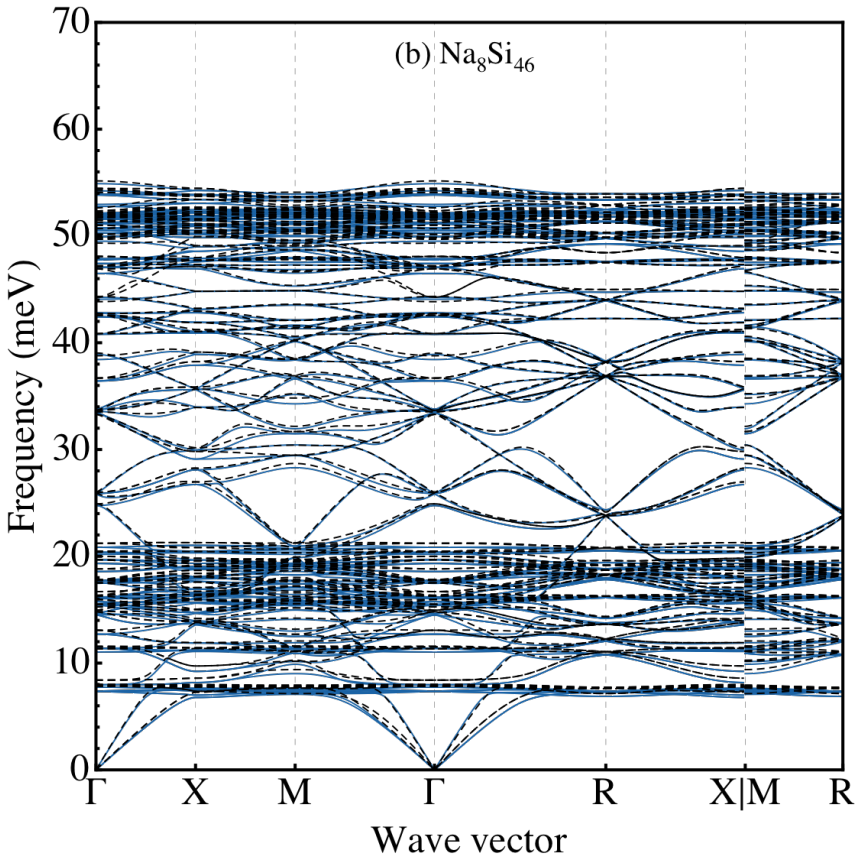

Figure 4.6: Comparison of phonon dispersions calculated by CSLD (blue solid line) and DFPT (black dashed line) for Na_8Si_{46}

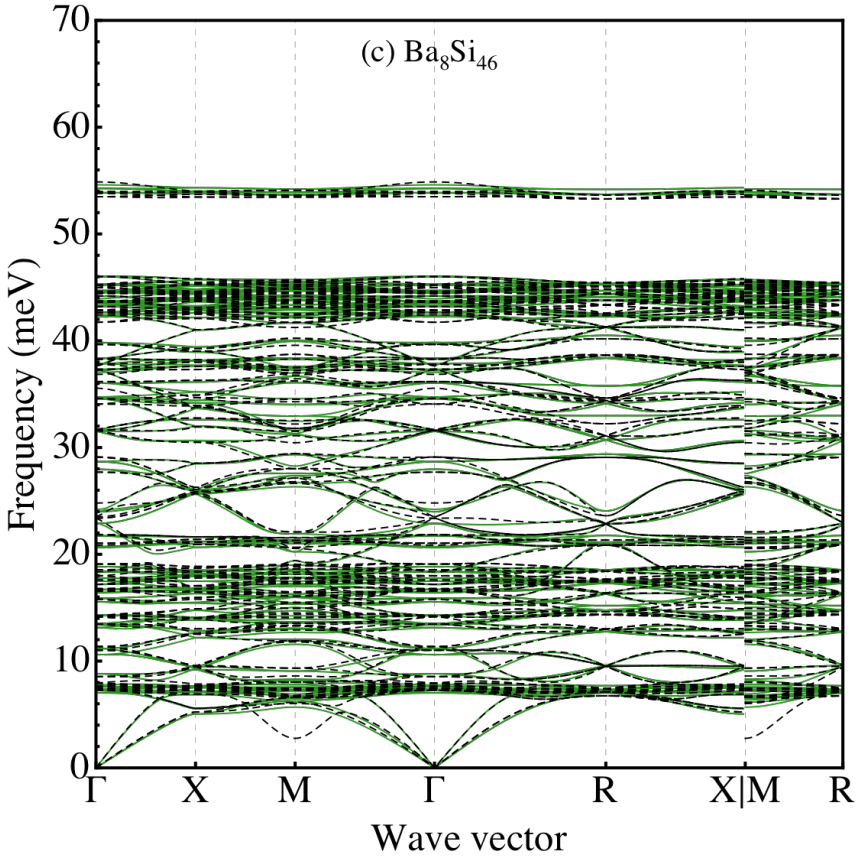

Figure 4.7: Comparison of phonon dispersions calculated by CSLD (green solid line) and DFPT (black dashed line) for Ba_8Si_{46}

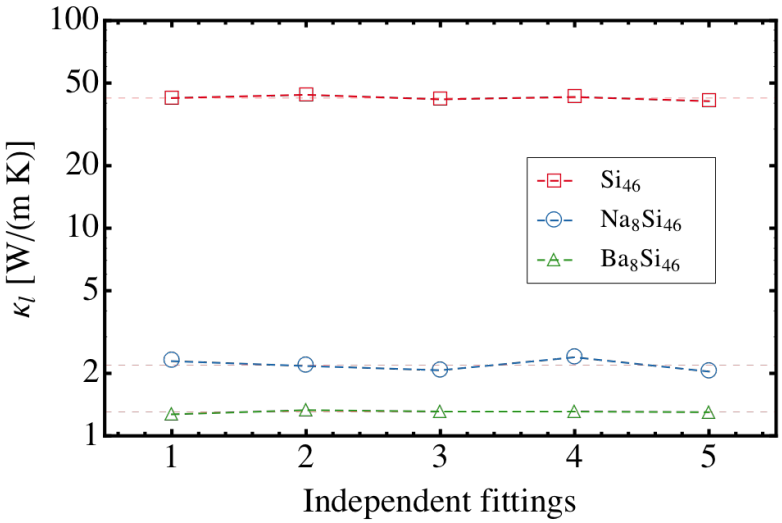

Figure 4.8: Calculated lattice thermal conductivities for Si_{46} (red square), Na_8Si_{46} (blue circle) and Ba_8Si_{46} (green triangle) from 5 independent fittings. The thin red dashed lines denote the corresponding averaged lattice thermal conductivities.

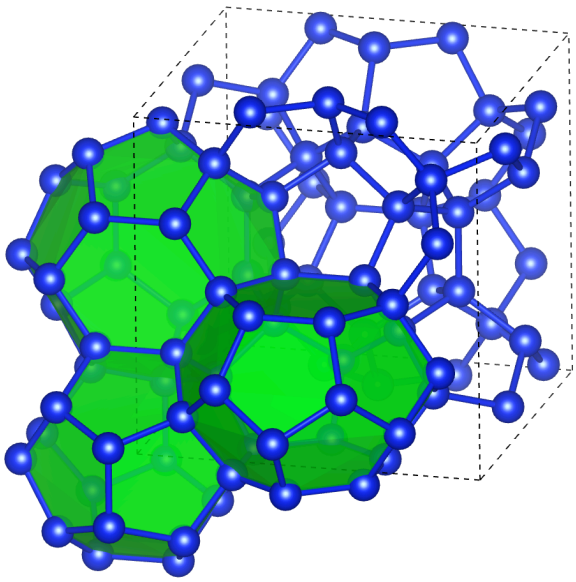

Figure 4.9: Crystal structure of type-I Si clathrate without guest atoms. Si atoms are denoted as blue solid spheres. There are two kinds of polyhedra: dodecahedral and tetrakaidecahedral.

4.3 Results and Discussion

4.3.1 Crystal Structure

Fig. 4.9 shows the crystal structure for the type-I Si clathrate. It belongs to the space group $Pm\bar{3}n$ and contains 46 Si atoms in the primitive cell. The framework atom Si occupies three crystallographic sites 6*c*, 16*i* and 24*k* [7]. There are two types of sites that can be occupied by total eight guest atoms in the primitive cell: the 2*a* site in small dodecahedron (D) and 6*d* site in large tetrakaidecahedron (T) [7]. Compared with other type-I clathrate compounds such as $Ba_8Ga_{16}Sn_{30}$ and $Eu_8Ga_{16}Ge_{30}$, the type-I Si clathrate has a smaller cage volume and contains no disorder in the framework, which can supress the off-center occupation of guest atoms, making it an ideal platform for examining the impact of solely guest atoms on κ_l[7, 30]. Our fully relaxed lattice constants for Si_{46}, Na_8Si_{46} and Ba_8Si_{46} are 10.229, 10.243 and 10.396 Å respectively. Compared with experimentally measured values of 10.250, 10.196 and 10.328 Å [31, 32, 33], the relative errors are all within 1%. The lattice parameter of Si_{46} is slightly un-

derestimated while those of Na and Ba doped Si clathrates are overestimated. This is probably due to the different smearing schemes adopted for semiconductor and metal. Doping with Ba expands the lattice by 1.6% while doing with Na merely expands it by 0.13%.

4.3.2 IFCs and Phonon Dispersion

The analysis of the fitted IFCs in Fig. 4.2 shows that the second- and third-order one-body interactions in all three compounds are associated with the three Si sites (denoted as Si_1, Si_2 and Si_3) and the two guest atom sites. Second- and third-order IFCs with non-zero interaction distances and large Frobenius norms are all associated with the nearest-neighbor Si-Si interactions. Noticeable differences in one-body interactions among Si_{46}, Na_8Si_{46} and Ba_8Si_{46} are found and analyzed in Fig. 4.3 and Fig. 4.4. For the second–order one-body interactions, several features can be inferred: (1) the addition of guest atoms weakens the one-body interactions of Si atoms; (2) the one-body interactions of guest atoms are generally weaker than those of Si atoms in the framework; (3) the one-body interactions of Ba atoms are considerably stronger than those of Na atoms; (4) the one-body interactions of guest atoms in dodecahedral cages are stronger than those in tetrakaidecahedral cages. For the third-order one-body interactions, similar features as in second–order one-body interactions can be found. In addition, Na atoms have much less impact on the strength of the third-order one-body Si-Si interactions, leaving them nearly unchanged. Another interesting feature is that the third-order one-body interactions of guest atoms in tetrakaidecahedral cages are very small and those in dodecahedral cages are exactly zero as enforced by symmetry. For the second- and third-order nearest-neighbor Si-Si interactions, the addition of Na has a weak influence while that of Ba reduces the interaction strength considerably. The above analysis provides a unified picture that Na atoms interact weakly with the framework and act more like an individually rattling atoms (incoherent coupling), while Ba atoms interact strongly with the framework (coherent coupling).

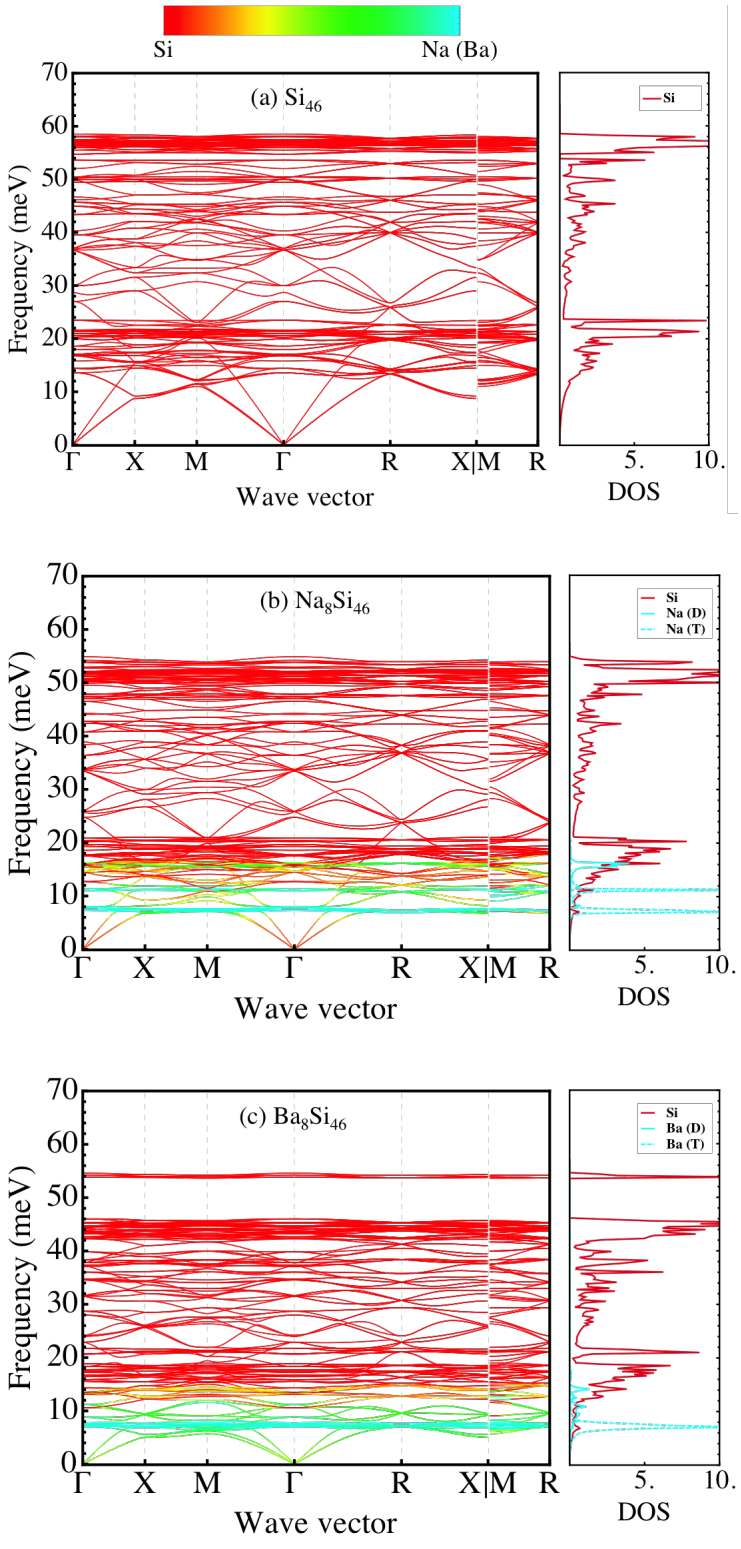

Figure 4.10: Calculated phonon dispersions and atom-projected phonon density of states for Si_{46}, Na_8Si_{46} and Ba_8Si_{46} respectively. Interpolated colors are assigned to phonon modes according to the Frobenius norm of the normalized polarization vector of Na (Ba) atoms. Red is used for value of 0 (pure Si) and light blue for 1 (pure Na or Ba).

Fitted harmonic IFCs were used to calculate phonon dispersions and atom-projected phonon density of states (DOS) shown in Fig. 4.10. The addition of guest atoms in the empty cages slightly suppresses the Debye temperatures via weakening of the second-order interactions. Profound changes of vibrational spectrum are found in the low-frequency window from 0 to 20 meV. In contrast to Si_{46}, three frequency peaks resembling the single-frequency Einstein mode associated with Na atoms are identified and centered at energies $E_1 \approx$ 6-8 meV, $E_2 \approx$ 10-12 meV and $E_3 \approx$ 14-16 meV. The lowest-energy optical modes associated with the Na atoms are rather flat, cutting through the acoustic branches, confirming the "avoided crossing" behavior. The resulting strongly localized modes can be attributed to the weak interaction (small absolute values of IFCs) between guest (Na) and host (Si) atoms as demonstrated in Ref. [8]. The small expansion of lattice parameter in Na_8Si_{46} compared with Si_{46} also provides evidence for the uncorrelated vibrations of Na atoms. It is further found that the two phonon DOS peaks at lower frequencies are associated with the Na atoms occupying the 6*d* sites in tetrakaidecahedral cages, and the highest-frequency peak corresponds to Na vibrations at the 2*a* sites in dodecahedral cages. In contrast, vibrations of guest atoms in Ba_8Si_{46} cannot be classified into various narrow frequency windows. Instead, the corresponding phonon DOS exhibits an delocalized distribution. This is in line with the coherent coupling of the guest atoms with the host lattice found in experiments [12, 14]. Only one broadened frequency peak resembling the single-frequency Einstein mode is found at energy $E_1' \approx$ 6-8 meV, which corresponds to the vibrations of Ba atoms in tetrakaidecahedral cages. Meanwhile, the vibrations of Ba atoms with delocalized frequencies are located in dodecahedral cages. In addition, the strong interaction between Ba and Si atoms further eliminates the anisotropy of tetrakaidecahedral cage found between Na and Si atoms, making the two low-frequency peaks merge into one. The striking difference in vibrational dynamics between Na and Ba probably can be to attributed to their different atomic sizes.

4.3.3 Lattice Thermal Conductivity

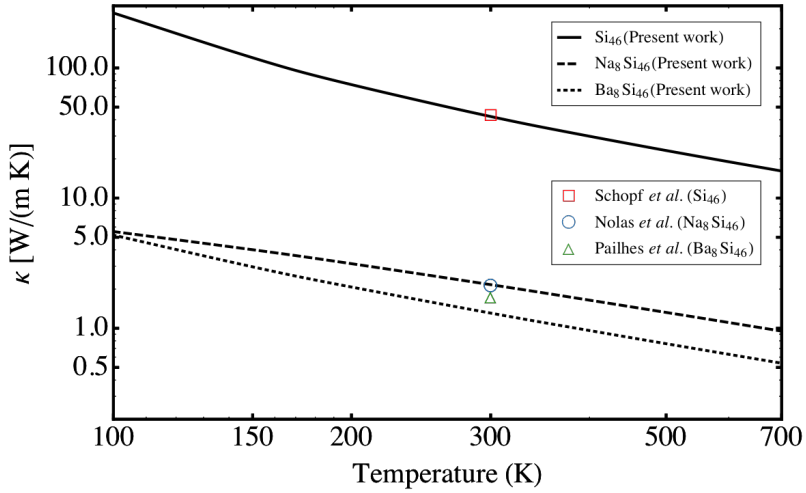

Figure 4.11: Calculated lattice thermal conductivities for Si_{46} (solid line), Na_8Si_{46} (dashed line) and Ba_8Si_{46} (dotted line) respectively. The red square denotes the simulated value for Si_{46} at 300 K using effective potential [34]. Blue circle and green triangle are experimental measurements for Na_8Si_{46} and Ba_8Si_{46} from Pailhès *et al.* [14] and Nolas *et al.* [35]

Fig. 4.11 shows the calculated κ_l for Si_{46}, Na_8Si_{46} and Ba_8Si_{46} compared with previous studies. κ_l of Si_{46} is significantly higher than those of Na_8Si_{46} and Ba_8Si_{46} at temperatures from 100 to 700 K. The κ_l of Na_8Si_{46} are roughly two times that of Ba_8Si_{46}. Due to the limited available experimental measurements we are only able to compare them with our theoretical predictions at room temperature (300 K). Empirical potentials have been generated to simulate κ_l for the type-I semiconductor clathrate systems. Daniel *et al*. predicted that κ_l of Si_{46} and Ba_8Si_{46} are 43.1 ± 4.1 and 6.0 ± 0.3 W m^{-1} K^{-1} at 300 K [34]. They attribute the overestimation of κ_l of Ba_8Si_{46} compared with experimental value of 1.7 W m^{-1} K^{-1} to the difference in the lattice constants between simulation and experiment [14]. Our calculated κ_l of 1.3 W m^{-1} K^{-1} for Ba_8Si_{46} is in a better agreement with experiments, and κ_l of 42.3 W m^{-1} K^{-1} for Si_{46} is in line with their simulation [34]. Our calculated κ_l of 2.2 W m^{-1} K^{-1} for Na_8Si_{46} is also in a good agreement with the estimation of 2.1 W m^{-1} K^{-1} by Nolas *et al* [35]. Their underestimation

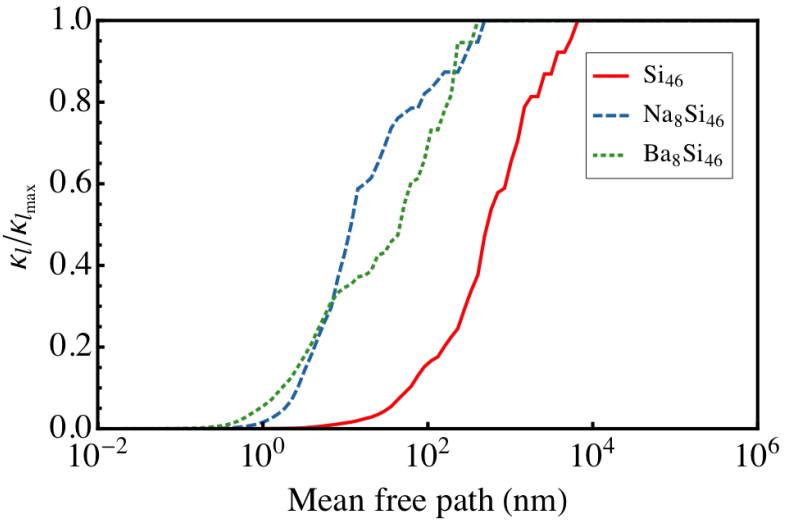

Figure 4.12: Calculated cumulative lattice thermal conductivities for Si_{46} (red solid line),Na_8Si_{46} (green dashed line) and Ba_8Si_{46} (green dotted line) with respect to maximum mean free path at 300 K

is probably due to the usage of rather short mean free path of 5.1 Å which is the distance between Na atoms inside tetrakaidekahedral cages. It is believed that the κ_l obtained by first-order perturbation theory is generally overestimated due to the neglection of high-order interactions. However, the calculated mean free paths from perturbation theory could drop below the smallest interatomic distances, underestimating κ_l. Relatively sparse $\mathbf{q}$-point mesh and small value of *scalebroad* adopted in the calculation could also underestimate of κ_l. In addition, the accuracies of experimentally extracted κ_l values of Na_8Si_{46} and Ba_8Si_{46} depend on the validity of the constant Lorenz number used in the Wiedemann-Franz law. Therefore more experimental measurements with high accuracy are required for a comprehensive comparison and analysis.

The dependence of κ_l on MFP is examined by the calculated cumulative κ_l in Fig. 4.12. Si_{46} has a large MFP range from 1 to 10^4 nm, while for Na_8Si_{46} and Ba_8Si_{46} MFP has a small range from 0.1 to 500 nm. It is found that phonon modes with MFPs larger than 1.0 nm contribute over 90% of the total κ_l. This directly rebuts the regularly used assumption that MFP in these compounds are limited by the physical separation of the guest atoms [12]. Thus the contradiction between

rather short estimated phonon mode lifetime (below 0.2 ps) from these MFPs and experimentally measured much longer lifetime (above 1.0 ps) probably cannot be used to rule out the extra scattering induced by guest atoms, which is in contrast to the conclusion in Ref. [12].

4.3.4 Group Velocity and Lifetime

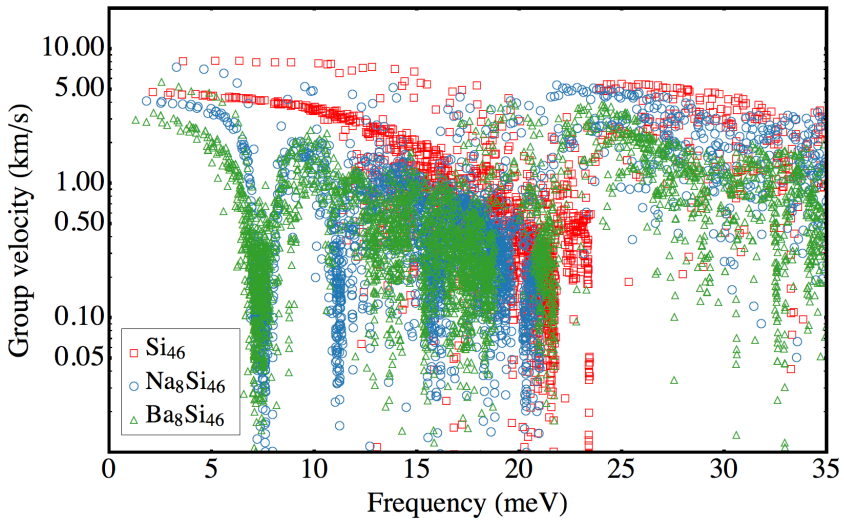

Figure 4.13: Calculated phonon group velocities for Si_{46} (red square), Na_8Si_{46} (blue circle) and Ba_8Si_{46} (green triangle) respectively.

Since phonon mode group velocity and lifetime are two main factors that determine κ_l, we examine the impact of guest atoms on these quantities. The phonon mode group velocities with frequencies less than 35 meV are plotted in Fig. 4.13. Generally, group velocities of Si_{46} are larger than those of Na_8Si_{46} and Ba_8Si_{46} because of the steep acoustic dispersion extending up to about 15 meV. In the acoustic region (below 6 meV) Na_8Si_{46} has similar but slightly reduced group velocities compared to Si_{46}, while Ba_8Si_{46} has significantly reduced group velocities due to both heavy atomic mass and weakened interatomic interactions. Group velocities of both Na_8Si_{46} and Ba_8Si_{46} are dramatically reduced in the frequency window from 6 to 8 meV due to the presence of localized optical modes associated with guest atoms. The extra rattling modes centered at about 12 meV in Na_8Si_{46} further reduce the corresponding mode group velocity.

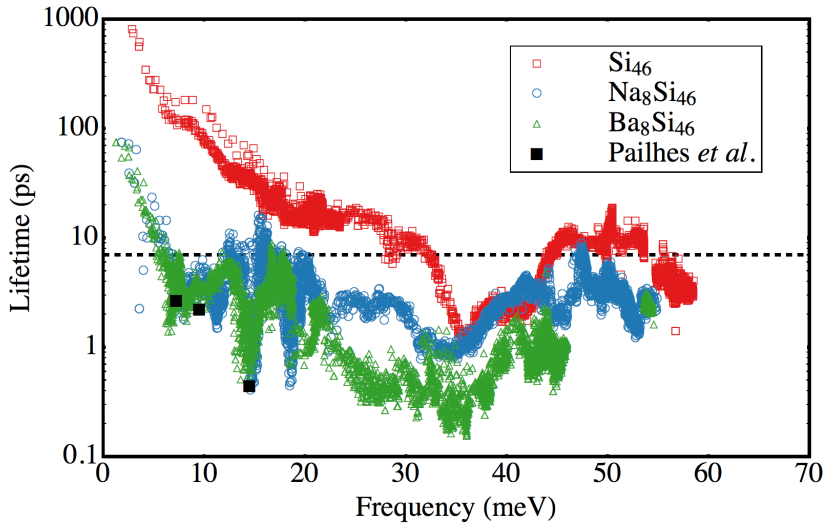

Figure 4.14: Calculated phonon mode lifetime for Si_{46} (red square), Na_8Si_{46} (blue circle) and Ba_8Si_{46} (green triangle) at 300 K. Three solid black squares are three measured lifetimes of longitudinal phonon modes centered at frequencies $E_1' \sim$ 6-8 meV, $E_2' \sim$ 8-10 meV and $E_3' \sim$ 14-16 meV [14]. The black dashed line indicate the experimental resolution limit of about 7 ps [14].

Frequency-dependent phonon lifetime is plotted in Fig. 4.14. Roughly 10-fold reduction of mode lifetimes is observed in both Na_8Si_{46} and Ba_8Si_{46} from those in Si_{46}. Considering the energy widths of acoustic modes are beyond the experimental resolution limit of 0.2 meV , we are only able to compare the lifetimes of three optical modes of Ba_8Si_{46} to experimental measurements, which are centered at frequencies $E_1' \approx$ 6-8 meV, $E_2' \approx$ 8-10 meV and $E_3' \approx$ 14-16 meV. The experimentally measured energy widths of 0.5, 0.6 and 3 meV for longitudinal phonons ($\mathbf{q}_{00h}$) in these three frequency windows, corresponding to mode lifetimes of 2.6, 2.2 and 0.22 ps, are in good agreements with our calculation as show in Fig. 4.14 [14]. The calculated energy widths of acoustic modes for Ba_8Si_{46} are all below the resolution limit of 0.2 meV (6.6 ps), which validates the absence of a broadening of the acoustic modes in experimental data [14]. Therefore it is improper to exclude the usual scattering mechanism as a main cause of the reduced κ_l since in both empty and filled Si clathrates the energy widths of acoustic modes are beyond the resolution limit, which in turn invalidates phononic filter effect [13, 14].

4.3.5 Scattering Rates

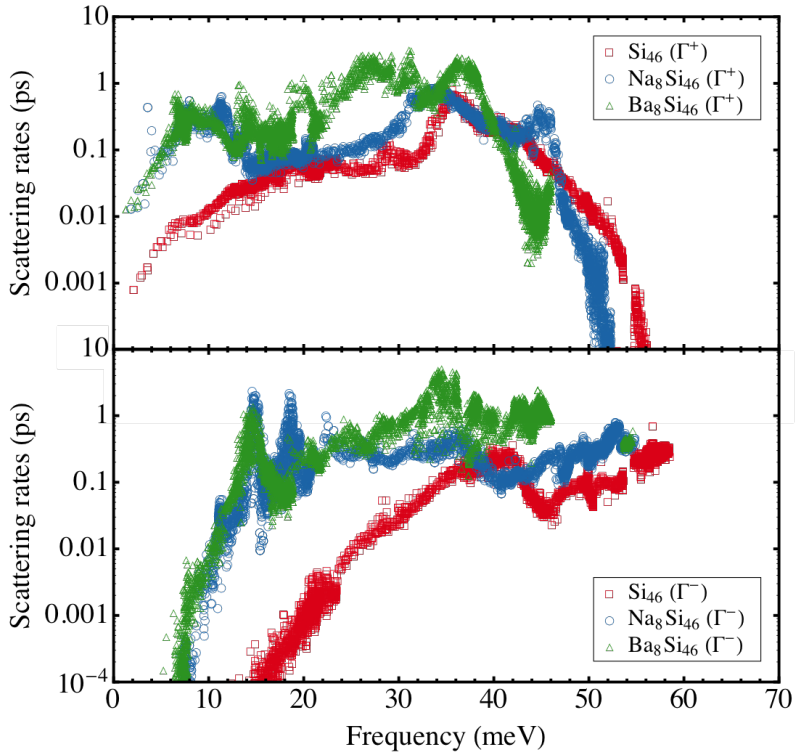

Figure 4.15: Calculated scattering rates of absorption (Γ^+) and emission (Γ^-) processes for Si_{46} (red square), Na_8Si_{46} (blue circle) and Ba_8Si_{46} (green triangle) at 300 K.

Though the calculated phonon mode lifetimes explicitly exhibit a roughly 10-fold reduction in compounds of Na_8Si_{46} and Ba_8Si_{46} as in Ref. [15, 16], it is more instructive to examine the scattering rates for absorption and emission processes. It is found that scattering rates due to both absorption and emission of phonon modes with frequencies less than 40 meV are greatly enhanced in Na_8Si_{46} and Ba_8Si_{46}. Moreover, phonon modes with frequencies less than about 12 meV are mostly scattered by combining with other phonon modes in the absorption process. Since phonon modes with frequencies beyond the rattling frequencies ($\omega < 6$ meV and $\omega >$ 20 meV) are heavily scattered, it is thus inferred that the presence of guest atoms drastically change the scattering mechanism and induce extra scattering channels.

To identify the details of phonon modes involved in the scattering processes, we examine the

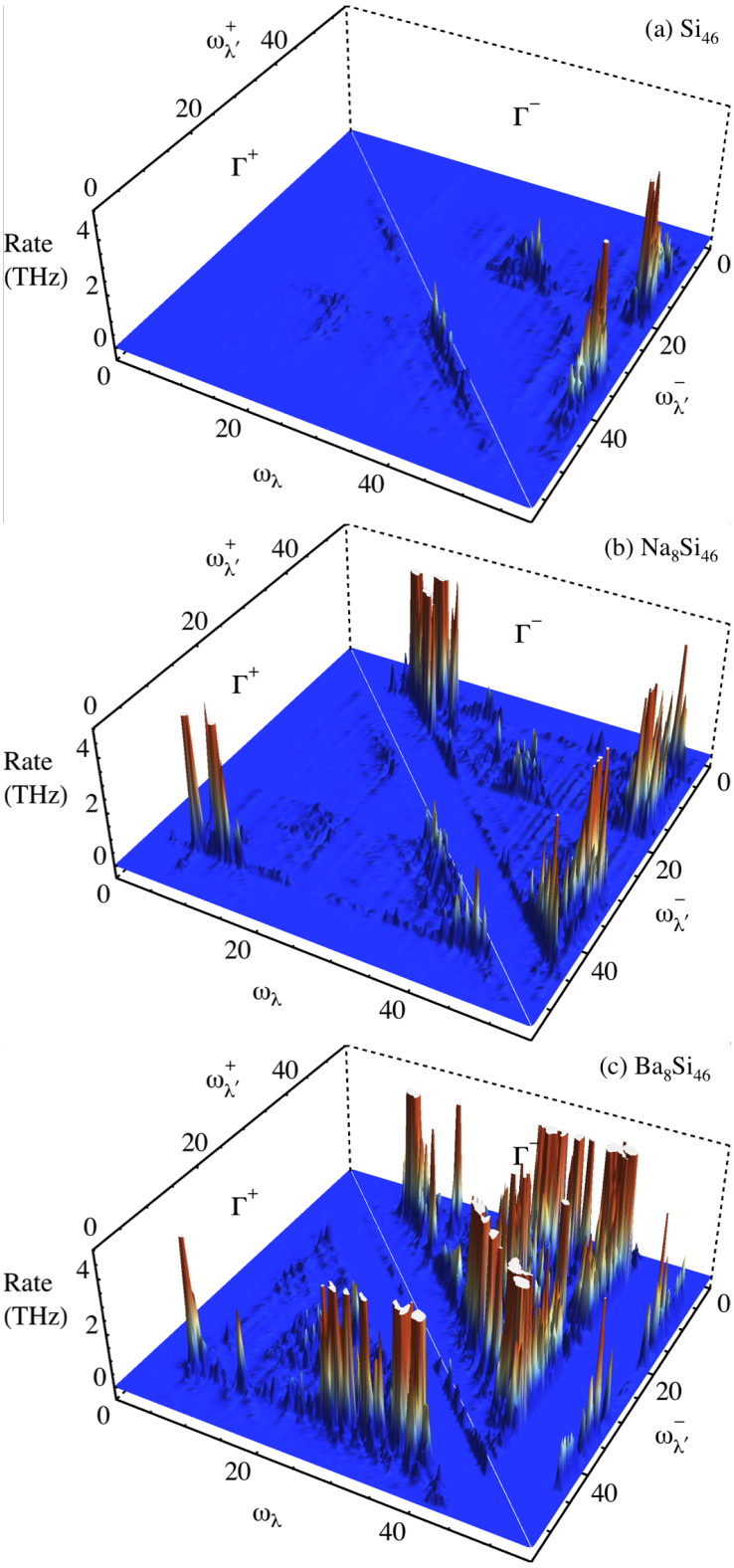

Figure 4.16: Scattering rates associated with phonon mode (λ) in the absorption (Γ^{+}: $\lambda + \lambda^{'} \rightarrow \lambda^{''}$) and emission ($\Gamma^{-}$: $\lambda \rightarrow \lambda^{'} + \lambda^{''}$) processes for Si_{46}, Na_8Si_{46} and Ba_8Si_{46} at 300 K. The corresponding phonon frequencies are given in meV.

scattering events in Fig. 4.16. The energy conservation constraint restricts the absorption and emission processes in the lower and upper triangular panels. Considering the absorption processes, Fig. 4.16 (b) explicitly shows the additional three strong scattering peaks with $\omega_\lambda <$ 20 meV, which correspond to absorptions involving ($\omega_\lambda \approx E_1$, $\omega_{\lambda'} \approx E_1$), ($\omega_\lambda \approx E_1$, $\omega_{\lambda'} \approx E_2$) and ($\omega_\lambda \approx E_2$, $\omega_{\lambda'} \approx E_1$) for Na_8Si_{46} compared with Si_{46}. Moreover, rattling modes with $\omega_{\lambda'} \approx E_1$ can be further absorbed by high-frequency optical modes with $\omega_\lambda > 40$ meV. Similarly, rattling modes with $\omega_{\lambda'} \approx E_1'$ gives rise to strong additional scattering of phonon modes with $\omega_\lambda \approx E_1'$, 12-14 and 25-40 meV for Ba_8Si_{46} in Fig. 4.16 (c). Considering the emission processes, the scattering peaks in Na_8Si_{46} are found mostly due to emission of rattling modes with $\omega_{\lambda'} \approx E_1$ and E_2, while in Ba_8Si_{46} there are considerable scattering rates due to non-rattling modes. Therefore two points can be inferred: (1) rattling modes due to vibrations of guest atoms in tetrakaidecahedral cages can be effectively either absorbed or emitted, thus dramatically increasing scattering rates; (2) the change of vibrational spectrum due to the presence of guest atoms can induce extra scattering events in addition to those directly caused by rattling modes.

4.3.6 Differential Lattice Thermal Conductivity

From the above analysis of group velocity and lifetime, we can safely draw a conclusion that it is the rattling modes which heavily reduce group velocity and enhance scattering rates that lead to the dramatic reduction of κ_l in Na_8Si_{46} and Ba_8Si_{46}. However, it is not easy to decouple the impact of group velocity from that of phonon lifetime. Previous experimental and theoretical investigations tend to achieve different conclusions on the importance of reducing group velocity [15, 16, 12, 14]. Observing the fact that the phonon mode lifetimes of Si_{46} has a strong dependence on frequency while depends weakly on phonon wavevector, we calculated κ_l for Na_8Si_{46} and Ba_8Si_{46} using frequency-dependent phonon lifetimes of Si_{46}, which are denoted as $Na_8Si_{46}^*$ and $Ba_8Si_{46}^*$, and can be used to estimate the reduction of κ_l purely due to reduc-

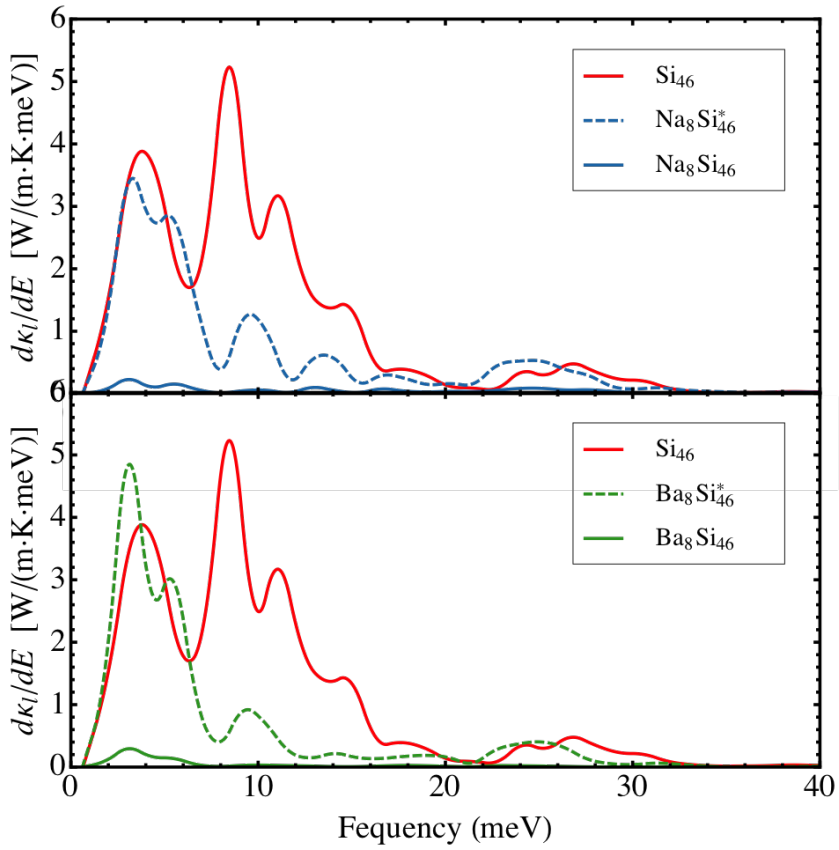

Figure 4.17: Calculated differential lattice thermal conductivity with respect to frequency for Si_{46} (red solid line), Na_8Si_{46} (blue solid line) and Ba_8Si_{46} (green solid line) at 300 K. The dashed lines denote the results obtained with frequency-dependent phonon mode lifetime of Si_{46}.

tion of group velocity. Since acoustic, optical and rattling modes can be classified into different frequency windows, we estimate their contributions to κ_l by plotting the differential κ_l with respect to frequency in Fig. 4.17. We find phonon modes with frequencies higher than 40 meV hardly contribute to the total κ_l. We further divide the frequency window from 0 to 40 meV into three subregions, namely, (I) 0-6 meV, (II) 6-20 meV and (III) 20-40 meV. Therefore we can clarify heat conduction from different phonon modes, namely acoustic modes below the localized guest modes (I), low-energy optical modes with (II) and without (III) localized modes. The Si_{46}, $Na_8Si^*_{46}$ and $Ba_8Si^*_{46}$ have comparable large contributions to total κ_l in regions of both (I) and (III), where κ_l is dramatically reduced in both Na_8Si_{46} and Ba_8Si_{46}. This indicates that the reduction of lifetime dominates over that of group velocity. The higher contribution to total κ_l from $Ba_8Si^*_{46}$ in (I) region is due to the higher density of states towards the flat localized modes. In contrast, contributions to the total κ_l from $Na_8Si^*_{46}$ and $Ba_8Si^*_{46}$ are much less than that of Si_{46} in region (II), from which we believe the reduction in group velocities are also very important. In conclusion, it is crucial to have both significantly reduced phonon lifetime and suppressed group velocity to achieve the overall low κ_l.

4.4 Conclusions

In summary, we identified the coherent and incoherent couplings between the guest optical modes and framework acoustic modes in Na and Ba filled type-I Si clathrates. The coherence is possibly related to the atomic sizes of guest atoms and the resulting lattice expansion. We further confirm the "avoided crossing" behavior as well. Small cations (Na) tend to form separated localized modes in both dodecahedral and tetrakaidecahedral cages, while large cations (Ba) form localized modes in tetrakaidecahedral cage and coherently coupled with the framework in dodecahedral cages. The low lattice thermal conductivities of Na_8Si_{46} or Ba_8Si_{46} should be attributed

to the dramatic reduction in both phonon lifetime and group velocity. Specifically, the localized guest modes not only gives rise to small group velocities but also can be either absorbed or emitted in the scattering events, thus dramatically enhancing scattering rates. The increased intrinsic anharmonicity with additional guest atoms are responsible for the observed low lattice thermal conductivities, thus ruling out both resonant scattering mechanism and phononic filter effect.

4.5 Acknowledgement

This work was supported by the Office of Naval Research (Grant No. N00014-14-1-0444) and used computing resources at the National Energy Research Scientific Computing Center (NERSC), which is supported by the US DOE under contract DE-AC02-05CH11231. The work by Fei Zhou was performed under the auspices of the US DOE by Lawrence Livermore National Laboratory under contract DE-AC52-07NA27344.

References

[1] G. A. Slack. *CRC Handbook of Thermoelectrics*. CRC Press, Boca Raton, FL, 1995.

[2] G. S. Nolas, G. A. Slack, D. T. Morelli, T. M. Tritt, and A. C. Ehrlich. The effect of rare earth filling on the lattice thermal conductivity of skutterudites. *J. Appl. Phys.*, 79(8):4002–4008, 1996.

[3] B. C. Sales, D. Mandrus, and R. K. Williams. Filled skutterudite antimonides: A new class of thermoelectric materials. *Science*, 272(5266):1325–1328, 1996.

[4] Donald T. Morelli, Gregory P. Meisner, Baoxing Chen, Siqing Hu, and Ctirad Uher. Cerium filling and doping of cobalt triantimonide. *Phys. Rev. B*, 56:7376–7383, Sep 1997.

[5] G. S. Nolas, J. L. Cohn, G. A. Slack, and S. B. Schujman. Semiconducting Ge clathrates: Promising candidates for thermoelectric applications. *Applied Physics Letters*, 73(2):178–180, 1998.

[6] B. C. Sales, D. Mandrus, B. C. Chakoumakos, V. Keppens, and J. R. Thompson. Filled skutterudite antimonides: electron crystals and phonon glasses. *Phys. Rev. B*, 56:15081–15089, Dec 1997.

[7] Toshiro Takabatake, Koichiro Suekuni, Tsuneyoshi Nakayama, and Eiji Kaneshita. Phonon-glass electron-crystal thermoelectric clathrates: Experiments and theory. *Rev. Mod. Phys.*, 86:669–716, Jun 2014.

[8] Eric S. Toberer, Alex Zevalkink, and G. Jeffrey Snyder. Phonon engineering through crystal chemistry. *J. Mater. Chem.*, 21:15843–15852, 2011.

[9] R. O. Pohl. Thermal conductivity and phonon resonance scattering. *Phys. Rev. Lett.*, 8:481–483, Jun 1962.

[10] J. L. Cohn, G. S. Nolas, V. Fessatidis, T. H. Metcalf, and G. A. Slack. Glasslike heat conduction in high-mobility crystalline semiconductors. *Phys. Rev. Lett.*, 82:779–782, Jan 1999.

[11] Michael Marek Koza, Mark Robert Johnson, Romain Viennois, Hannu Mutka, Luc Girard, and Didier Ravot. Breakdown of phonon glass paradigm in La- and Ce-filled Fe_4Sb_{12} skutterudites. *Nat Mater*, 7(10):805–810, 10 2008.

[12] Mogens Christensen, Asger B. Abrahamsen, Niels B. Christensen, Fanni Juranyi, Niels H. Andersen, Kim Lefmann, Jakob Andreasson, Christian R. H. Bahl, and Bo B. Iversen. Avoided crossing of rattler modes in thermoelectric materials. *Nat Mater*, 7(10):811–815, 10 2008.

[13] H. Euchner, S. Pailhès, L. T. K. Nguyen, W. Assmus, F. Ritter, A. Haghighirad, Y. Grin, S. Paschen, and M. de Boissieu. Phononic filter effect of rattling phonons in the thermoelectric clathrate $Ba_8Ge_{40+x}Ni_{6-x}$. *Phys. Rev. B*, 86:224303, Dec 2012.

[14] S. Pailhès, H. Euchner, V. M. Giordano, R. Debord, A. Assy, S. Gomès, A. Bosak, D. Machon, S. Paschen, and M. de Boissieu. Localization of propagative phonons in a perfectly crystalline solid. *Phys. Rev. Lett.*, 113:025506, Jul 2014.

[15] Wu Li and Natalio Mingo. Thermal conductivity of fully filled skutterudites: Role of the filler. *Phys. Rev. B*, 89:184304, May 2014.

[16] Terumasa Tadano, Yoshihiro Gohda, and Shinji Tsuneyuki. Impact of rattlers on thermal conductivity of a thermoelectric clathrate: A first-principles study. *Phys. Rev. Lett.*, 114:095501, Mar 2015.

[17] G. Kresse and J. Hafner. *Ab initio* molecular dynamics for liquid metals. *Phys. Rev. B*, 47:558–561, Jan 1993.

[18] G. Kresse and J. Hafner. *Ab initio* molecular-dynamics simulation of the liquid-metal–amorphous-semiconductor transition in germanium. *Phys. Rev. B*, 49:14251–14269, May 1994.

[19] G. Kresse and J. Furthmüller. *Comput. Mater. Sci.*, 6:15–50, 1996.

[20] G. Kresse and J. Furthmüller. Efficient iterative schemes for *ab initio* total-energy calculations using a plane-wave basis set. *Phys. Rev. B*, 54:11169–11186, Oct 1996.

[21] P. E. Blöchl. Projector augmented-wave method. *Phys. Rev. B*, 50:17953–17979, Dec 1994.

[22] John P. Perdew, Kieron Burke, and Matthias Ernzerhof. Generalized gradient approximation made simple. *Phys. Rev. Lett.*, 77:3865–3868, Oct 1996.

[23] R. Caracas X. Gonze, J.-M. Beuken, F. Detraux, M. Fuchs, G. M. Rignanese, L. Sindic, M. Verstraete, G. Zerah, and F. Jollet et al. *Comput. Mater. Sci.*, 25:478–492, 2002.

[24] W. Kohn and L. J. Sham. Self-consistent equations including exchange and correlation effects. *Phys. Rev.*, 140:A1133–A1138, Nov 1965.

[25] Fei Zhou, Weston Nielson, Yi Xia, and Vidvuds Ozoliņš. Lattice anharmonicity and thermal conductivity from compressive sensing of first-principles calculations. *Phys. Rev. Lett.*, 113:185501, Oct 2014.

[26] Stefano Baroni, Paolo Giannozzi, and Andrea Testa. Green's-function approach to linear response in solids. *Phys. Rev. Lett.*, 58:1861–1864, May 1987.

[27] Xavier Gonze. Perturbation expansion of variational principles at arbitrary order. *Phys. Rev. A*, 52:1086–1095, Aug 1995.

[28] Xavier Gonze. Adiabatic density-functional perturbation theory. *Phys. Rev. A*, 52:1096–1114, Aug 1995.

[29] Wu Li, Jesús Carrete, Nebil A. Katcho, and Natalio Mingo. *Comput. Phys. Commun.*, 185:1747–1758, 2014.

[30] B. C. Sales, B. C. Chakoumakos, R. Jin, J. R. Thompson, and D. Mandrus. Structural, magnetic, thermal, and transport properties of $X_8Ga_{16}Ge_{30}$ (X=Eu, Sr, Ba) single crystals. *Phys. Rev. B*, 63:245113, Jun 2001.

[31] I. Zeiringer, MingXing Chen, A. Grytsiv, E. Bauer, R. Podloucky, H. Effenberger, and P. Rogl. The ternary system au-ba-si: Clathrate solution, electronic structure, physical properties, phase equilibria and crystal structures. *Acta Materialia*, 60:2324–2336, 2012.

[32] G.K. Ramachandran, J. Dong, J. Diefenbacher, J. Gryko, R.F. Marzke, O.F. Sankey, and P.F. McMilan. Synthesis and x-ray characterization of silicon clathrates. *Journal of Solid State Chemistry*, 145:716–730, 1999.

[33] S. Yamanaka, E. Enishi, H. Fukuoka, and M. Yasukawa. High-pressure synthesis of a new silicon clathrate superconductor, Ba_8Si_{46}. *Inorganic Chemistry*, 39:56–58, 2000.

[34] Daniel Schopf, Holger Euchner, and Hans-Rainer Trebin. Effective potentials for simulations of the thermal conductivity of type-i semiconductor clathrate systems. *Phys. Rev. B*, 89:214306, Jun 2014.

[35] G. S. Nolas, J.-M. Ward, J. Gryko, L. Qiu, and M. A. White. Transport properties of Na_8Si_{46}. *Phys. Rev. B*, 64:153201, Sep 2001.

CHAPTER 5

Nontrivial Electron-Phonon Interactons Lead to Positive Seebeck Coefficients in Cu and Ag

5.1 Introduction

According to the well known Mott formula, S is proportional to the derivative of σ with energy at Fermi level ε_F, specifically $S \propto T\left(d\sigma/d\varepsilon_F\right)/\sigma$. Considering $\sigma \propto N\langle v^2\rangle\tau$ which is valid for a metal or degenerate semiconductor with N the density of states (DOS), $\langle v^2\rangle$ the average Fermi velocity and τ carrier lifetime, S can be further separated into two terms that proportional to $d(N\langle v^2\rangle)/d\varepsilon$ and $d\tau/d\varepsilon$ respectively. Previous study of S is focused on the first term by adopting constant relaxation time approximation (CRTA) [1], in which τ is assumed to be a spatially isotropic constant, thus making S a static property of electronic band structure. This leads to various strategies to optimize S via band-structure engineering including converging many valleys, forming DOS peak via resonant impurity and exploiting highly directional orbitals in 3D bulk thermoelectrics [2, 3, 4, 5, 6]. Though CRTA predicts correct signs of S for most semiconductors and could achieve quantitative agreement for certain materials [1], it severely fails in most metallic systems [7]. In metals and semimetals, thermal broadening of the Fermi distribution function f simultaneously activates two kinds of carriers with opposite signs and reduces the contribution from $d(N\langle v^2\rangle)/d\varepsilon$, thus making $d\tau/d\varepsilon$ innegligible. Indeed, we observe that the energy dependence of τ plays a major role in metallic systems by not only changing the absolute

magnitude but also the sign of S.

Metals, which usually have high electrical conductivities, are not interesting thermoelectric materials due to their relatively low S. However, their S exhibit fundamentally interesting behavior, that is, the signs of S do not necessarily follow the carrier type, which is in contrast to regular semiconductors [7]. Surprisingly, quite a few metals exhibit positive S, among which copper (Cu), silver (Ag) and gold (Au) show increasing positive S over the temperature range of 100 and 1300 K; Molybdenum (Mo) and tungsten (W) show first increasing and then decreasing positive S, and the transition temperature is about 1300 K [8]. Lithium (Li), the simplest metal, also exhibits increasing positive S across the entire temperature range of its solid phase [9]. To explain the positive S in monovalent metals, Robinson *et al.* carried out theoretical calculations based on empirical electron-phonon interactions (EPI) and free electrons via investigating the energy dependence of the electron mean free path [10]. Their study on solid alkali metals reveals the importance of the unusual energy dependence of EPI for Li to retain the positive S. However, their conclusion is in contrast to the argument based on significant deviation from free-electron model, which was proposed by Jones and MacDonald *et al.* [11, 12]. Most recent first-principles study of the positive S of Li by Xu *et al.* supported the latter argument and further pointed out that the energy-dependent lifetime $\tau(\varepsilon)$, which is inversely proportional to DOS, determines the sign of S [7]. However, neither DOS-related τ nor CRTA predicts positive sign of S for Cu, Ag and Au, which indicates the possible complexities from Fermi surface and EPI [7]. Therefore we revisit the origin of positive S in noble metals Cu and Ag. Our fully first-principles calculation based on rather dense interpolation in both electron and phonon momentum space reveals that the energy-dependent EPI, which effectively reflects itself in band index i and wavevector $\mathbf{k}$ dependent relaxation time $\tau_{i,\mathbf{k}}$ and $\sigma(\varepsilon)$ the spectral conductivity, leads to sign change of S from negative to positive, thus supporting Robinson's finding [10].

5.2 Computational Details

The electronic structures, phonons and EPI vertices were calculated based on density functional perturbation theory (DFPT) [13] with a coarse $12\times12\times12$ **k**-mesh and a $6\times6\times6$ **q**-mesh using Quantum Espresso package [14]. To ensure the convergence of $\tau_{i,\mathbf{k}}$, we utilized a method developed by Giustino *et al.* [15] as implemented in EPW (Electron-Phonon Wannier) [16] to interpolate electron, phonon states and EPI vertices via exploring their spatial localizations using generalized Wannier functions [17]. Then the electron self-energies considering electron-phonon interactions were calculated on a $40\times40\times40$ **k**-mesh using a gaussian smearing width of 0.03 eV with interpolated phonon modes and EPI vertices on a $60\times60\times60$ **q**-mesh. The good convergence of electron self-energy near Fermi level was verified by interpolating phonon momenta on a dense $80\times80\times80$ **q**-mesh and the relative error is within 5% for both Cu and Ag. The interpolated $\varepsilon_{i,\mathbf{k}}$ and $\tau_{i,\mathbf{k}}$ were used as input to BoltzTrap package [1] to calculate DOS and transport coefficients using tetrahedron smearing method [18]. We particularly emphasize here that dense sampling of EPI vertex is crucial since less converged $\tau_{i,\mathbf{k}}$ does not give rise to positive Seebeck coefficient according to our observation.

Standard density functional theory (DFT) [19] calculations were performed using Quantum Espresso package [14] and Troullier-Martins norm-conserving pseudopotentials [20] with the Perdew-Burke-Ernzerhof (PBE) [21] exchange-correlation (xc) functional [22] within the generalized gradient approximation (GGA) [23]. A kinetic energy cutoff of 75 Ry with Marzari-Vanderbilt cold smearing [24] widths of 0.02 Ry and Monkhorst-Pack grids of $16\times16\times16$ for **k**-point sampling were used to ensure the convergence of total energy in self-consistent calculations. The volumes for both structures were fully relaxed until the total stress is below 10^{-4} Ry/bohr^3. Afterwards, non-self-consistent calculations using a coarse $12\times12\times12$ **k**-mesh were carried out to construct MLWFs [25, 26, 17, 27]. Fig. 5.1 and Fig. 5.2 show the calculated band

structures and phonon dispersions respectively.

Both Cu and Ag crystalize in close-packed face-centered cubic structure at temperatures from 300 to 900 K and belong to the space group $Fm\bar{3}m$ (No. 225). The fully relaxed lattice constant of 6.822 bohr (3.609 Å) for Cu is in excellent agreement with experimentally measured value of 3.615 Å [28], while the relaxed lattice constant of 7.920 bohr (4.190 Å) for Ag is overestimated by about 2.6% compared to experimental value of 4.086 Å [29], which is in agreement with GGA's typical overestimation of lattice constant by 2-3% [30]. We used the fully relaxed constants since the small lattice expansion is not expected to dramatically change the physics of electron-phonon interaction, such as reversing the sign of calculated S, which was verified by our calculation. However, we indeed observe the reduction in calculated conductivity in Ag.

Following the *disentanglement* strategy [26] implemented in MLWFs, we optimized the subspace containing five d-like and two s-like WFs by constructing a frozen window extends to about 7 eV above the Fermi level in order to accurately interpolate the band structure near Fermi level. As expected, the five d-like WFs are quite localized of which the spatial spreads are all below 1.0 Å (approximately 0.50 Å and 0.87 Å for Cu and Ag respectively). The two s-like WFs exhibit much larger spatial spreads of about 2.50 and 3.35 Å for Cu and Ag, which are consistent with their delocalized feature observed in directly calculated band structures. Interpolated band structure for Cu in Fig. 5.1 is in excellent agreement with band structure from non-self-consistent calculation, while the interpolated band structure for Ag shows slight deviations particularly along path from Γ to K. The range of energy window, frozen window and number of WFs were varied to improve the constructed WFs for Ag, however, excellent agreement as in Cu was not achieved. As a result, we used one of the best WFs constructed for Ag since the interpolated bands still closely describe the general feature (slope and kink). It is believed that denser **k**-mesh used in constructing WFs can improve the accuracy of band interpolation. Fig. 5.3 shows the spatial decay of the Hamiltonian matrix elements $H^{\mathrm{el}}_{\mathbf{R}_e,\mathbf{R}'_e}$ and dynamical ma-

trix $D^{\mathrm{ph}}_{\mathbf{R}_p,\mathbf{R}'_p}$ in the Wannier representation, both of which show exponential localization within the corresponding supercell. Moreover, similarities are found among the matrix elements in the Wannier representation mainly due to both close electronic and crystal structures of Cu and Ag. The exponential decay of bare EPI vertices in the two limiting cases $g(\mathbf{R}_e,\mathbf{0}_p)$ and $g(\mathbf{0}_e,\mathbf{R}_p)$ are shown in Fig. 5.4. The spatial localization of Hamiltonian, dynamical matrix and bare EPI vertex indicate that a uniform $6\times6\times6$ $\mathbf{q}$-mesh corresponds to interactions extending up to $R\sim$ 12 Å is sufficient to determine accurate self-energies [15].

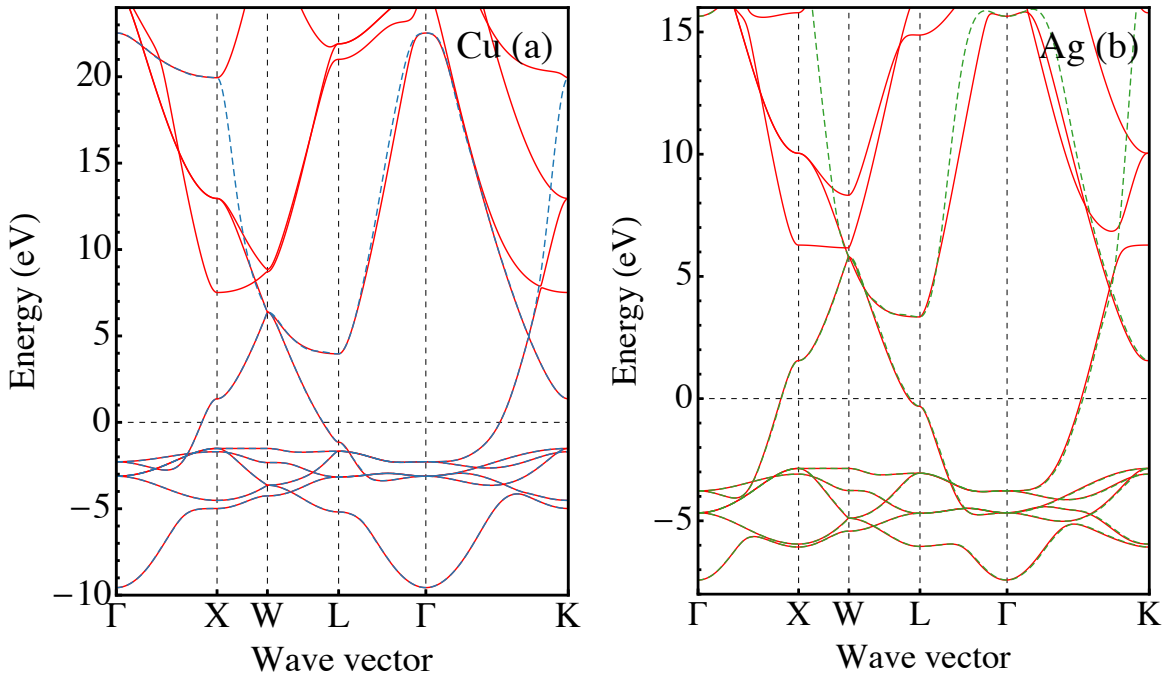

Figure 5.1: Dashed lines: interpolated bands associated with the optimal subspace containing five d-like and two s-like WFs within the frozen window. Solid lines: calculated DFT band structures of Cu and Ag.

5.3 Results and Discussion

Calculated S for Cu and Ag are shown in Fig. 5.5 (a) and (c). The CRTA predicts negative S and indicates that electron accumulates against temperature gradient, which is a reflection of basic

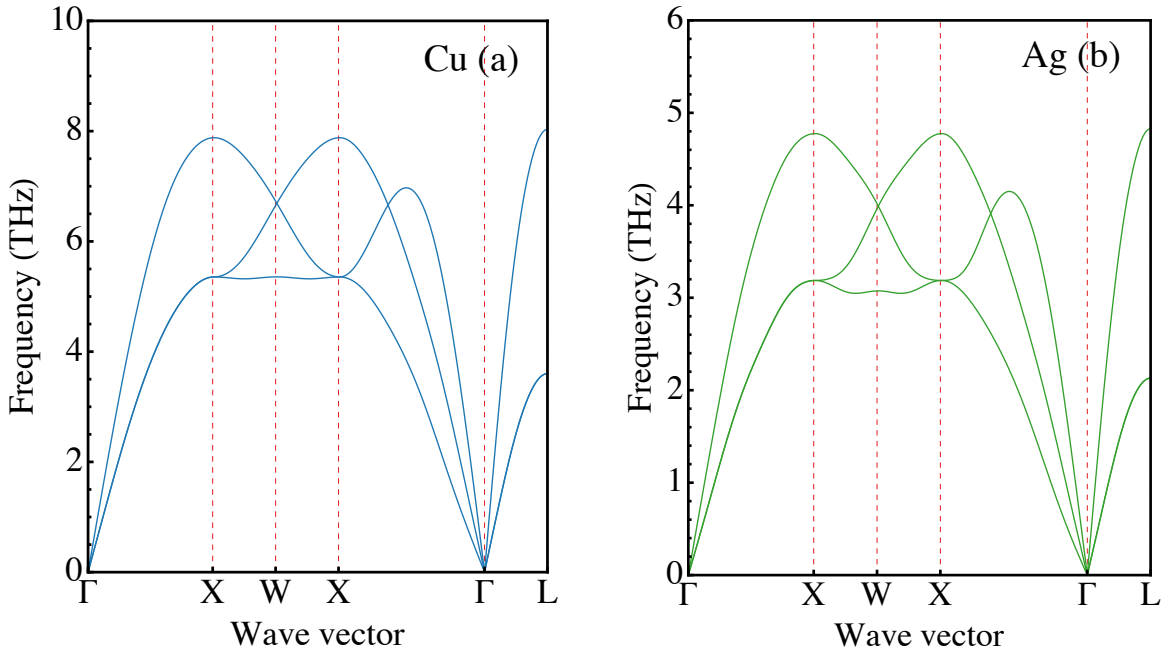

Figure 5.2: Phonon dispersions for Cu and Ag.

kinetic theory. Instead, RTA considering explicit EPI predicts the positive S and the increasing trend of S with increased temperature. However, the large relative deviation in S between calculated and experimentally measured values indicates that excellent agreement is still not achieved. We mostly attribute this deviation to three main factors: (1) temperature-dependent electronic band structure and phonon dispersion were not considered, which could change the spectrum considerably [32, 33]; (2) the Boltzmann transport equation was not solved in an iterative way, thus not taking into account the non-equilibrium distributions of interacting electrons and phonons [34, 35]; (3) the adopted relaxation time approximation does not take into account full inelastic scattering, which needs to evaluate the corresponding collision integral explicitly in the Boltzmann transport equation. In addition, more accurate band structure and EPI vertex calculation including many-body effect may also improve the result via going beyond simple mean-field theory of DFT GGA adopted here [36], though the self-energy correction induced by correlation effects is generally weak in metals [37]. Note that the absolute deviation in S is in typical range of error within RTA and the large relative error is partially due to the small absolute

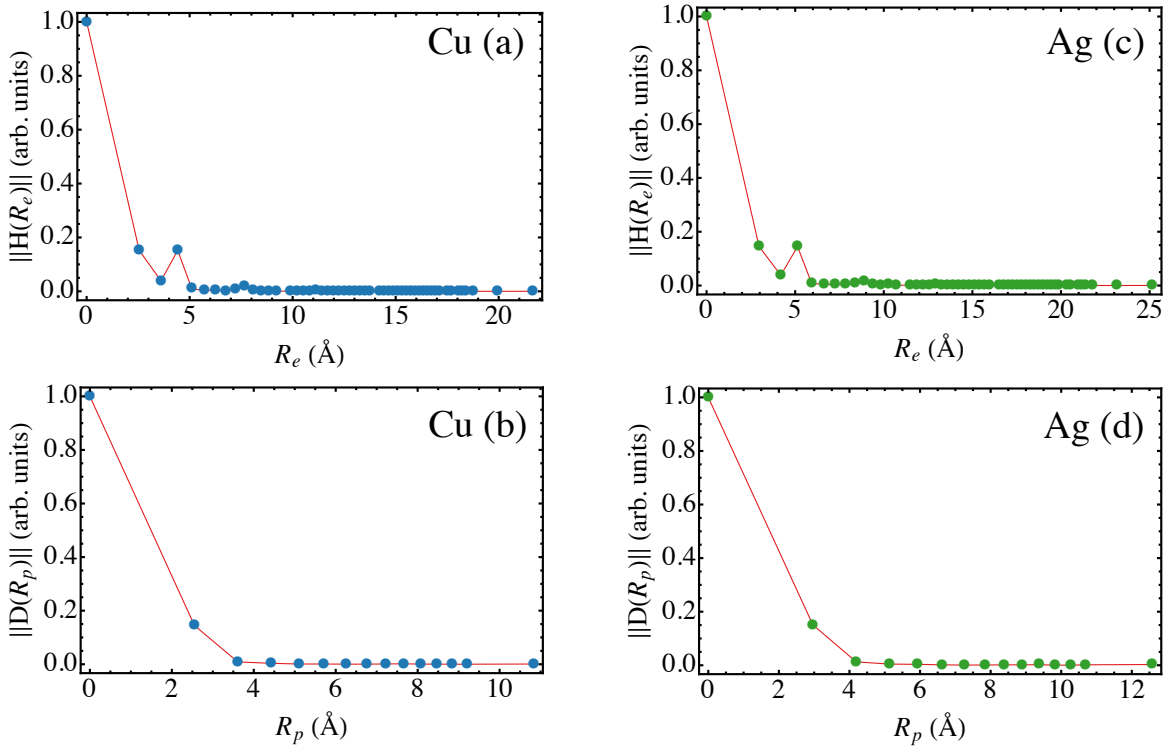

Figure 5.3: Spatial decay of the electronic Hamiltonian in the Wannier representation $H^{\mathrm{el}}_{\mathbf{R}_e,\mathbf{R}'_e}$ as a function of $R = |\mathbf{R}_e - \mathbf{R}'_e|$ for Cu (a) and Ag (c). Spatial decay of the dynamical matrix in the Wannier representation $D^{\mathrm{ph}}_{\mathbf{R}_p,\mathbf{R}'_p}$ as a function of the distance $R = \left(\mathbf{R}_p - \mathbf{R}'_p\right)$ for Cu (b) and Ag (d).

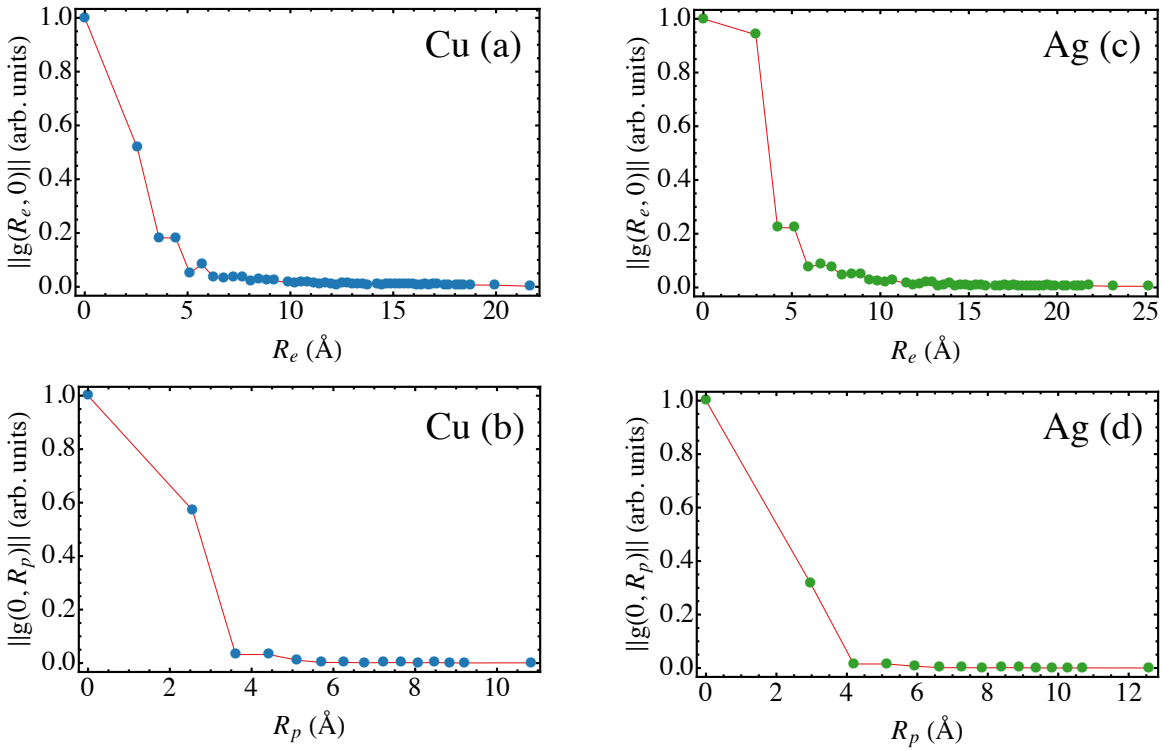

Figure 5.4: Spatial decay of the bare EPI vertex in the joint electron-phonon Wannier representation $g(\mathbf{R}_e, \mathbf{R}_p)$ as a function of $\mathbf{R}_e$ and $\mathbf{R}_p$. (a) and (c) show the limiting cases $g(\mathbf{R}_e, \mathbf{0})$ for Cu and Ag. (b) and (d) show the limiting cases $g(\mathbf{0}, \mathbf{R}_p)$ for Cu and Ag.

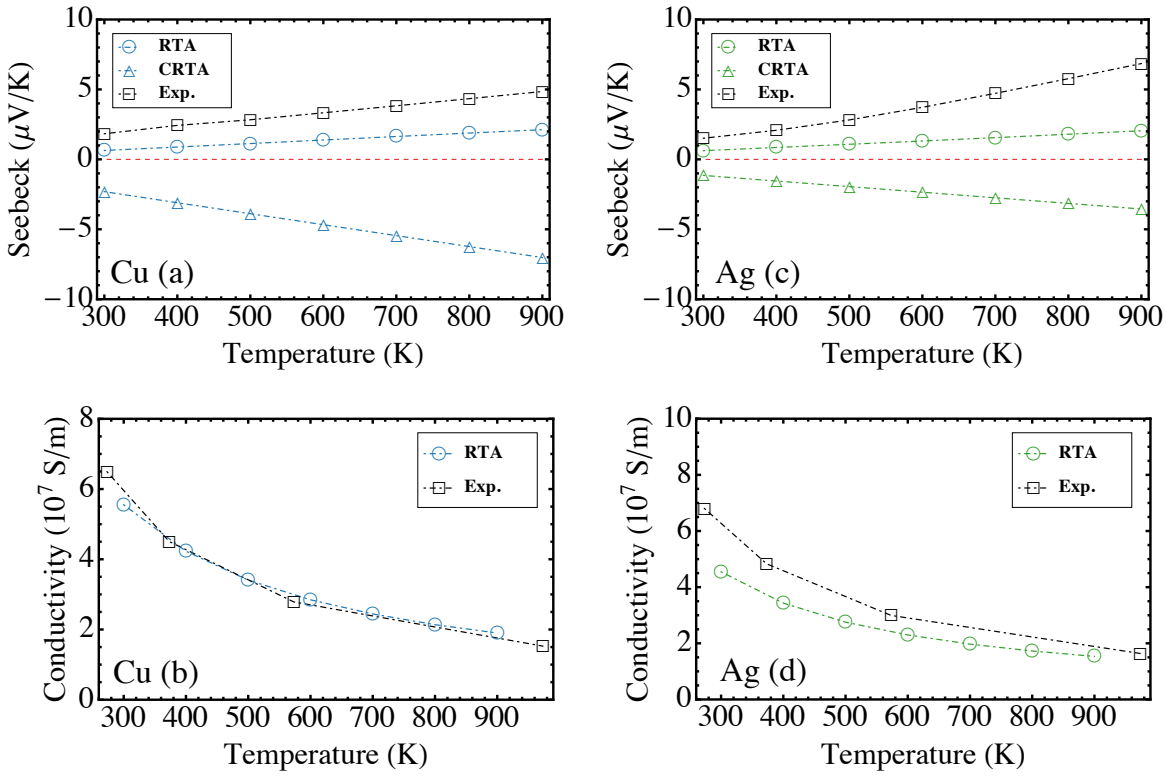

Figure 5.5: Calculated Seebeck coefficients: (a) and (c), and electronic conductivities: (b) and (d) for Cu and Ag using different approximations, namely relaxation time approximation (empty circle) and constant relaxation time approximation (empty triangle) compared with experimental measurements (empty square) from 300 to 900 K [8, 31]. The red dotted lines indicate a Seebeck coefficient equals zero.

values of S in Cu and Ag [8]. Fig. 5.5 (b) and (d) show and compare the carrier conductivities for Cu and Ag. The calculated conductivities decrease monotonically with increasing temperature following the trend found in experiments, which is in conformity with increasing phonon population. Our calculated conductivities for Cu are in excellent agreement with experiment [31], while smaller calculated values are found in Ag. This is probably due to the overestimation of lattice constant by about 2.6% for Ag, which indicates that volumetric change might have considerable effect on transport properties.

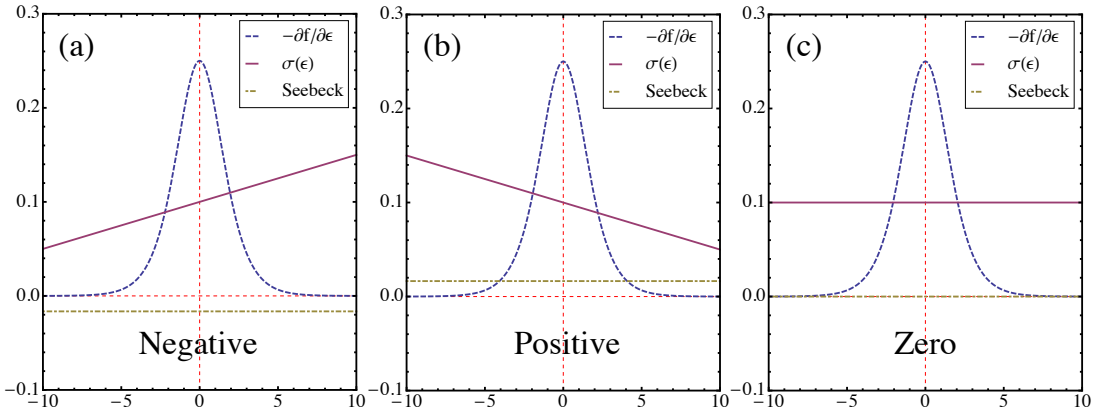

Figure 5.6: Simple illustration of the sign change of the Seebeck coefficient. (a), (b) and (c) respectively shows the variation of the sign of the Seebeck coefficient (yellow dot-dashed lines) from negative to positive to zero when the slope of the spectral conductivity (solid lines) is changed from positive to negative to zero. Blue dashed lines indicate the derivative of Fermi-Dirac distribution with respective to energy.

Considering that our calculations achieve both qualitative and reasonably quantitative agreement with experiments, we move on to discuss the physics with respect to the sign change of S, which is the essence of the present study. In order to better illustrate the idea behind positive S, we present the calculated S in three typical pictures in Fig. 5.6. The key ingredient that determines the sign of S is $\sigma(\varepsilon)$ defined in Eq. (2.35). The energy dependence of $\sigma(\varepsilon)$ instead of its absolute value within the integral window restricted by $\partial f/\partial\varepsilon$ results in different S, namely, positive energy dependence of $\sigma(\varepsilon)$ on ε gives rise to negative S and vice versa; constant $\sigma(\varepsilon)$ leads to

zero *S*. This simple numerical illustration in fact shows that the sign of *S* is independent of the sign of carrier, which is in contrast to a commonly accepted concept that p-type carriers lead to positive *S* and vice versa. In fact, the positive *S* in p-type semiconductors is determined by the negative dependence of $\sigma(\varepsilon)$, which is due to the decreased electron group velocity when energy moves towards the top of valence band.

Now we examine $\sigma(\varepsilon)$ for Cu and Ag respectively. We plot the $\sigma(\varepsilon)$ in Fig. 5.7 (a) and (c), in which the constant τ in CRTA is 10 fs. Despite the absolute value of $\sigma(\varepsilon)$ in CRTA can be adjusted to accord with experimentally measured conductivity, *S* is independent of the rescaled τ [1] and shows negative value in both Cu and Ag. Inspection of calculated band structures shows that the positive dependence of $\sigma(\varepsilon)$ on energy in CRTA is probably due to the slightly increased group velocity with increasing energy. In drastic contrast to CRTA, RTA gives rise to a negative dependence of $\sigma(\varepsilon)$ on energy and thus predicts positive *S*. Comparison between CRTA and RTA further illustrates that it is the energy dependence of $\tau(\varepsilon)$ that determines the sign of *S*. Since the energy dependence of the electron-phonon scattering rate $1/\tau(\varepsilon)$ is assumed to be proportional to the DOS by Xu *et al.* [7], we inspect the DOS around Fermi level in Fig. 5.7 (b) and (d). The DOSs in both Cu and Ag do not follow the DOS of free electron (DOS$\propto\sqrt{E}$) and it is in conformity with the analysis of orbital-projected DOS that the electronic states around Fermi level contain a considerable amount of *d*-orbitals. However, the slightly decreasing (near constant) DOS for Cu (Ag) leads to slightly increasing (near constant) $\tau(\varepsilon)$, which further supports the results from CRTA. It is thus inferred that the energy-dependence of $\tau(\varepsilon)$ is more complicated in Ag and Cu than that in Li.

Though the above analysis indeed indicates that the shape of $\sigma(\varepsilon)$ at the vicinity of Fermi level determines *S*, its physical meaning is elusive since $\sigma(\varepsilon)$ can not be directly measured and demonstrated via experiments. A more physically friendly Bethe-Sommerfeld expansion of

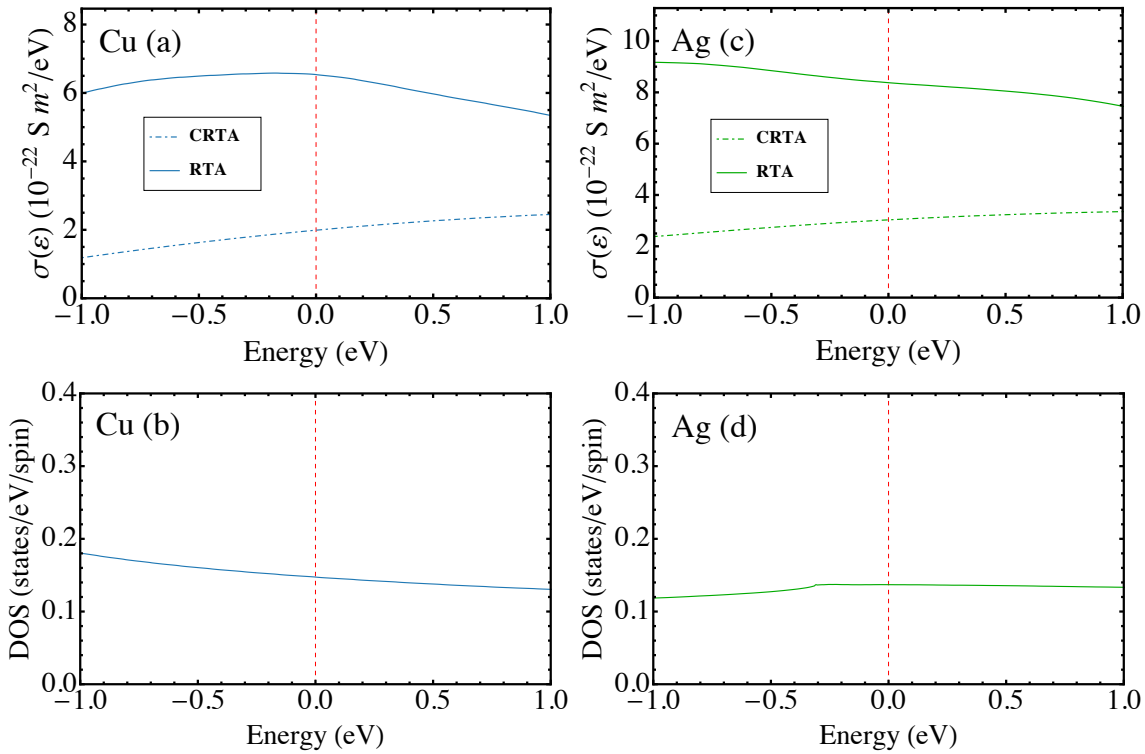

Figure 5.7: (a) and (c): calculated spectral conductivities for Cu and Ag using constant relaxation time approximation (solid lines) and relaxation time approximation (dot-dashed lines) at 300 K respectively. (b) and (d): calculated density of states for Cu and Ag. The vertical dotted lines denote the Fermi energy, which is shifted to zero eV.

S is adopted here as a connection to measurable physical quantities [38, 4].

$$S(T) = -\frac{\pi^2}{3}\frac{k_B}{e}(k_B T)\left[\frac{1}{n(\varepsilon)}\frac{dn(\varepsilon)}{d\varepsilon} + \frac{1}{\mu(\varepsilon)}\frac{d\mu(\varepsilon)}{d\varepsilon}\right] \tag{5.1}$$

The left term in the above square brackets represents the DOS term, which is trivial to the sign change of Seebeck here. While the right term, proportional to the derivative of carrier mobility with respective to energy, could be either positive or negative. According to Drude's model, the carrier mobility is assumed to be proportional to relaxation time and inversely proportional to effective mass $\mu \propto \tau/m^*$. Our previously analysis reveals that the dependence of μ on τ is mostly relevant for positive S in Cu and Ag. Instead, for regular semiconductors, μ is believed to depend more on m^* due to two factors: (1) variation of m^* near the conduction or valence band edge in semiconductors is much stronger than that in metals; (2) the validity of CRTA in doped semiconductors is improved by the presence of ionized impurity scattering which strongly scatters carrier at band edges where scattering due to phonon is small, leading to less energy-dependent electron relaxation time [39].

To further shed light on whether this peculiar dependence of relaxation time on energy comes from unique Fermi surface or nontrivial EPI, we calculated $\tau_{i,\mathbf{k}}$ using $(i,\mathbf{k})$-dependent and CEPI vertices respectively. Since $\tau_{i,\mathbf{k}}$ is anisotropic in momentum space, the plotted relaxation time scatters considerably in an energy interval. Therefore, the averaged energy-dependent relaxation time $\tau(\varepsilon)$ is further defined as

$$\tau(\varepsilon) = \frac{\sum_{i,\mathbf{k}} \tau_{i,\mathbf{k}} v(i,\mathbf{k})\, v(i,\mathbf{k})\, \delta(\varepsilon - \varepsilon_{i,\mathbf{k}})}{\sum_{i,\mathbf{k}} v(i,\mathbf{k})\, v(i,\mathbf{k})\, \delta(\varepsilon - \varepsilon_{i,\mathbf{k}})} \tag{5.2}$$

and plotted in Fig. 5.8. We find that CEPI leads to positive dependence of $\tau(\varepsilon)$ on energy in Cu and almost constant $\tau(\varepsilon)$ in Ag, both of which would lead to negative S due to overall positive dependence of $\sigma(\varepsilon)$ on energy. Conversely, monotonically decreasing $\tau(\varepsilon)$ were obtained using

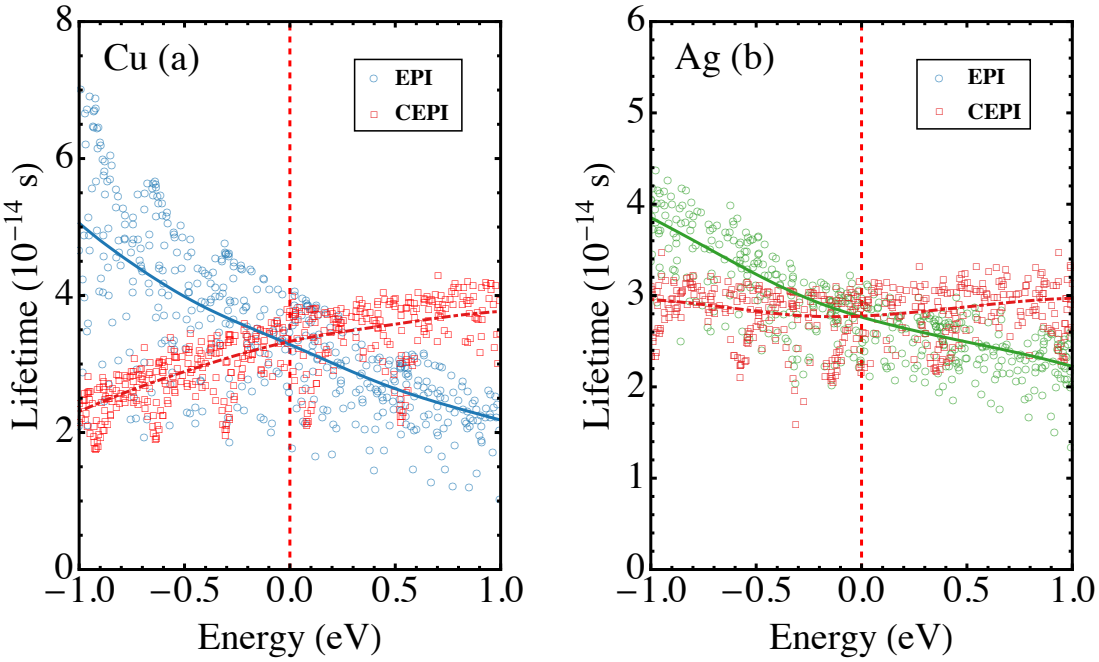

Figure 5.8: Calcualted relaxation time (lifetime) for Cu (a) and Ag (b) using electron-phonon interaction vertex (empty circles) and constant electron-phonon interaction vertex (empty squares) at 300 K. The solid and dot-dashed lines show the corresponding averaged energy-dependent relaxation time.

EPI, which indeed verifies the fact that it is the nontrivial EPI that leads to positive S. It can be further inferred that the averagely increased EPI vertex with respect to energy results in decreased $\tau(\varepsilon)$. The distorted Fermi surface plays a less important role in reversing the sign of S. The physical picture with respect to the positive S in electron carrier dominated metals such as Cu and Ag reveals that the presence of lattice vibration can effectively scatter electron and cause electron accumulation at higher temperature end. This is mainly due to the energy-dependent electron scattering mediated by phonons, while in free electron model there is no such extra scattering. The dependence of S on $\sigma(\varepsilon)$ and peculiar EPI could offer insights into several aspects of thermoelectrics: (1) semimetals with asymmetric band structure, which are usually good conductors, could be tuned to achieve larger S through asymmetric $\sigma(\varepsilon)$; (2) strong electron energy filtering effect [4], realized via introducing resonant impurities and resonant scattering, could also possibly be achieved by direct phonon engineering. (3) instead of explicitly calculating EPI

vertex for every single electron-phonon scattering process, the effective energy-dependent EPI vertex averaged over multiple processes in a small energy interval could be used to calculate relaxation time and speed up the accurate thermoelectric prediction.

5.4 Conclusions

In summary, we have carried out a fully first-principles study of the positive Seebeck coefficients for Cu and Ag based on DFT, Wannier interpolation and Boltzmann equation under relaxation time approximation. Our calculated Seebeck coefficients achieve reasonable agreement with experiments considering adopted various approximations. We successfully predict the correct sign (positive) of the Seebeck coefficients. The key ingredient in determining the correct sign of the Seebeck coefficient is spectral conductivity. Neither constant relaxation time nor density of states related relaxation time nor constant electron-phonon interaction vertex predicts correct energy dependence of spectral conductivity. Compared with Li, the deviation of electronic state from free-electron model does not give rise to the positive Seebeck in Cu and Ag. In fact, the nontrivial electron-phonon interaction is more important and a quantitative influence needs to be estimated. Our calculation reveals that it is the energy-dependent electron-phonon interaction vertex that leads to decreasing relaxation time, spectral conductivity and thus positive Seebeck coefficient. Our results are in agreement with Robinson's finding [10]. The exotic energy variations of electron-phonon interaction offer insights into both theoretical prediction and practical realization of thermoelectric devices with better performance through efficient prediction and modification of spectral conductivity.

5.5 Acknowledgement

This work was supported by the U.S. Department of Energy, Office of Science, Basic Energy Sciences, under Grant No. DE-FG02-07ER46433 and used computing resources at the National Energy Research Scientific Computing Center (NERSC), which is supported by the U.S. DOE under contract DE-AC02-05CH11231.

References

[1] Georg K.H. Madsen and David J. Singh. Boltztrap. a code for calculating band-structure dependent quantities. *Comput. Phys. Commun.*, 175(1):67 – 71, 2006.

[2] G D Mahan and J O Sofo. The best thermoelectric. *Proceedings of the National Academy of Sciences*, 93(15):7436–7439, 1996.

[3] Yanzhong Pei, Xiaoya Shi, Aaron LaLonde, Heng Wang, Lidong Chen, and G. Jeffrey Snyder. Convergence of electronic bands for high performance bulk thermoelectrics. *Nature*, 473(7345):66–69, 05 2011.

[4] Joseph P. Heremans, Bartlomiej Wiendlocha, and Audrey M. Chamoire. Resonant levels in bulk thermoelectric semiconductors. *Energy Environ. Sci.*, 5:5510–5530, 2012.

[5] David Parker, Xin Chen, and David J. Singh. High three-dimensional thermoelectric performance from low-dimensional bands. *Phys. Rev. Lett.*, 110:146601, Apr 2013.

[6] Daniel I. Bilc, Geoffroy Hautier, David Waroquiers, Gian-Marco Rignanese, and Philippe Ghosez. Low-dimensional transport and large thermoelectric power factors in bulk semiconductors by band engineering of highly directional electronic states. *Phys. Rev. Lett.*, 114:136601, Mar 2015.

[7] Bin Xu and Matthieu J. Verstraete. First principles explanation of the positive seebeck coefficient of lithium. *Phys. Rev. Lett.*, 112:196603, May 2014.

[8] N Cusack and P Kendall. The absolute scale of thermoelectric power at high temperature. *Proceedings of the Physical Society*, 72(5):898, 1958.

[9] P. W. Kendall. The absolute thermoelectric powers of the liquid alkali metals. *Phys. Chem. Liq.*, 1(1):33–48, 1968.

[10] John E. Robinson. Thermoelectric power in the nearly-free-electron model. *Phys. Rev.*, 161:533–539, Sep 1967.

[11] H Jones. The thermoelectric power of monovalent metals. *Proc. Phys. Soc. London Sect. A*, 68(12):1191, 1955.

[12] D.K.C.M. Donald. *Thermoelectricity: An Introduction to the Principles*. John Wiley & Sons, 1962.

[13] Stefano Baroni, Stefano de Gironcoli, Andrea Dal Corso, and Paolo Giannozzi. Phonons and related crystal properties from density-functional perturbation theory. *Rev. Mod. Phys.*, 73:515–562, Jul 2001.

[14] Paolo Giannozzi, Stefano Baroni, Nicola Bonini, Matteo Calandra, Roberto Car, Carlo Cavazzoni, Davide Ceresoli, Guido L Chiarotti, Matteo Cococcioni, Ismaila Dabo, Andrea Dal Corso, Stefano de Gironcoli, Stefano Fabris, Guido Fratesi, Ralph Gebauer,

Uwe Gerstmann, Christos Gougoussis, Anton Kokalj, Michele Lazzeri, Layla Martin-Samos, Nicola Marzari, Francesco Mauri, Riccardo Mazzarello, Stefano Paolini, Alfredo Pasquarello, Lorenzo Paulatto, Carlo Sbraccia, Sandro Scandolo, Gabriele Sclauzero, Ari P Seitsonen, Alexander Smogunov, Paolo Umari, and Renata M Wentzcovitch. Quantum espresso: a modular and open-source software project for quantum simulations of materials. *J. Phys.: Condens. Matter*, 21(39):395502, 2009.

[15] Feliciano Giustino, Marvin L. Cohen, and Steven G. Louie. Electron-phonon interaction using wannier functions. *Phys. Rev. B*, 76:165108, Oct 2007.

[16] Jesse Noffsinger, Feliciano Giustino, Brad D. Malone, Cheol-Hwan Park, Steven G. Louie, and Marvin L. Cohen. Epw: A program for calculating the electron–phonon coupling using maximally localized wannier functions. *Comput. Phys. Commun.*, 181(12):2140 – 2148, 2010.

[17] Nicola Marzari, Arash A. Mostofi, Jonathan R. Yates, Ivo Souza, and David Vanderbilt. Maximally localized wannier functions: Theory and applications. *Rev. Mod. Phys.*, 84:1419–1475, Oct 2012.

[18] Peter E. Blöchl, O. Jepsen, and O. K. Andersen. Improved tetrahedron method for brillouin-zone integrations. *Phys. Rev. B*, 49:16223–16233, Jun 1994.

[19] P. Hohenberg and W. Kohn. Inhomogeneous electron gas. *Phys. Rev.*, 136:B864–B871, Nov 1964.

[20] N. Troullier and José Luís Martins. Efficient pseudopotentials for plane-wave calculations. *Phys. Rev. B*, 43:1993–2006, Jan 1991.

[21] John P. Perdew, Kieron Burke, and Matthias Ernzerhof. Generalized gradient approximation made simple. *Phys. Rev. Lett.*, 77:3865–3868, Oct 1996.

[22] W. Kohn and L. J. Sham. Self-consistent equations including exchange and correlation effects. *Phys. Rev.*, 140:A1133–A1138, Nov 1965.

[23] John P. Perdew, Kieron Burke, and Yue Wang. Generalized gradient approximation for the exchange-correlation hole of a many-electron system. *Phys. Rev. B*, 54:16533–16539, Dec 1996.

[24] Nicola Marzari, David Vanderbilt, Alessandro De Vita, and M. C. Payne. Thermal contraction and disordering of the al(110) surface. *Phys. Rev. Lett.*, 82:3296–3299, Apr 1999.

[25] Nicola Marzari and David Vanderbilt. Maximally localized generalized wannier functions for composite energy bands. *Phys. Rev. B*, 56:12847–12865, Nov 1997.

[26] Ivo Souza, Nicola Marzari, and David Vanderbilt. Maximally localized wannier functions for entangled energy bands. *Phys. Rev. B*, 65:035109, Dec 2001.

[27] Arash A. Mostofi, Jonathan R. Yates, Young-Su Lee, Ivo Souza, David Vanderbilt, and Nicola Marzari. wannier90: A tool for obtaining maximally-localised wannier functions. *Computer Physics Communications*, 178(9):685 – 699, 2008.

[28] Henry M. Otte. Lattice parameter determinations with an x-ray spectrogoniometer by the debyeascherrer method and the effect of specimen condition. *J. Appl. Phys.*, 32(8):1536–1546, 1961.

[29] J Spreadborough and J W Christian. High-temperature x-ray diffractometer. *J. Sci. Instrum.*, 36(3):116, 1959.

[30] Philipp Haas, Fabien Tran, and Peter Blaha. Calculation of the lattice constant of solids with semilocal functionals. *Phys. Rev. B*, 79:085104, Feb 2009.

[31] G.W.C. Kaye and T.H. Laby. *Tables of Physical and Chemical Constants*. Longman, 1995.

[32] J. A. Knapp, F. J. Himpsel, A. R. Williams, and D. E. Eastman. Temperature dependence of bulk and surface energy bands in copper using angle-resolved photoemission. *Phys. Rev. B*, 19:2844–2849, Mar 1979.

[33] P Winsemius, F F van Kampen, H P Lengkeek, and C G van Went. Temperature dependence of the optical properties of au, ag and cu. *J. Phys. F*, 6(8):1583, 1976.

[34] D. L. Rode. Electron mobility in direct-gap polar semiconductors. *Phys. Rev. B*, 2:1012–1024, Aug 1970.

[35] Ashok T. Ramu, Laura E. Cassels, Nathan H. Hackman, Hong Lu, Joshua M. O. Zide, and John E. Bowers. Rigorous calculation of the seebeck coefficient and mobility of thermoelectric materials. *J. Appl. Phys.*, 107(8), 2010.

[36] G. Antonius, S. Poncé, P. Boulanger, M. Côté, and X. Gonze. Many-body effects on the zero-point renormalization of the band structure. *Phys. Rev. Lett.*, 112:215501, May 2014.

[37] Z. P. Yin, A. Kutepov, and G. Kotliar. Correlation-enhanced electron-phonon coupling: Applications of *gw* and screened hybrid functional to bismuthates, chloronitrides, and other high-T_c superconductors. *Phys. Rev. X*, 3:021011, May 2013.

[38] V.Y. Irkhin and Y.P. Irkhin. *Electronic Structure, Correlation Effects and Physical Properties of D- and F-metals and Their Compounds*. Cambridge International Science Publishing, Limited, 2007.

[39] Bo Qiu, Zhiting Tian, Ajit Vallabhaneni, Bolin Liao, Jonathan M. Mendoza, Oscar D. Restrepo, Xiulin Ruan, and Gang Chen. First-principles simulation of electron mean-free-path spectra and thermoelectric properties in silicon. *EPL (Europhysics Letters)*, 109(5):57006, 2015.

CHAPTER 6

First-Principles Study of Thermoelectric Properties from Electron-Phonon and Phonon-Phonon Interactions in B20-type CoSi

6.1 Introduction

The conversion efficiency of thermoelectric materials is determined by the thermoelectric figure of merit ZT, given by the equation $ZT = \sigma S^2 T/(\kappa_e + \kappa_l)$, where S is the Seebeck coefficient, σ is electrical conductivity, κ_e and κ_l are thermal conductivities from carrier and lattice respectively. The thermoelectric power factor is defined as σS^2. For practical application, ZT above 1.0 is needed. There are two general strategies to enhance ZT: (1) direct reduction of κ_l and (2) optimization of power factor. The former can be realized by finding intrinsically low-κ_l materials [1] combined with techniques such as introducing alloy scattering and nanostructure [2]. However, κ_l cannot be arbitrarily reduced and has a minimum value due to the fact that the phonon mean free path cannot be reduced below the interatomic spacing [3]. Therefore optimization of power factor should be sought in order to further enhance ZT.

According to the definition, high power factor can be achieved with high conductivity and large Seebeck coefficient. This is difficult since conditions that tend to increase one tend to decrease the other [4]. To ensure large Seebeck coefficient, either electrons or holes should dominate the system's transport. And for high electrical conductivity, large Fermi velocity and carrier concen-

tration are required. The peak power factor is achieved by compromising large Seebeck coefficient and high electrical conductivity at carrier concentrations between 10^{19} and 10^{21} carriers per cm^3 [4]. This kind of compromise is commonly realized by heavily doping semiconductors which increases electrical conductivity while possibly maintaining large Seebeck coefficient. The reverse approach, which is to enhance Seebeck coefficient while maintaining relatively high electrical conductivity, has only been realized in intermetallic compounds such as Fe_2VAl [5] and B20-type transition-metal monosilicides [6].

B20-type cobalt monosilicide (CoSi) has attracted considerable research interest due to its exceptional thermoelectric properties, i.e., large Seebeck coefficient (100 μV K^{-1}) but with metal-like conductivity (10^{-4} Ω cm), which gives rise to a power factor as high as 60 μW K^{-2} cm^{-1} at room temperature, comparable to or higher than most state-of-the-art thermoelectric materials such as PbTe, Bi2Te3 and SnSe [7, 8, 9]. P-type doping effects of Al and B substitution on Si site have been investigated systematically [10, 11, 12]. Lue *et al.* found that the substitution of Al on the Si sites causes a monotonic and dramatic decrease in electrical resistivity [10]. However, their measured electrical resistivity for intrinsic CoSi is considerably larger than that in the other studies [12]. On the other hand, Li *et al.* observed that between 300 and 550 K, electrical resistivity first increases and then drops with increasing Al substitution [12]. Both Lue *et al.* and Li *et al.* found that the Seebeck coefficients of $CoSi_{1-x}Al_x$ single crystals shift towards the positive direction and the sign change of S occurs at around $x = 0.04$ [10, 12]. Sun *et al.* recently studied n-type doping effect of Ni, Pd and Pt substitutions on Co sites [13]. They measured the lowest resistivity for pure CoSi in conformity with the measurements on a single crystal by Petrova *et al.* [14] and found both electrical resistivity and the Seebeck coefficient decrease with increasing carrier concentration. They further obtained the maximum ZT of 0.13 at room temperature for $Co_{0.98}Pt_{0.01}Si$. The relatively small value of ZT is mainly due to large lattice thermal conductivity ($\kappa_l > 10$ W m^{-1} K^{-1}) [13]. Kuo *et al.* and Skoug *et al.* investigated the effects of Ge

partial substitution for Si on the thermoelectric properties of $CoSi_{1-x}Ge_x$ alloys. Their results show substantial decrease in both electrical resistivity and lattice thermal conductivity with Ge partial substitution for Si [15, 16]. The resulting maximum ZT at 300 K is about 0.1 [15].

In contrast to wide availability of experimental studies, there are limited number of theoretical investigations. Pan *et al.* calculated band structures for both pure and hole-doped CoSi using the full-potential linear augmented plane wave approach and explained the negative Seebeck coefficient of undoped CoSi and the positive shift of the Seebeck coefficient with Al substitution with the shape of energy-dependent density of states [17]. Sakai *et al.* attributed the large negative Seebeck coefficient to the asymmetric density of states (DOS) around the pseudogap [18]. Kanazawa *et al.* studied B20-type CoGe which has a similar band structure as CoSi and concluded that the large positive or negative Seebeck coefficient originates from the asymmetric band structure composed of a Dirac cone and a flat band with sharp bends around the Fermi energy [19]. However, their Boltzmann transport model can only explain semi-quantitatively the experimental results while the theoretical largest negative Seebeck coefficient exists at a different doping concentration from experimental measurements [19].

To further optimize the power factor for CoSi, a comprehensive model is required to not only explain the experimental measurements quantitatively but also predict thermoelectric properties with high accuracy. We start by pointing out several deficiencies of previous models which lead to significantly different results for CoSi. First, since the Fermi level is located near the pseudogap (where the DOS is low) and there also exists an abrupt change of DOS, the shift of Fermi level due to temperature broadening of energy distribution cannot be neglected. The Fermi level moves above the flat band at high temperatures as shown in Fig. 6.7. Second, at low temperatures the Fermi level stays below the flat band. A simple examination of DOS in Fig. 6.7 shows that CoSi should possess a positive Seebeck coefficient, which is in contrast to what Pan *et al.* found [17]. Third, the Boltzmann transport model based on constant relaxation

time approximation (CRTA) fails to quantitively predict experimental measurements, such as the large negative Seebeck coefficient for stoichiometric CoSi, the exact doping concentration of Al at which the sign of the Seebeck coefficient changes, and the general dependence of thermoelectric properties on doping concentrations. These deficiencies indicate that a more accurate model which takes into account both the temperature-dependent shift of Fermi level and the energy-dependent electron relaxation time should be used. Additionally, one of the main factors inhibiting further improvements in the thermoelectric efficiencies of pure and doped CoSi is their relatively high κ_l. A theoretical study is therefore required to produce insight to further reduce thermal conductivity. Considering the deficiencies in the previous theoretical studies and the lack of theoretical investigation of κ_l, we provide a fully first-principles study of both electron and phonon transport. To avoid CRTA, we explicitly evaluated electron relaxation time by calculating electron scattering rates due to phonons. The phonon relaxation time was evaluated considering both electron-phonon interaction (EPI) and phonon-phonon interaction (PPI). We show that EPI leads to electron relaxation time that is strongly dependent on energy, which is essential to explain the exceptional thermoelectric properties. Using the estimated electron relaxation time for each electronic state (i, $\mathbf{k}$), our calculated Seebeck coefficient, electrical resistivity, power factor, and the dependence of our Seebeck coefficient on both doping concentration and temperature all agree quantitively with experiments. Our phonon transport calculation reveals that the total thermal conductivity is composed mainly of electrical and lattice contributions. Phonon relaxation time is limited mostly by PPI at temperatures higher than 200 K. At low temperatures it is considerably reduced by EPI. Maximum ZTs of 0.11 and 0.25 can be achieved with slight electron doping at 300 and 600 K respectively for CoSi without further reducing total thermal conductivity.

6.2 Computational Details

6.2.1 DFT Calculations

We used QUANTUM ESPRESSO package [20] to perform basic electronic structure calculations. We obtained band energies for wavevectors in the irreducible Brillouin zone (IBZ). We used BoltzTrap package to extract Fermi velocities from these band energies and evaluated electron transport properties including the Seebeck coefficient, electrical conductivity, and electronic thermal conductivity [21]. Scattering rates for electrons and phonons due to EPI were computed using the electron-phonon Wannier (EPW) package [22, 23] based on maximally localized Wannier functions (WFs) [24, 25, 26, 27]. Spatially localized WFs were constructed using the disentanglement strategy [25]. The interpolation scheme implemented in EPW allows for accurate evaluation of EPI vertices at densely sampled electron and phonon wavevectors, which guarantees good convergence of electron and phonon self-energies [23]. We used a recently developed compressive sensing lattice dynamics (CSLD) method to extract both second- and third-order interatomic force constants (IFCs) [28]. The forces of training supercell structures were calculated using Vienna *Ab initio* simulation package (VASP) [29, 30, 31, 32]. We calculated lattice thermal conductivity with the ShengBTE package using the resulting IFCs as inputs [33].

6.2.2 Electron-Phonon Wannier Interpolation

Standard DFT [34] calculations were performed using the Quantum Espresso package [20] and Troullier-Martins norm-conserving pseudopotentials [35] with the Perdew-Burke-Ernzerhof (PBE) [36] exchange-correlation (xc) functional [37] within the generalized gradient approximation (GGA) [38]. A kinetic energy cutoff of 75 Ry with Methfessel-Paxton smearing [39] width of 0.015 Ry and Monkhorst-Pack grids of $8\times8\times8$ for **k**-point sampling were used to ensure the convergence of total energy in self-consistent calculations. The volumes were fully relaxed until

the total stress was below 5×10^{-6} Ry/bohr^3. The lattice constant for the fully relaxed structure was found to be 8.437 bohr (4.465 Å), which is in good agreement with experimentally measured value of 4.450 Å [40]. The slight overestimation of lattice constant (here about 0.3%) is typical with GGA.

We constructed WFs, dynamical matrices, and EPI vertices on a coarse 6×6×6 **k**-mesh and a 2×2×2 **q**-mesh and further verified results using a dense 8×8×8 **k**-mesh and a 4×4×4 **q**-mesh. Following the *disentanglement* strategy [25] implemented in MLWFs, we constructed 28 Wannier functions starting from the lowest energy band. The frozen window was set to be approximately 1.4 eV above the Fermi level to ensure the band structures were interpolated accurately. The WFs were initialized with randomly-centered s-type Gaussian functions. Fig. 6.1 (a) shows the comparison between the decay of the Hamiltonian in the Wannier representation constructed using 6×6×6 and 8×8×8 **k**-meshes respectively. It can be inferred that $H(\mathbf{R}_e)$ decreases to a very small value with R_e larger than 15 Å on both **k**-meshes. Fig. 6.1 (b) shows the comparison between the decay of the dynamical matrix in the Wannier representation constructed using 4×4×4 and 2×2×2 **q**-meshes respectively. We can see the dense 4×4×4 **q**-mesh leads to spatial decay of $D(\mathbf{R}_p)$ such that values vanish with R_p larger than 10 Å. The coarse 2×2×2 **q**-mesh captures most large-value elements in $D(\mathbf{R}_p)$ and may neglect some long-range interactions with R_p larger than about 8 Å. Fig. 6.1 (b) and (c) shows the spatial decay of EPI vertex $g(\mathbf{R}_e, \mathbf{R}_p)$ in the joint electron-phonon Wannier representation on coarse and dense **k**- and **q**-meshes. In the limiting case of $g(\mathbf{R}_e, \mathbf{0})$, both coarse and dense **k**- and **q**-meshes give rise to fast decay with increasing R_e. In the limiting case of $g(\mathbf{0}, \mathbf{R}_p)$, the dense **k**- and **q**-meshes – which correspond to a maximum value of approximately 15 Å for R_p – lead to well localized $g(\mathbf{0}, \mathbf{R}_p)$. At the maximum value of approximately 8 Å for R_p allowed by the coarse **k**- and **q**-meshes, $g(\mathbf{0}, \mathbf{R}_p)$ still has large values, which also can be seen on the dense **k**- and **q**-meshes at $R_p \approx 8$ Å . From the observation of the sharp decrease of $g(\mathbf{0}, \mathbf{R}_p)$ at R_p larger than 8 Å on

the dense **k**- and **q**-meshes, we can conclude that the EPI vertices in the Wannier representation constructed from the coarse **k**- and **q**-meshes captures most large-value matrix elements in the Hamiltonian, dynamical matrices, and EPI vertices and therefore can be utilized to interpolate these quantities without missing significant long-range contributions. Further examination shows that our constructed WFs in Fig. 6.1 are not well converged to real values. However, this fact does not invalidate the electron-phonon Wannier interpolation scheme since the scheme only needs a unitary transformation $U_{ij,\mathbf{k}}$ that leads to proper spatial localization of the Hamilton and EPI vertices in the Wannier representation. Fig. 6.2 shows the comparison between the electronic band structures directly calculated by DFT and interpolated by the WFs constructed from the coarse $6\times6\times6$ **k**-mesh. Good agreement is achieved with the exception of slight deviation near the upper bound of the frozen window. We further compare phonon dispersion interpolated using $2\times2\times2$ and $4\times4\times4$ **q**-meshes in Fig. 6.3. The deviation is mainly attributed to the high-frequency optical modes approaching the Γ point, probably due to the omission of the long-range term with the coarse **q**-mesh. Nevertheless, the overall agreement is fairly good. We used the coarse **k**- and **q**-meshes in real calculations for two reasons. First, the interpolation of EPI vertex using the dense **k**- and **q**-meshes requires a huge amount of memory ($>$ 40 Gb per core and tens of cores are needed to perform a practical calculation). Second, the coarse **k**- and **q**-meshes already capture the most important physically relevant components. Since the unitary transformation $U_{ij,\mathbf{k}}$ is not unique due to the convergence issue of WFs, we further independently constructed different sets of WFs and found their impact on calculated thermoelectric properties to be within 8%.

The electron self-energy for a given electronic state $(i,\mathbf{k})$ was calculated using interpolated phonon modes and EPI vertices on a $30\times30\times30$ **q**-mesh with a gaussian smearing width of 0.03 eV. The good convergence of electron self-energy near Fermi level was verified by interpolating phonon modes on a dense $40\times40\times40$ **q**-mesh. The relative error was found to be within 1%.

The phonon self-energy for a given phonon mode $(\nu, \mathbf{q})$ due to electron-phonon interactions was calculated using interpolated electronic states and EPI vertices on a $40\times40\times40$ $\mathbf{q}$-mesh with the same gaussian smearing width. The good convergence of phonon self-energy near Fermi level was verified by a dense $50\times50\times50$ $\mathbf{k}$-mesh and the relative error was within 1%.

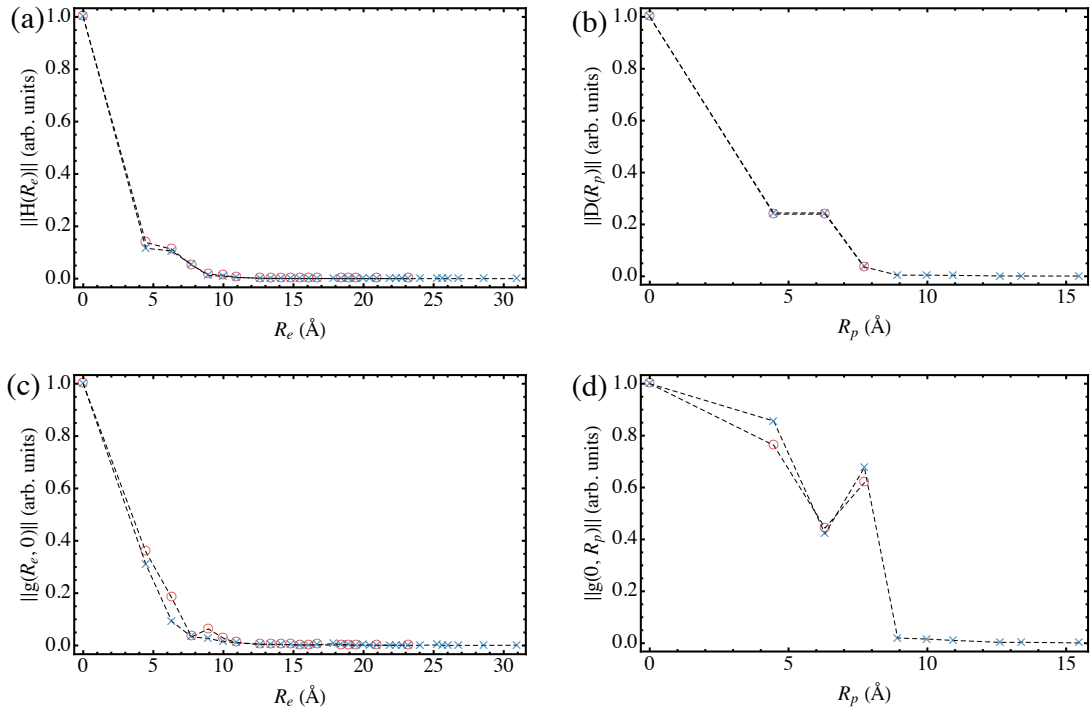

Figure 6.1: Comparison between the spatial decay of the electronic Hamiltonian in the Wannier representation $H^{\mathrm{el}}_{\mathbf{R}_e,\mathbf{R}'_e}$, the dynamical matrix in the Wannier representation $D^{\mathrm{ph}}_{\mathbf{R}_p}$ and the bare EPI vertex in the joint electron-phonon Wannier representation $g(\mathbf{R}_e, \mathbf{R}_p)$ in the two limiting cases of $g(\mathbf{R}_e, \mathbf{0})$ and $g(\mathbf{0}, \mathbf{R}_p)$ on different $\mathbf{k}$ and $\mathbf{q}$-meshes. The red circle shows the result using a $6\times6\times6$ $\mathbf{k}$-mesh and a $2\times2\times2$ $\mathbf{q}$-mesh. The blue cross shows the result using an $8\times8\times8$ $\mathbf{k}$-mesh and a $4\times4\times4$ $\mathbf{q}$-mesh.

6.2.3 Real-Space IFCs

Structure relaxation and self-consistent calculations were performed using Vienna *Ab initio* simulation package (VASP) [29, 30, 31, 32] with the projector-augmented wave (PAW) [41] method using the Perdew-Becke-Ernzerhof (PBE) [36] generalized gradient approximation (GGA) [38]

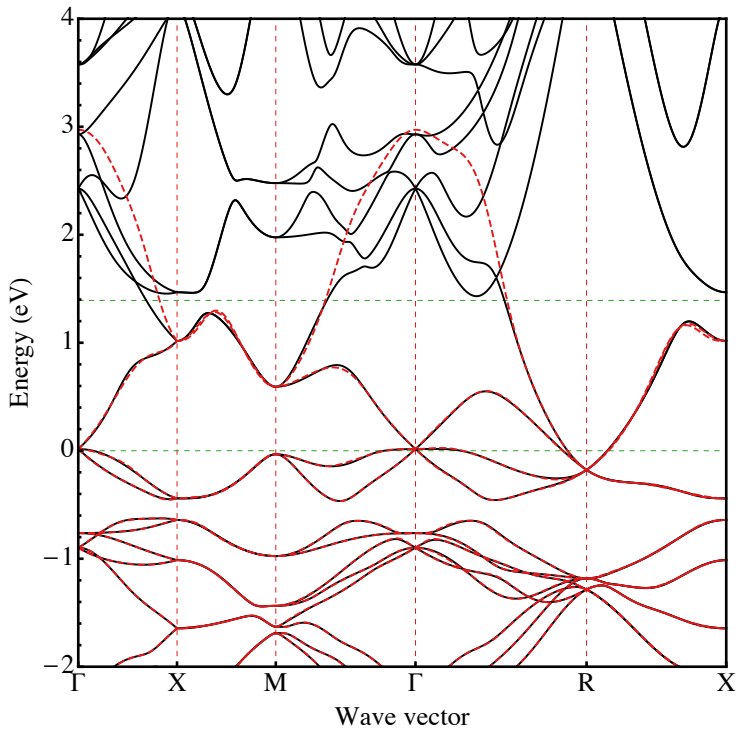

Figure 6.2: Comparison between the band structure of CoSi obtained from DFT calculations (black lines) and Wannier interpolation using 28 WFs (red dashed lines). Fermi level at 0 K and the top of the frozen energy window is indicated by the green dashed line centered at 0.0 and 1.4 eV respectively.

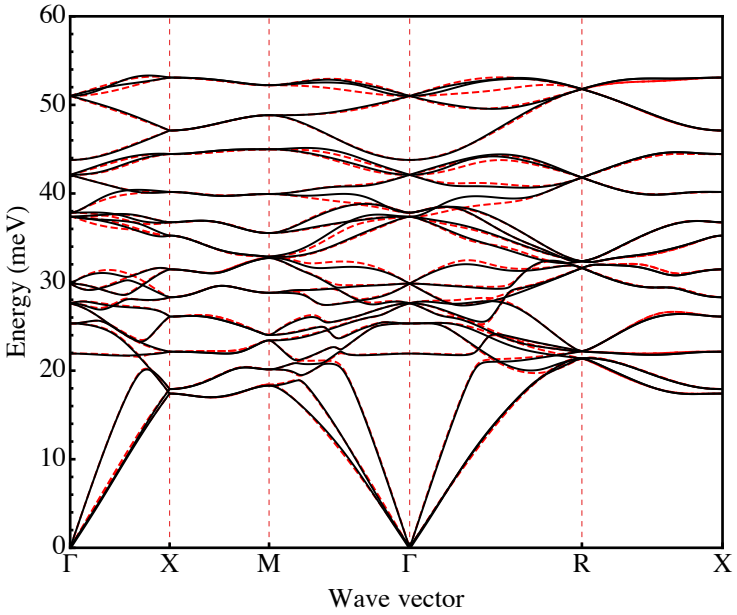

Figure 6.3: Comparison between the phonon dispersion of CoSi obtained using DFPT with a 2×2×2 (red dashed lines) and a 4×4×4 (black lines) **q**-mesh respectively implemented in Quantum Espresso.

for the exchange-correlation (xc) functional. [34] For the structure relaxation a plane wave basis with cutoff energy of 400 eV and a Monkhorst-Pack 10×10×10 **k**-point mesh were used. The energy convergence threshold was set to be 10^{-7} eV per primitive cell and forces were converged to be less than 10^{-3} eV/Å. The fully relaxed structure has a lattice constant of 4.433 Å, which is in good agreement with experimentally measured value of 4.450 Å [40].

We included interaction distances up to approximately 9 and 4 Å for second- and third-order interactions respectively. These cutoffs give rise to 1,442 symmetrically distinct elements out of 1,977 IFCs. Forces calculated from ten $4 \times 4 \times 4$ supercell structures with random atomic displacements ranging from 0.01 to 0.05 Å were used as training and validation sets. The total energy calculation of constructed supercells used only the Γ point with the same convergence threshold as that used in the structure relaxation. The optimal μ in Eq. (2.55) was selected from a list of values, in which the minimum value gives rise to overfitting while the maximum value leads to underfitting, based on random sub-sampling validation. We randomly selected

$\approx$ 80% of forces for IFCs training and the rest for validation. Multiple independent fittings of IFCs were carried out and the deviation of calculated κ_l is within 1%. Fig. 6.4 shows the comparison between our predicted forces and those directly calculated by VASP. Small relative errors of 1.47% verifies the utilized cutoffs for second and third-order interactions and indicates good accuracy of fitted IFCs as well. Fig. 6.5 shows the Frobenius norm of calculated IFCs with increasing interaction distances, which decrease to small value within the cutoffs. Fig. 6.6 shows the calculated phonon dispersion and DOS using fitted IFCs from CSLD. Our CSLD results are in good agreement with those obtained with DFPT in Quantum Espresso, as shown in Fig 6.3. The phonon dispersion obtained from CSLD shows slightly higher frequency for the same mode, probably due to the used different pseudopotentials from those in Quantum Espresso.

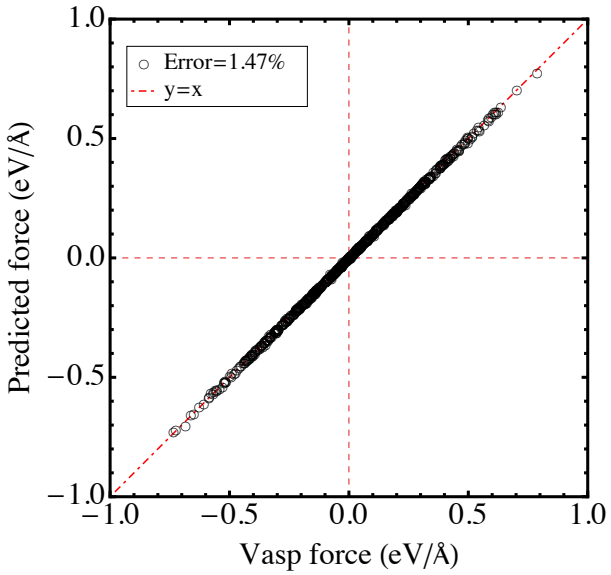

Figure 6.4: Comparison between forces predicted by the fitted IFCs and those directly calculated by VASP (black circles). The red dot dashed line is a diagonal, representing the exact fit. Relative error for the predicted forces is indicated in the legends.

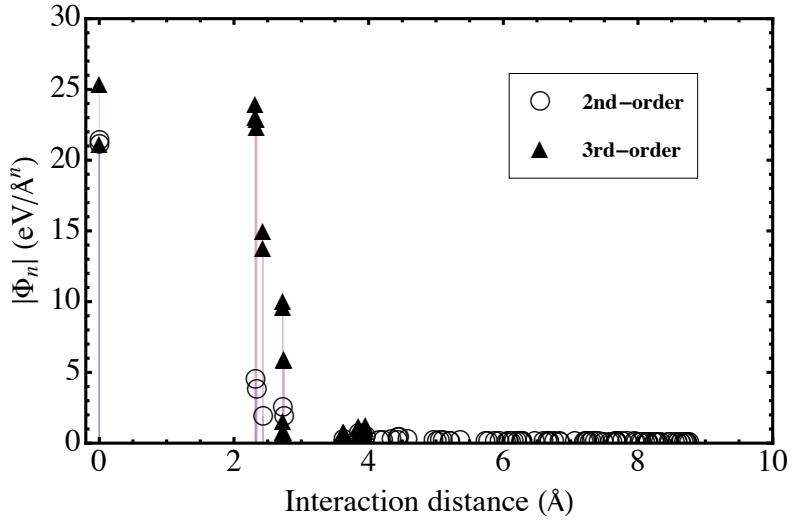

Figure 6.5: Frobenius norm of the fitted second- and third-order IFCs versus interaction distance, which is defined as the maximum distance between atoms.

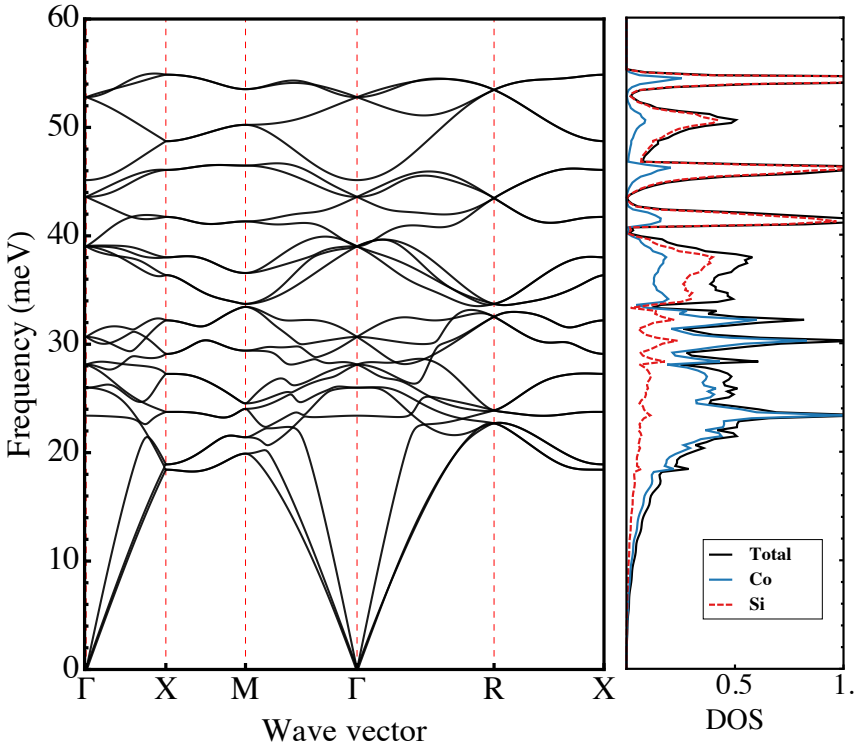

Figure 6.6: Calculated phonon dispersion and atom-projected density of states with the IFCs obtained from CSLD.

6.2.4 Transport Properties

For each temperature from 100 to 600 K, the corresponding Fermi level was determined by counting the total number of electrons using calculated DOS and Fermi-Dirac distribution as shown in Fig. 6.7. The DOS at 0 K was precisely calculated using tetrahedron method [42] with a 30×30×30 **k**-mesh. To solve the Boltzmann transport equation, the same **k**-mesh was used and the relative error of calculated Seebeck coefficient and electrical conductivity compared to a dense 40×40×40 **k**-mesh is within 1%. For lattice thermal conductivity calculation, we used a 16×16×16 **q**-mesh with $scalebroad = 0.1$ [33] and the relative error with respect to a dense 20×20×20 **q**-mesh is within 2%. Electron and phonon self-energies were calculated for the corresponding 1376 and 368 symmetrically distinctive electron and phonon wavevectors.

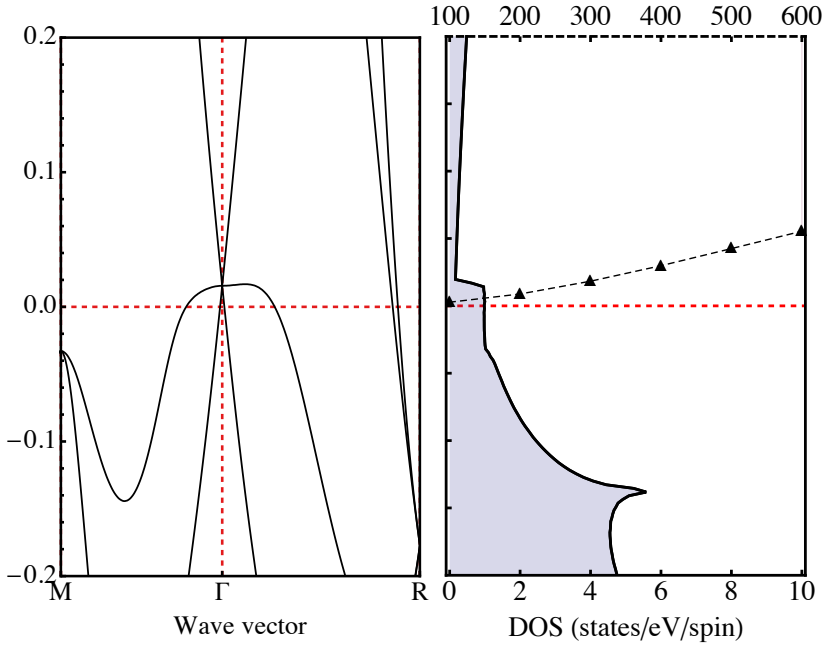

Figure 6.7: Detailed band structure and density of states around Fermi level. The horizontal red dashed line is the Fermi level at 0 K. The solid triangles shows the temperature-dependent Fermi levels from 100 to 600 K.

6.3 Results and Discussion

6.3.1 Electron Transport

With calculated Fermi level that conserves the total number of electrons at a given temperature and thereby evaluated electron lifetime, we calculated the Seebeck coefficient for pristine CoSi and compared our results with various experimental measurements [13, 11, 16, 18] in Fig. 6.8 (a). Our results show correct temperature dependence and exhibit large negative values of the Seebeck coefficient from 200 to 600 K. Our calculated Seebeck efficient follows closely with the experimental measurements from Sakai *et al.* [18], Skoug *et al.* [16] and Ren *et al.* [11] Compared with the Seebeck coefficient of about -90.8 μV K^{-1} at 300 K from Sun *et al.* [13], our calculated value of about -69.1 μV K^{-1} shows a roughly 24% underestimation. Considering various approximations involved in the theoretical model and possible extra scattering and distortion of band structure due to the presence of defects in experiments, our calculated Seebeck coefficient achieves good agreement with experiments. We further examine the accuracy of the calculated Seebeck coefficient by plotting its dependence on hole concentration in Fig. 6.8 (b). We reproduced a positive shift of Seebeck coefficient with increasing hole concentration. Moreover, our calculated critical hole concentration per formula unit at which the Seebeck coefficient changes sign is about 0.04, which is in excellent agreement with experimental measurements from Lue *et al.* [10] and Li *et al.* [12] The absolute value of the Seebeck coefficient again agrees very well with experiments at low hole concentration, however, shows large underestimation at high hole concentration. This is probably due to the fact that the norm conserving pseudopotentials predict a slightly lower-energy band pocket at M point compared with that obtained from PAW pseudopotential.

After verifying our calculated Seebeck coefficient, we move on to identify the main factor that gives rise to this exceptional thermoelectric property. For comparison, we also show the See-

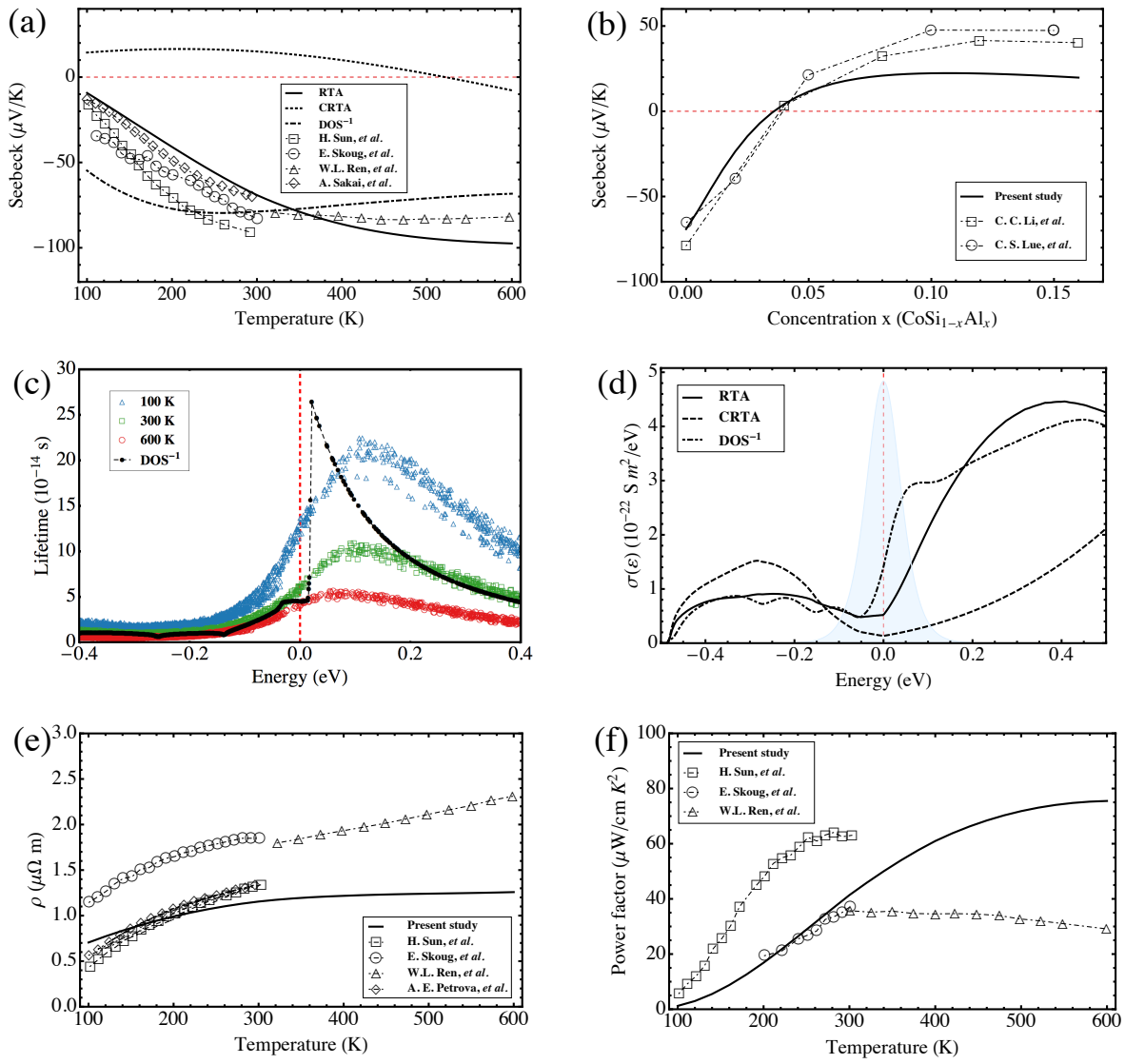

Figure 6.8: Calculated Seebeck coefficient, its dependence on hole concentration, electron lifetime, spectral conductivity, electrical conductivity, and power factor of CoSi. (a) Seebeck coefficient calculated under constant relaxation time approximation (CRTA), relaxation time approximation (RTA) and using electron lifetime that is inversely proportional to the electronic density of states (DOS), compared with experimental measurements [13, 11, 16, 18]. (b) The Seebeck coefficient at different concentrations of Al substitution on Si site at 300 K compared with experiments [10, 12]. (c) Electron lifetime near the Fermi level at 100, 300 and 600 K (Fermi levels are shifted to 0 eV). The black disk shows the lifetime that is inversely proportional to DOS. (d) Comparison between the spectral conductivity calculated under CRTA, RTA and using electron lifetime that is inversely proportional to DOS at 300 K. The light blue shaped area indicates the energy window restricted by the negative derivative of Fermi-Dirac distribution with respect to energy $(-\partial f(E_F)/\partial \varepsilon)$. Its absolute value is suppressed in order to show the whole peak. (e) Temperature dependence of electrical resistivity of CoSi compared with experiments [13, 11, 16, 14]. (f) Temperature dependence of thermoelectric power factor of CoSi compared with experimental measurements [13, 11, 16].

beck coefficient calculated with constant relaxation time and relaxation time that is inversely proportional to DOS in Fig. 6.8 (a). In contrast to the study by Pan *et al.* [17], we found CRTA in which the effect of DOS is fully included predicts a positive Seebeck coefficient at temperatures from 100 to 520 K. The small negative values at higher temperatures is due to the shift of Fermi level above the flat bands as shown in Fig. 6.7. This suggests that both the asymmetric band structure and abrupt change of DOS around Fermi level are not enough to explain the large negative Seebeck coefficient, thus energy dependence of lifetime should be taken into account. To partially eliminate the drastic approximation imposed by CRTA, we used the lifetime that is inversely proportional to DOS [43], which we refer as DOS^{-1} approximation and has been used to successfully explain the positive Seebeck in Lithium [44]. Though it leads to a Seebeck coefficient with large negative value, it shows significant overestimation and underestimation at low and high temperature ends respectively, which indicates an incorrect shape of energy dependence of lifetime. This discrepancy can be attributed to the fact that DOS^{-1} approximation only works properly when elastic acoustic scattering is dominating, while in CoSi there is a large number of optical branches interacting with electrons at high temperature [43]. Quantitive comparison between the calculated electron lifetime considering electron-phonon scattering at various temperatures and using DOS^{-1} approximation are shown in Fig. 6.8 (c). We observe strong energy dependence of electron lifetime, namely, there is a sharp increase of lifetime with increasing electronic band energy near the Fermi level. This feature can be partially found in the DOS^{-1} approximation, where the sharp increase of lifetime is due to the abrupt change of DOS. As can be seen in Eq. (2.36), a positive energy dependence of lifetime can lead to a negative Seebeck coefficients. Therefore, it can be inferred that in CoSi the energy-dependent lifetime dominates over the effect of DOS, thus giving rise to the large negative Seebeck coefficient. A more general quantity that determines both the absolute value and sign of the Seebeck coefficient is the spectral conductivity as defined in Eq. (2.35). We plot the spectral conductivity computed

under RTA, CRTA and DOS^{-1} approximation at 300 K in Fig. 6.8 (d). Under RTA the spectral conductivity at the vicinity of Fermi level is quite symmetric and the slightly larger value below the Fermi level within the filtering window restricted by $-\partial f(E_F)/\partial \varepsilon$ leads to a small positive Seebeck coefficient. Under RTA and DOS^{-1} approximation electron lifetime exhibits strong energy dependence, which leads to extremely asymmetric spectral conductivity, thus giving to the large negative Seebeck coefficient.

Fig. 6.8 (e) shows the calculated temperature-dependent electrical resistivity. In contrast to the Seebeck coefficient, there exists larger discrepancy among different experimental measurements. Sun *et al.* and Petroval *et al.* reported the lowest measured electrical resistivity so far [13, 14]. Since the electrical conductivity measured by Petrova *et al.* is from a single crystal CoSi, it indicates that the dominating electron scattering at elevated temperatures in their experiment is through electron-phonon interactions. Indeed, our computed electrical conductivity agrees very well with their measurements below 300 K, further confirming that the electron-phonon interaction is the main factor which leads to the finite electrical conductivity. Ren *et al.* and Skoug *et al.* reported significantly higher electrical conductivity, probably due to the extra scattering induced by various defects [11, 16]. Our calculated electrical conductivity exhibits unusual temperature dependence at temperatures higher than 300 K, i.e., the electrical resistivity remains nearly a constant that is independent of temperature. This is in contrast to a commonly accepted concept that increased population of phonons at higher temperatures should increase electron scattering rates and thus leads to higher electrical resistivity. Indeed, a further reduction of lifetime is observed with increased temperatures as shown in Fig. 6.8 (c). However, the shift of Fermi energy towards higher energy with increasing temperature partially cancels the effect of lifetime reduction. As can be seen in Fig. 6.8 (c), there is large difference between the electron lifetime at 100 and 300 K near the Fermi level, but the difference at 300 and 600 K is pretty small. Another factor is the increased Fermi velocity. From Fig. 6.2 we can see the averaged Fermi velocity increases

near the Γ and R points when the Fermi level moves above the flat band at temperatures higher than 300 K. The overall effect makes the electrical resistivity a nearly temperature-independent constant. This behavior has not been observed in previous experiments. This is possiblely due to the fact that various defects that can shift Fermi level and induce extra scattering. Verification of our results needs to measure the electrical resistivity using the high-quality single crystal CoSi. Calculated power factor is plotted and compared with experiments in Fig. 6.8 (f). Our theoretical results show a steady increase with increasing temperature and achieve a maximum value of about 75 μW cm^{-1} K^{-2}at 600 K. Sun *et al.* reported a overall larger power factor mostly due to the larger Seebeck coefficient [13]. Ren *et al.* showed a overall smaller power factor mostly due to the smaller electrical conductivity [11]. The best agreement is achieved when comparing to measurements from Skoug *et al.*. However, it is due to their larger Seebeck coefficient and smaller electrical conductivity [16]. Considering the fact that the results from different experiments scatter a lot, our computed temperature-dependent power factor agrees reasonably well with experiments.

6.3.2 Phonon Transport

The total thermal conductivity of pristine CoSi consists of electronic and lattice contributions as shown in Fig. 6.9 (a). Over the entire temperature range from 100 to 600 K, κ_l decreases monotonically from 40.9 to 6.1 W m^{-1} K^{-1} while κ_e increases from 3.8 to 12.5 W m^{-1} K^{-1}. This leads to a total thermal conductivity exhibiting sharp decrease with increasing temperature up to 200 K and very small further reduction at higher temperatures. Calculated κ_l agrees well with experimental reports from Sun *et al.* and Ren *et al.* [45, 11] in Fig. 6.9 (b). One interesting point is to identify the impact of EPI on κ_l. Compared with the calculated κ_l without considering EPI in Fig. 6.9 (b), EPI has significant impact on κ_l at low temperatures and reduce κ_l from 67.8 to 40.9 W m^{-1} K^{-1} at 100 K. At temperatures higher than 300 K, EPI almost has no impact on κ_l.

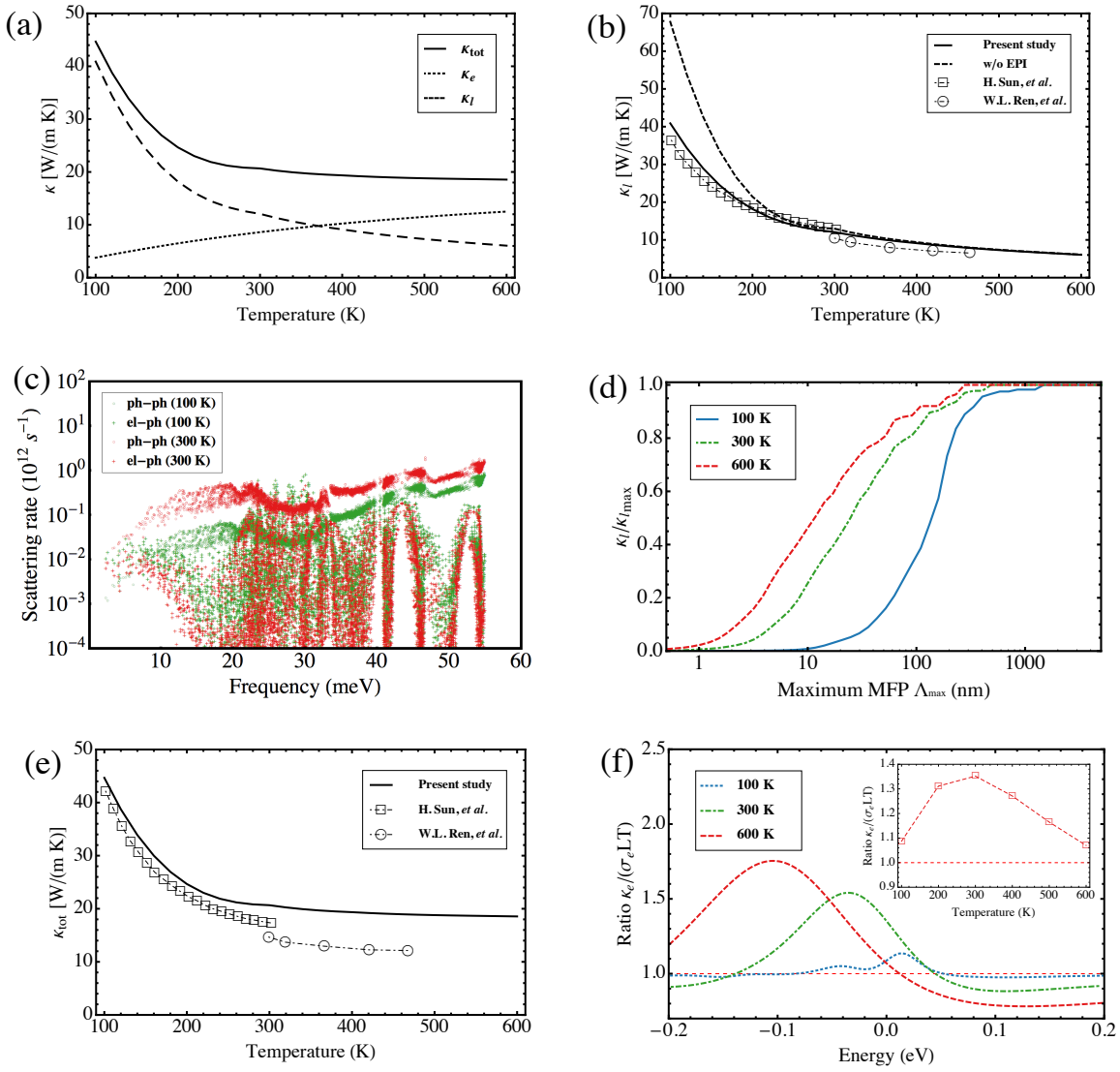

Figure 6.9: (a) Calculated electronic thermal conductivity κ_e, lattice thermal conductivity κ_l and total thermal conductivity κ_{tot}. (b) Calculated lattice thermal conductivity with and without electron-phonon interaction compared with experimental measurements [45, 11] (c) Comparison between scattering rates due to electron-phonon interaction (EPI) and phonon-phonon interaction (PPI) (d) Comparison between cumulative lattice thermal conductivities divided by their maximum values of 40.9, 12.6 and 6.1 W m^{-1} K^{-1} at 100, 300 and 600 K. (e) Calculated total thermal conductivity compared with experimental measurements [13, 11]. (f) The ratio between calculated electronic thermal conductivity and that estimated based on Wiedemann-Franz law using the Lorenz number of 2.44×10^{-8} W Ω K^{-2} at 100, 300 and 600 K as a function of chemical potential. The inset shows the temperature dependence of the ratio for pristine CoSi.

This can be understood from the plotted phonon scattering rates due to EPI and PPI respectively in Fig. 6.9 (c). The phonon scattering rates due to EPI have weak dependence on temperature, which can be seen from the formulation of phonon self energy in Eq. (2.33). While the scattering rates due to PPI increase considerably with increased temperatures from 100 to 300 K, mainly attributable to the increased phonon population. At low temperature both EPI and PPI scatter phonon modes significantly while at high temperature PPI dominates over EPI. The dependence on maximum mean free path of κ_l at 100, 300 and 600 K is shown in Fig. 6.9 (d). We see temperature alters the distribution of κ_l over mean free path significantly. At high temperatures the contribution to κ_l due to phonon modes with short mean free paths increases, which is detrimental to κ_l reduction based on restricting maximum mean free path. For example, κ_l at 600 K can only be reduced by 50% to about 3 W m^{-1} K^{-1} with maximum mean free path of 10 nm, which is still too high to achieve $ZT > 1.0$. In addition, 10 nm is pretty short and the impact on the Seebeck coefficient and electrical conductivity should be further examined. Fig. 6.9 (e) shows the calculated total thermal conductivity in comparison with experiments [45, 11]. Our result agrees well with the reports from Sun *et al.* due to the agreement in electrical conductivity [13], while exhibits systematic overestimation compared with the reports from Ren *et al.* [11], mainly due to the significantly higher electrical resistivity measured in their experiments. We also examine the validity of Wiedemann-Franz law in Fig. 6.9 (f). With increased temperature, the calculated Lorenz number shows a both enhanced and broadened peak around Fermi level. The maximum enhancement of the Lorenz number can be as large as 70% compared with regularly used constant of 2.44×10^{-8} W Ω K^{-2}. However, the shift of Fermi level partially eliminates this effect and the overall Lorenz number shows a peak value of about 35% enhancement at 300 K and 10% enhancement at both low temperature (100 K) and high temperature ends (600 K). This calls for a further validation of the Lorenz constant used in experiments. This also can be used to explain the overestimation of κ_l from experiments in Fig. 6.9 (b).

6.3.3 Optimization

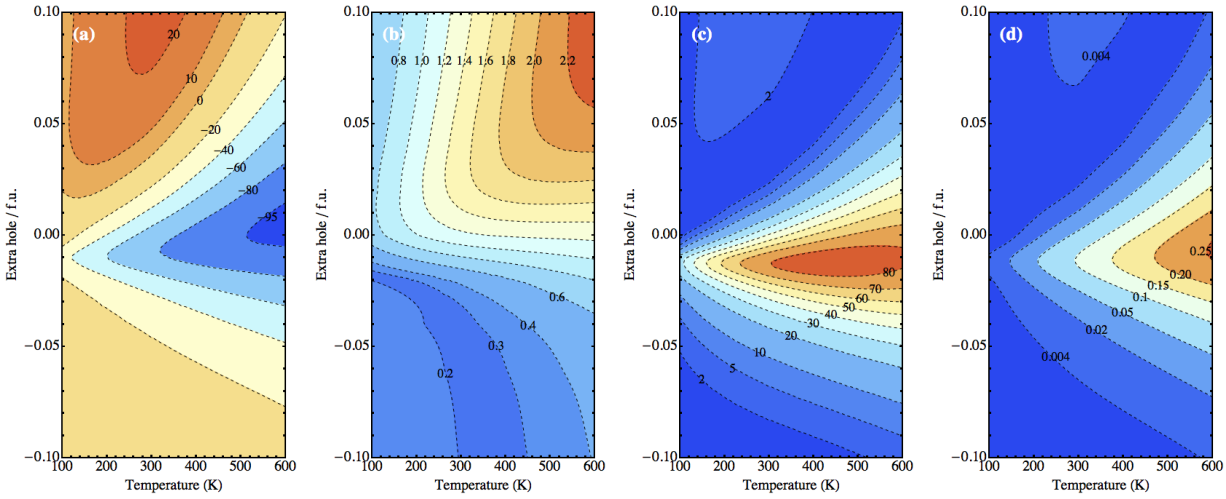

Figure 6.10: Contour plots of the calculated (a) Seebeck coefficient, (b) electrical resistivity, (c) thermoelectric power factor and (d) ZT as a function of temperature and extra hole per formula unit ($CoSi_{1-x}Al_x$). The negative value of x corresponds to extra electron per formula unit. The unit of the Seebeck coefficient, electrical conductivity and thermoelectric power factor are given in μV K^{-1}, $\mu\Omega$ m and μW cm^{-1} K^{-2} respectively.

Fig. 6.10 shows a comprehensive investigation of temperature and doping dependence of the Seebeck coefficient, electrical resistivity, thermoelectric power factor and ZT. Fig. 6.10 (a) shows the dependence of the Seebeck coefficient on temperature and hole concentration. We see the optimal Seebeck with large negative value can be achieved with slight electron doping at low temperatures and can be readily found in pristine CoSi at high temperatures. The increase of temperature tends to enhance the Seebeck coefficient. Hole doping has an effect to shift the Seebeck coefficient towards a positive value as already demonstrated in Fig. 6.8 (b). Fig. 6.10 (b) shows the dependence of electrical resistivity on temperature and hole concentration. The electrical resistivity with either electron or hole doping increases with increasing temperature, primarily due to the enhanced electron scattering by phonon. However, the shift of Fermi level due to temperature broadening of energy distribution leads to an almost constant electrical resistivity at high temperature in pristine CoSi. At a given temperature, electron doping reduces while hole

doping increases electrical receptivity. Detailed analysis of hole doping below 500 K shows the electrical resistivity first increases then slightly decreases, which exhibits the same behavior found by Li *et al.* [12]. The calculated doping and temperature-dependent power factor are plotted in Fig. 6.10 (c). It shows that a large power factor above 60 μW cm^{-1} K^{-2} can be achieved at temperature as low as 200 K with slight electron doping (≈ 0.01/f.u.). The power factor can be further enhanced to reach a value as high as 80 μW cm^{-1} K^{-2} at temperatures higher than 300 K. On the other hand, the hole doping decreases the power factor and heavy hole doping with the positive Seebeck coefficient leads to a rather small power factor due to high electrical resistivity and small absolute value of the Seebeck coefficient. Note that our optimal power factor obtained with slight electron doping is in contrast to the reports by Sun *et al.* that all the n-type-doped samples show reduced power factor near room temperature. This could be due to the off-stoichiomectry of their prepared samples, which also can be inferred from the better agreement between their measured Seebeck coefficient and our calculated Seebeck coefficient with slight electron doping. Fig. 6.10 (d) shows the resulting doping and temperature-dependent ZT. Optimal ZTs of 0.11 and 0.25 can be achieved at 300 and 600 K respectively with slight electron doping.

6.4 Conclusions

In summary, we have carried out a fully first-principles study of doping and temperature-dependent thermoelectric properties of B20-type CoSi by explicitly taking into account electron-phonon and phonon-phonon interactions. For the electron transport, we found the large negative Seebeck coefficient of pristine CoSi is mostly due to the strong energy dependence of carrier lifetime. Neither the abrupt change of density of states nor the asymmetric band structure directly gives rise to the large negative Seebeck coefficient. Our calculated Seebeck coefficient and

electrical resistivity show good agreement with experiments at various temperatures and doping concentrations. The presence of nearly constant electrical resistivity for pristine CoSi at temperatures from 300 to 600 K can be attributed to the shift of Fermi level due to the temperature broadening of energy distribution, which should be further examined in the future experiments. For the phonon transport, we found both electron-phonon and phonon-phonon interactions contribute significantly to phonon scattering at temperatures lower than 200 K. At 100 K electron scatters phonon considerably and reduces the lattice thermal conductivity from 67.8 to 40.9 W m^{-1} K^{-1}. At temperatures higher than 300 K, phonon-phonon interaction dominates over electron-phonon interaction. Our calculated lattice and total thermal conductivity agree well with experiments. Based on the optimized power factor, we predict that the maximum ZT at 300 and 600 K is about 0.11 and 0.25 respectively without further reducing the total thermal conductivity. Our study shows the importance to consider electron-phonon interaction in evaluating accurate energy dependent carrier lifetime in order to explain, identify and optimize thermoelectric properties through first-principles calculations.

6.5 Acknowledgement

This work was supported by the U.S. Department of Energy, Office of Science, Basic Energy Sciences, under Grant No. DE-FG02-07ER46433 and used computing resources at the National Energy Research Scientific Computing Center (NERSC), which is supported by the U.S. DOE under contract DE-AC02-05CH11231.

References

[1] Xu Lu, Donald T. Morelli, Yi Xia, Fei Zhou, Vidvuds Ozolins, Hang Chi, Xiaoyuan Zhou, and Ctirad Uher. High performance thermoelectricity in earth-abundant compounds based on natural mineral tetrahedrites. *Advanced Energy Materials*, 3(3):342–348, 2013.

[2] Bed Poudel, Qing Hao, Yi Ma, Yucheng Lan, Austin Minnich, Bo Yu, Xiao Yan, Dezhi Wang, Andrew Muto, Daryoosh Vashaee, Xiaoyuan Chen, Junming Liu, Mildred S. Dresselhaus, Gang Chen, and Zhifeng Ren. High-thermoelectric performance of nanostructured bismuth antimony telluride bulk alloys. *Science*, 320(5876):634–638, 2008.

[3] G. A. Slack. *Solid State Physics*, volume 34. Academic Press, New York, 1979.

[4] G. Jeffrey Snyder and Eric S. Toberer. Complex thermoelectric materials. *Nat. Mater.*, 7(2):105–114, 02 2008.

[5] Hideaki Kato, Masaaki Kato, Yoichi Nishino, Uichiro Mizutani, and Shigeru Asano. Effect of silicon substitution on thermoelectric properties of heusler-type Fe_2VAl alloy. *Journal of the Japan Institute of Metals*, 65(7):652–656, 2001.

[6] S. Asanabe, D. Shinoda, and Y. Sasaki. Semimetallic properties of $Co_{1-x}Fe_xSi$ solid solutions. *Phys. Rev.*, 134:A774–A779, May 1964.

[7] Yanzhong Pei, Xiaoya Shi, Aaron LaLonde, Heng Wang, Lidong Chen, and G. Jeffrey Snyder. Convergence of electronic bands for high performance bulk thermoelectrics. *Nature*, 473(7345):66–69, 05 2011.

[8] Osamu Yamashita and Sunao Sugihara. High-performance bismuth-telluride compounds with highly stable thermoelectric figure of merit. *Journal of Materials Science*, 40(24):6439–6444, 2005.

[9] Li-Dong Zhao, Shih-Han Lo, Yongsheng Zhang, Hui Sun, Gangjian Tan, Ctirad Uher, C. Wolverton, Vinayak P. Dravid, and Mercouri G. Kanatzidis. Ultralow thermal conductivity and high thermoelectric figure of merit in SnSe crystals. *Nature*, 508(7496):373–377, 04 2014.

[10] C. S. Lue, Y.-K. Kuo, C. L. Huang, and W. J. Lai. Hole-doping effect on the thermoelectric properties and electronic structure of CoSi. *Phys. Rev. B*, 69:125111, Mar 2004.

[11] W.L. Ren, C.C. Li, L.T. Zhang, K. Ito, and J.S. Wu. Effects of Ge and B substitution on thermoelectric properties of CoSi. *Journal of Alloys and Compounds*, 392(1–2):50 – 54, 2005.

[12] C. C. Li, W. L. Ren, L. T. Zhang, K. Ito, and J. S. Wu. Effects of al doping on the thermoelectric performance of CoSi single crystal. *Journal of Applied Physics*, 98(6), 2005.

[13] Hui Sun, Xu Lu, and Donald T. Morelli. Effects of Ni, Pd, and Pt substitutions on thermoelectric properties of CoSi alloys. *Journal of Electronic Materials*, 42(7):1352–1357, 2013.

[14] Alla E. Petrova, Vladimir N. Krasnorussky, Anatoly A. Shikov, William M. Yuhasz, Thomas A. Lograsso, Jason C. Lashley, and Sergei M. Stishov. Elastic, thermodynamic, and electronic properties of MnSi, FeSi, and CoSi. *Phys. Rev. B*, 82:155124, Oct 2010.

[15] Y. K. Kuo, K. M. Sivakumar, S. J. Huang, and C. S. Lue. Thermoelectric properties of the $CoSi_{1-x}Ge_x$ alloys. *Journal of Applied Physics*, 98(12), 2005.

[16] E. Skoug, C. Zhou, Y. Pei, and D. T. Morelli. High thermoelectric power factor in alloys based on cosi. *Applied Physics Letters*, 94(2), 2009.

[17] Z. J. Pan, L. T. Zhang, and J. S. Wu. Electronic structure and transport properties of doped CoSi single crystal. *Journal of Applied Physics*, 101(3), 2007.

[18] A. Sakai, S. Yotsuhashi, H. Adachi, F. Ishii, Y. Onose, Y. Tomioka, N. Nagaosa, and Y. Tokura. Filling dependence of thermoelectric power in transition-metal monosilicides. In *Thermoelectrics, 2007. ICT 2007. 26th International Conference on*, pages 256–259, June 2007.

[19] N. Kanazawa, Y. Onose, Y. Shiomi, S. Ishiwata, and Y. Tokura. Band-filling dependence of thermoelectric properties in b20-type CoGe. *Applied Physics Letters*, 100(9), 2012.

[20] Paolo Giannozzi, Stefano Baroni, Nicola Bonini, Matteo Calandra, Roberto Car, Carlo Cavazzoni, Davide Ceresoli, Guido L Chiarotti, Matteo Cococcioni, Ismaila Dabo, Andrea Dal Corso, Stefano de Gironcoli, Stefano Fabris, Guido Fratesi, Ralph Gebauer, Uwe Gerstmann, Christos Gougoussis, Anton Kokalj, Michele Lazzeri, Layla Martin-Samos, Nicola Marzari, Francesco Mauri, Riccardo Mazzarello, Stefano Paolini, Alfredo Pasquarello, Lorenzo Paulatto, Carlo Sbraccia, Sandro Scandolo, Gabriele Sclauzero, Ari P Seitsonen, Alexander Smogunov, Paolo Umari, and Renata M Wentzcovitch. Quantum espresso: a modular and open-source software project for quantum simulations of materials. *J. Phys.: Condens. Matter*, 21(39):395502, 2009.

[21] Georg K.H. Madsen and David J. Singh. Boltztrap. a code for calculating band-structure dependent quantities. *Comput. Phys. Commun.*, 175(1):67 – 71, 2006.

[22] Jesse Noffsinger, Feliciano Giustino, Brad D. Malone, Cheol-Hwan Park, Steven G. Louie, and Marvin L. Cohen. EPW: A program for calculating the electron–phonon coupling using maximally localized wannier functions. *Comput. Phys. Commun.*, 181(12):2140 – 2148, 2010.

[23] Feliciano Giustino, Marvin L. Cohen, and Steven G. Louie. Electron-phonon interaction using wannier functions. *Phys. Rev. B*, 76:165108, Oct 2007.

[24] Nicola Marzari and David Vanderbilt. Maximally localized generalized wannier functions for composite energy bands. *Phys. Rev. B*, 56:12847–12865, Nov 1997.

[25] Ivo Souza, Nicola Marzari, and David Vanderbilt. Maximally localized wannier functions for entangled energy bands. *Phys. Rev. B*, 65:035109, Dec 2001.

[26] Nicola Marzari, Arash A. Mostofi, Jonathan R. Yates, Ivo Souza, and David Vanderbilt. Maximally localized wannier functions: Theory and applications. *Rev. Mod. Phys.*, 84:1419–1475, Oct 2012.

[27] Arash A. Mostofi, Jonathan R. Yates, Young-Su Lee, Ivo Souza, David Vanderbilt, and Nicola Marzari. wannier90: A tool for obtaining maximally-localised wannier functions. *Computer Physics Communications*, 178(9):685 – 699, 2008.

[28] Fei Zhou, Weston Nielson, Yi Xia, and Vidvuds Ozoliņš. Lattice anharmonicity and thermal conductivity from compressive sensing of first-principles calculations. *Phys. Rev. Lett.*, 113:185501, Oct 2014.

[29] G. Kresse and J. Hafner. *Ab initio* molecular dynamics for liquid metals. *Phys. Rev. B*, 47:558–561, Jan 1993.

[30] G. Kresse and J. Hafner. *Ab initio* molecular-dynamics simulation of the liquid-metal–amorphous-semiconductor transition in germanium. *Phys. Rev. B*, 49:14251–14269, May 1994.

[31] G. Kresse and J. Furthmüller. *Comput. Mater. Sci.*, 6:15–50, 1996.

[32] G. Kresse and J. Furthmüller. Efficient iterative schemes for *ab initio* total-energy calculations using a plane-wave basis set. *Phys. Rev. B*, 54:11169–11186, Oct 1996.

[33] Wu Li, Jesús Carrete, Nebil A. Katcho, and Natalio Mingo. Shengbte: A solver of the boltzmann transport equation for phonons. *Computer Physics Communications*, 185(6):1747 – 1758, 2014.

[34] P. Hohenberg and W. Kohn. Inhomogeneous electron gas. *Phys. Rev.*, 136:B864–B871, Nov 1964.

[35] N. Troullier and José Luís Martins. Efficient pseudopotentials for plane-wave calculations. *Phys. Rev. B*, 43:1993–2006, Jan 1991.

[36] John P. Perdew, Kieron Burke, and Matthias Ernzerhof. Generalized gradient approximation made simple. *Phys. Rev. Lett.*, 77:3865–3868, Oct 1996.

[37] W. Kohn and L. J. Sham. Self-consistent equations including exchange and correlation effects. *Phys. Rev.*, 140:A1133–A1138, Nov 1965.

[38] John P. Perdew, Kieron Burke, and Yue Wang. Generalized gradient approximation for the exchange-correlation hole of a many-electron system. *Phys. Rev. B*, 54:16533–16539, Dec 1996.

[39] M. Methfessel and A. T. Paxton. High-precision sampling for brillouin-zone integration in metals. *Phys. Rev. B*, 40:3616–3621, Aug 1989.

[40] P. Demchenko, J. Konczyk, O. Bodak, R. Matvijishyn, L. Muratova, and B. Marciniak. Single crystal investigation of the new phase $Er_{0.85}Co_{4.31}Si$ and of CoSi. *Chem. Met. Alloys*, 1:50–53, 2008.

[41] P. E. Blöchl. Projector augmented-wave method. *Phys. Rev. B*, 50:17953–17979, Dec 1994.

[42] Peter E. Blöchl, O. Jepsen, and O. K. Andersen. Improved tetrahedron method for brillouin-zone integrations. *Phys. Rev. B*, 49:16223–16233, Jun 1994.

[43] J.M. Ziman. *Electrons and Phonons: The Theory of Transport Phenomena in Solids*. International series of monographs on physics. OUP Oxford, 1960.

[44] Bin Xu and Matthieu J. Verstraete. First principles explanation of the positive seebeck coefficient of lithium. *Phys. Rev. Lett.*, 112:196603, May 2014.

[45] Hui Sun and Donald T. Morelli. Thermoelectric properties of $Co_{1-x}Rh_xSi_{0.98}B_{0.02}$ alloys. *Journal of Electronic Materials*, 41(6):1125–1129, 2012.

CHAPTER 7

First-Principles Study of Earth-Abundant Tetrahedrite $Cu_{12}Sb_4S_{13}$

7.1 Introduction

With a more complete understanding of electronic and thermal transport in semiconductor, better control over synthesis methods, and the successful application of nanotechnology, new materials systems with ZT higher than unity have been discovered and developed, including thin film superlattices, filled skutterudites and bulk nanostructure chalcogenides [1, 2, 3]. Unfortunately, complex and costly synthesis procedures prevent them from large-scale application, thus requiring the discovery of new thermoelectric materials which are inexpensive, environment-friendly, easy to synthesize and comprise of earth-abundant elements. Direct reduction of lattice thermal conductivity is one very successful route to improve ZT. More interesting from the thermoelectric point of view are crystalline solids which exhibit very low lattice thermal conductivity due to strong intrinsic phonon scattering. Examples are cage structures containing rattling atoms like skutterudites and clathrates [4], crystalline rocksalt structure I-V-VI_2 compounds (e.g. $AgSbTe_2$) [5] and Sb-containing ternary semiconductors that have Sb lone s^2 pair electrons [6]. Our recently discovered $Cu_{12}Sb_4S_{14}$, the base composition of a large family of natural minerals called tetrahedrites, exhibits intrinsically very low lattice thermal conductivity which gives birth to high $ZT \approx 0.9$, comparable to the state-of-the-art thermoelectric materials in the range of 600-700 K.

In addition, a comparable value of ZT can be achieved in a randomly chosen natural tetrahedrite mineral specimen, with composition adjusted by a simple and quick process. In this chapter, we present a first-principles study of the structural, electronic and lattice vibrational properties to investigate the doping effects of transition metals and the origin of intrinsically low lattice thermal conductivity. Most content has been published in Ref. [7, 8, 9, 10]

7.2 Computational Details

First-principles calculations based on density-functional theory (DFT) [11] with the projector-augmented wave (PAW) [12] method implemented in the Vienna *Ab initio* simulation package (VASP) [13, 14, 15, 16] were performed. The tetrahedrite structure obtained from ICSD is fully relaxed using the generalized gradient approximations Perdew-Becke-Ernzerhof (PBE) exchange-correlation functional [17, 18] with a Monkhorst-Pack **k**-point mesh of $4 \times 4 \times 4$ and a plane wave cutoff energy of 450 eV. The adopted convergence thresholds are 1.0×10^{-5} eV for the total energy of the primitive cell and 10^{-2} eV Å^{-1} for the forces on each atom. Our calculated equilibrium lattice constant is 10.403 Å, which shows a slight overestimation compared with the experimental value of 10.364 Å. And this is common for the PBE functional. Ternary phase diagram and various defect formation energies were calculated under the same setting. A Monkhorst-Pack **k**-point mesh of $10 \times 10 \times 10$ and the same energy cutoff were used to obtain the electronic density of states. The corresponding electronic band structure was calculated along the high-symmetry lines in the reciprocal space of body-centered cubic structure. We also performed calculation using LDA+U [19] method with U values of 4 and 8 eV and the Heyd-Scuseria-Ernzerhof (HSE06) [20, 21, 22] range-separated hybrid exchange functional to verify the electronic band structure obtained from the PBE functional. Interatomic force constants up to sixth-order were obtained via CSLD using constructed 464-atom supercells with configura-

tions obtained from *ab initio* molecular dynamics trajectories plus random small displacements (≈ 0.1 Å).

7.3 Results and Discussion

7.3.1 Structure, Stability and Defects

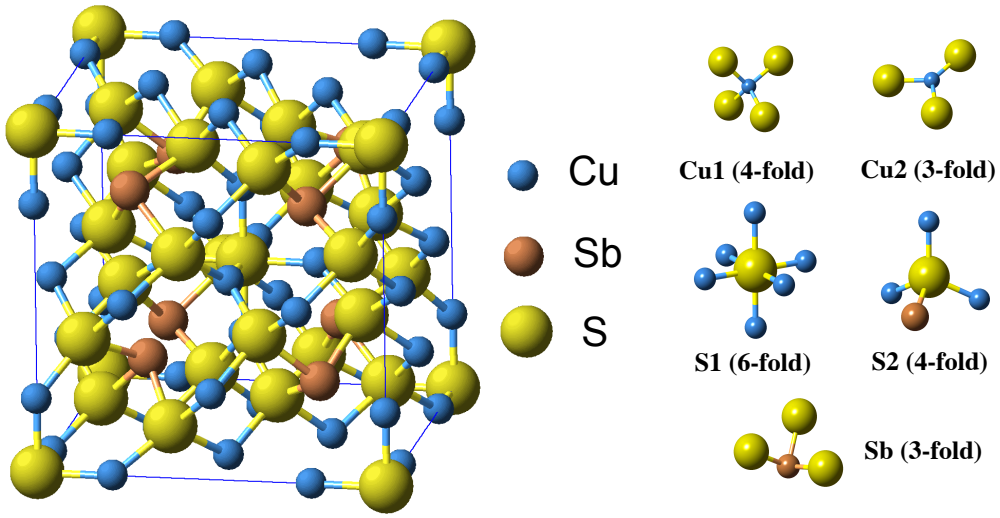

Figure 7.1: Crystal structure of tetrahedrite ($Cu_{12}Sb_4S_{13}$)

$Cu_{12}Sb_4S_{13}$ has a complex crystal structure based on the sphalerite arrangement. It has a total number of 29 atoms in a stoichiometric primitive cell of $I\bar{4}3m$ symmetry [23]. The structure is shown in Fig. 7.1. There are two kinds of Cu atoms. Six of the twelve Cu atoms denoted as Cu(2) occupy trigonal planar 12e sites and the other six Cu atoms denoted as Cu(1) distribute on tetrahedral 12d sites. There are also two kinds of sulfur atoms. Twelve out of thirteen sulfur atoms denoted as S(2) occupy tetrahedral sites bonded to one Cu(1) atom, two Cu(2) atoms and one antimony atom while the other sulfur atom denoted as S(1) occupies an octahedral site bonded to six Cu(2) atoms. The Sb atoms also occupy tetrahedral sites but are only bonded to three S(2) atoms. In terms of a simple crystal-chemical formula, it is expected that monovalent

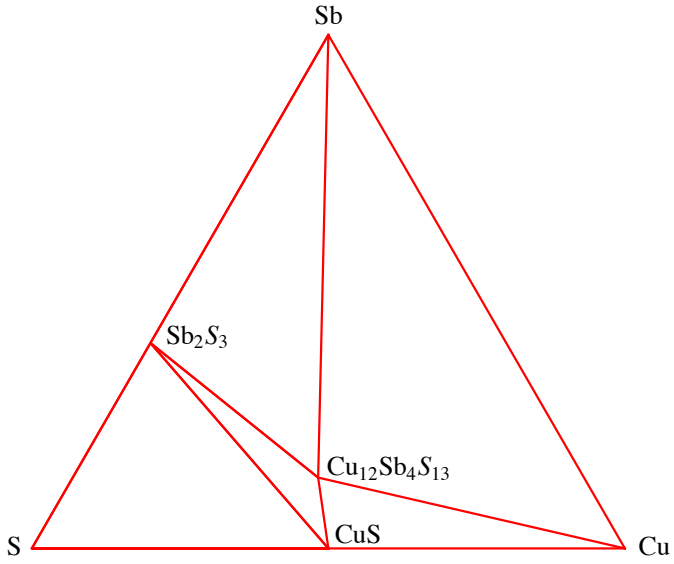

Figure 7.2: Ternary phase diagram of $Cu_{12}Sb_4S_{13}$ at T=0 K

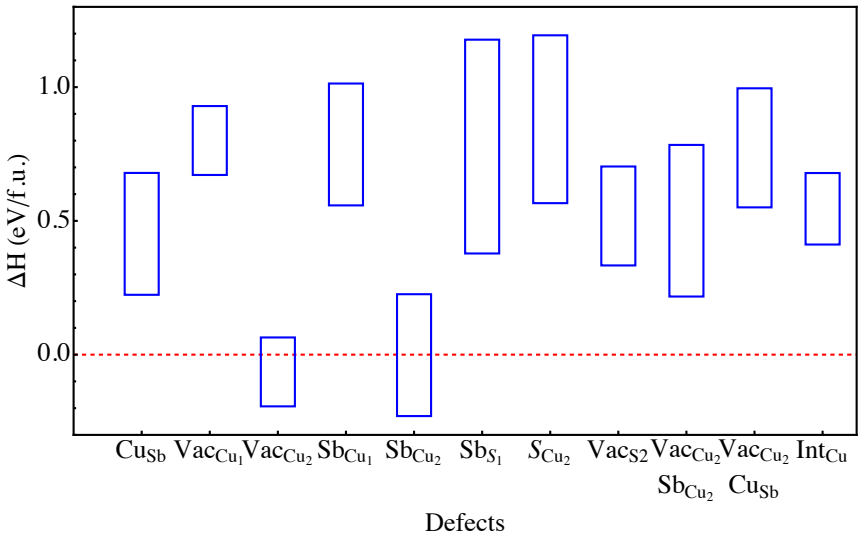

Figure 7.3: Defects formation energies in $Cu_{12}Sb_4S_{13}$ system at T=0 K

Cu^+ ions occupy four out of six tetrahedral sites, while the other two are occupied by Cu^{2+} ions; the trigonal planar 12e sites are occupied by monovalent Cu^+ [24].

Structure stability was verified against known stable elemental and binary phases: Cu, Cu_3SbS_4, Cu_7S_4, CuS, $CuSbS_2$, S, Sb, Sb_2S_3 and CuS_2. It was found that $Cu_{12}Sb_4S_{13}$ lies at the bottom of the convex hull at 0 K as shown in Fig. 7.2. We further constructed single- and dia-defects in a supercell composed of two formula units and calculated the corresponding formation energies using chemical potentials determined by four different set of stable phases near the $Cu_{12}Sb_4S_{13}$ phase as shown in Fig. 7.3. It can be seen that vacancy and Sb substitution on Cu trigonal planar 12e sites have both negative and positive formation energies extending from approximately -0.25 eV to 0.25 eV, which is due to the various phase equilibrium conditions. These negative values of formation energies for these two defects indicates that they are possible to form at low temperatures and shows the instability of Cu(2) sites. We will see these easily formed defects, together with the lattice distortion induced by unstable phonon modes, could lead to the variable-range hopping-type conduction at low temperatures observed in experimental measurements.

7.3.2 Band Structure and Density of States

DFT band structure calculations in Fig. 7.4 show that $Cu_{12}Sb_4S_{13}$ is a metal where the Fermi level falls near a sharp peak in the density of states at the top of the valence band, and a semi-conducting gap of about 1.2 eV separates the valence bands from the conduction bands. The valence bands are formed by hybridizing sulfur 3p and copper 3d orbitals. From the atom orbital-decomposed density of states in Fig. 7.5, we see that the main feature relevant for the thermoelectric properties is the existence of a valence band complex between -6 and 0 eV that is formed by hybridizing S p and Cu d orbitals. The valence band complex is split by a mini-gap of almost 1.0 eV separating 39 p-d hybridized bands of majority S p character and 60 hybridized bands of majority Cu d character. Together with the low-energy bands of S and Sb, this adds up

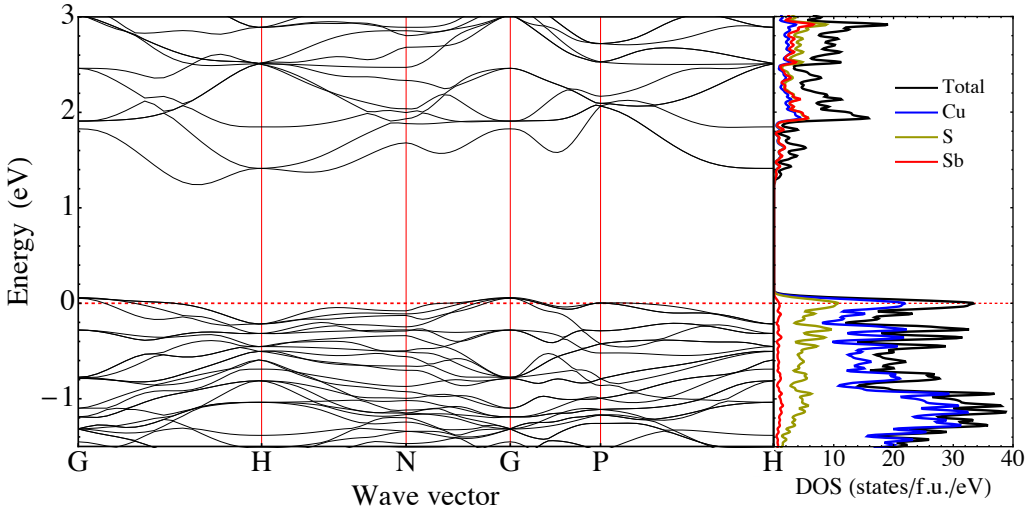

Figure 7.4: Electronic band structure and atom-projected density of states for $Cu_{12}Sb_4S_{13}$. Fermi level is marked by a dashed line

to a total of 116 spin-degenerate bands holding 330 electrons, resulting in two free hole states per formula unit of the pristine compound. It indicates, contrary to the naive valence counting argument given above, all copper ions are found to be in the monovalent Cu^+ states. We have verified that these conclusions remain qualitatively unchanged irrespective of the employed exchange-correlation functional. Our results are further verified by experimental measurements of Hall coefficient. One discrepancy between our calculation and experiments is that the low temperature experimental resistivity shows semiconductor-like characteristics and it cannot be fit with a simple activated behavior; rather, the conductivity behavior is more consistent with a hopping-type mechanism. We propose that the hopping-type mechanism is mainly due to the presence of various defects and lattice distortion at low temperature, which essentially makes $Cu_{12}Sb_4S_{13}$ behavior like a dirty metal.

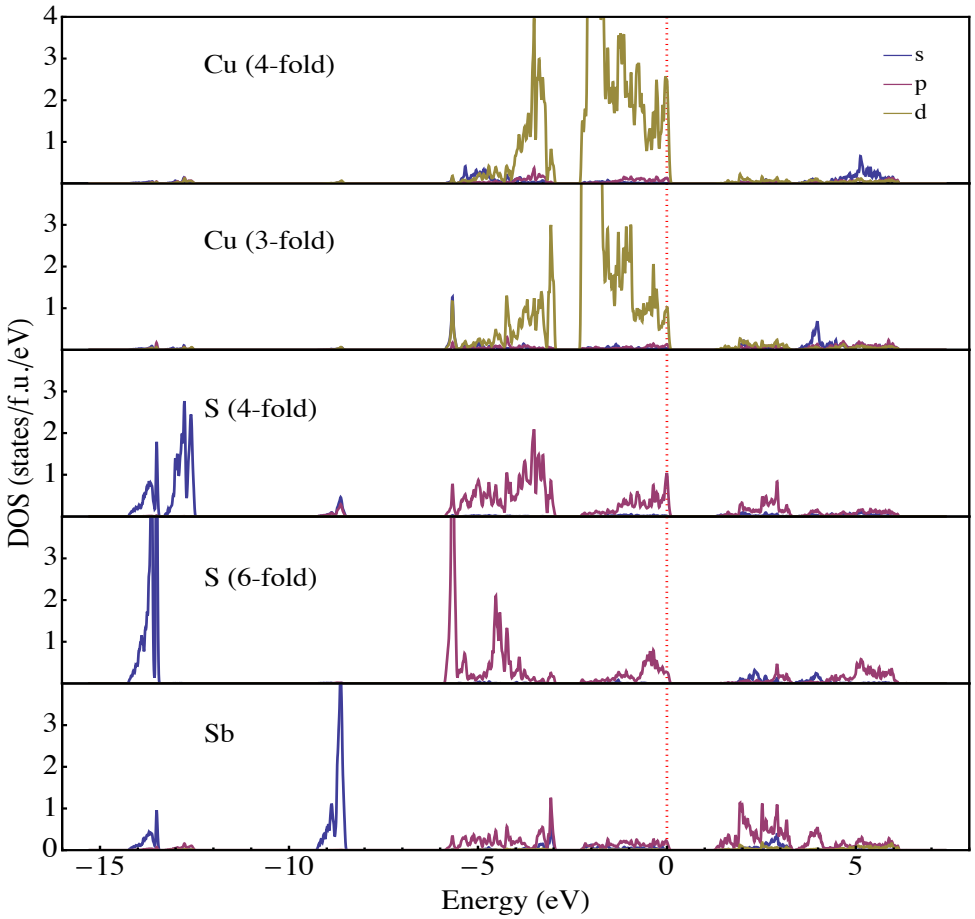

Figure 7.5: Orbital-decomposed density of states for $Cu_{12}Sb_4S_{13}$

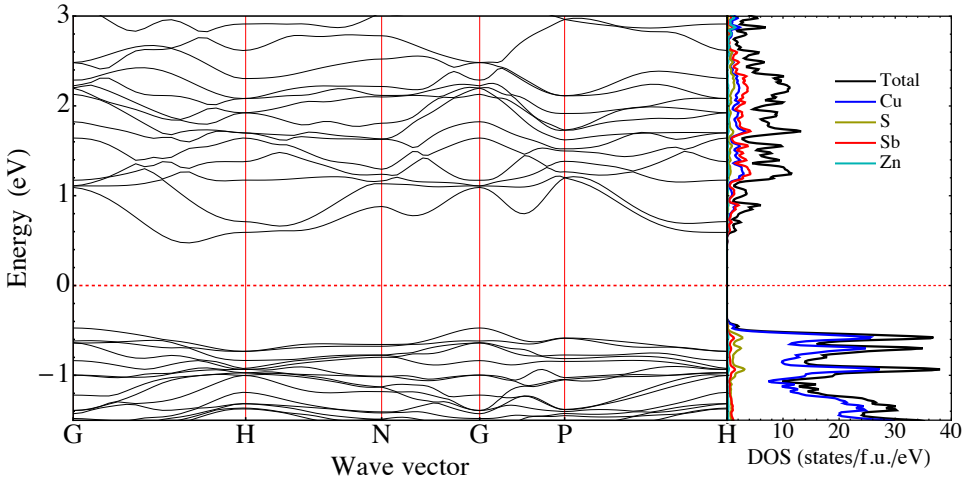

Figure 7.6: Electronic band structure and density of states for $Cu_{10}Zn_2Sb_4S_{13}$

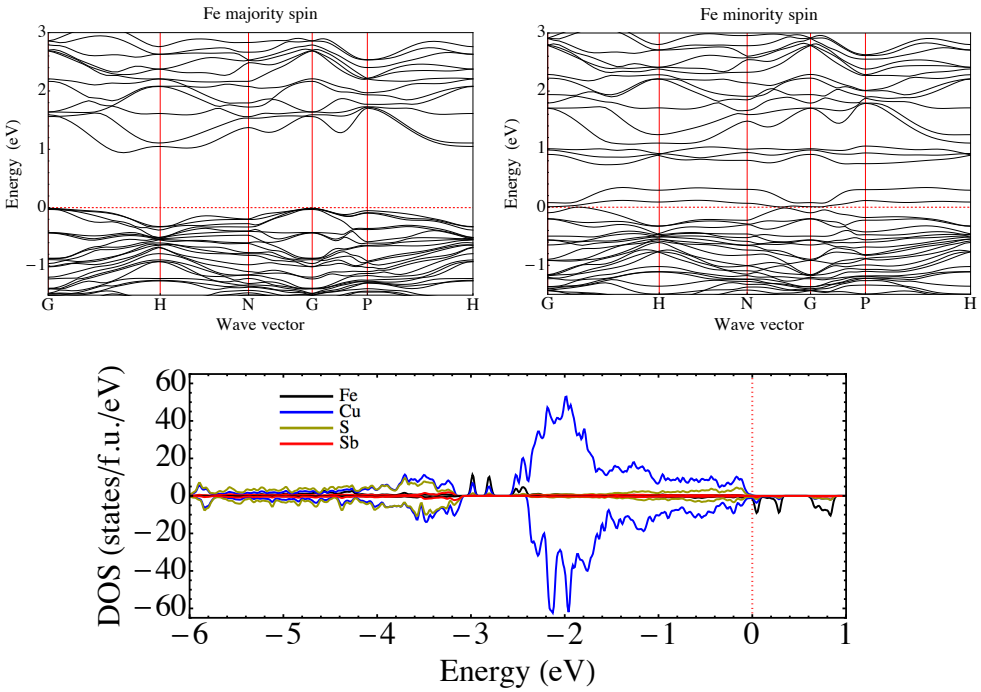

Figure 7.7: Electronic band structure and density of states for $Cu_{11}FeSb_4S_{13}$

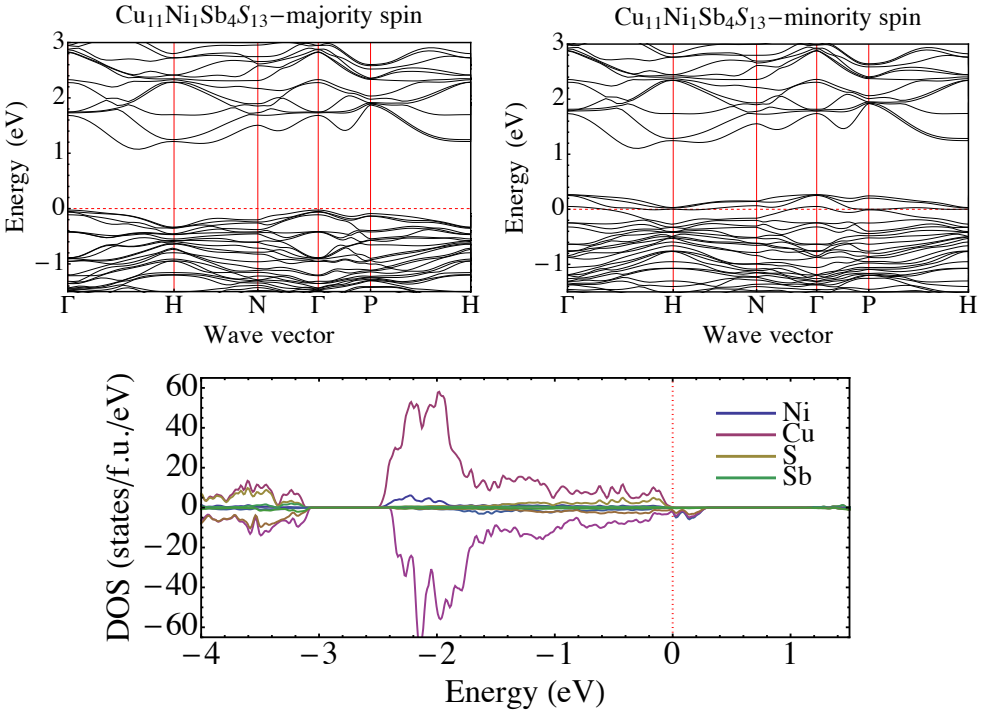

Figure 7.8: Electronic band structure and density of states for $Cu_{11}NiSb_4S_{13}$

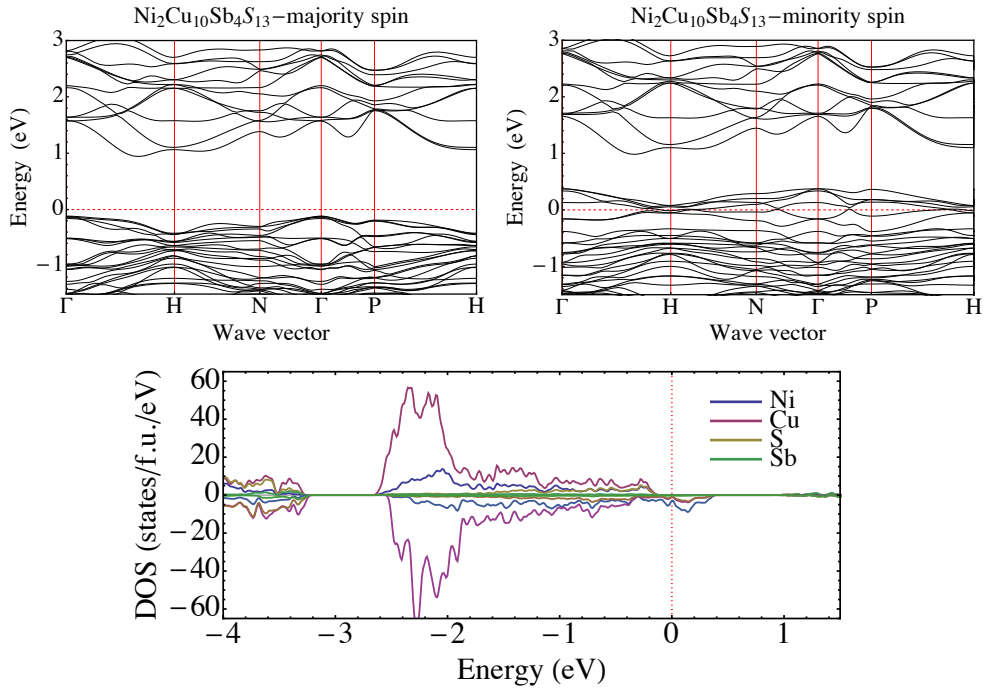

Figure 7.9: Electronic band structure and density of states for $Cu_{10}Ni_2Sb_4S_{13}$

7.3.3 Doped with Transition Metals $Cu_{12-x}M_xSb_4S_{13}$, M=Zn, Fe and Ni

Since stoichiometric $Cu_{12}Sb_4S_{13}$ has two holes per formula unit and ZT can be further optimized via controlling the hole filling, we investigated the doping effect of Zn, Fe and Ni on Cu sites. We studied the energetics of Zn substitution on both the trigonal 12e and tetrahedral 12d sites; the tetrahedral sites were preferred by more than 0.4 eV per substitutional atom. The substitution sites for $Cu_{10}Zn_2Sb_4S_{13}$ were determined by picking the lowest-energy configuration among all symmetry-inequivalent substitutional pairs on the tetrahedral 12d sites. The calculated band structure of $Cu_{10}Zn_2Sb_4S_{13}$ is shown in Fig. 7.6, showing that introduction of Zn leads to complete filling of the valence band states and semiconducting behavior. Since it is expected that the Zn ion will be strictly in the Zn^{2+} state, this is consistent with complete filling of the valence bands and the occurrence of a semiconductor observed in experiment [7].

Fe substitution on the tetrahedral 12d sites are also found to be preferred over the trigonal

12e sites. Spin-polarized band structure for $Cu_{11}FeSb_4S_{13}$ is shown in Fig. 7.7. We find that the majority-spin eg and t2g states are approximately 3 eV below the valence band maximum (VBM), while the minority-spin states fall into the band gap just above the VBM, but below the conduction band states of $Cu_{12}Sb_4S_{13}$. This is mainly due to the exchange splitting between the Fe majority- and minority-spin states of approximately 3 eV. Fe is found to be in the s0d5 high-spin configuration, corresponding to the Fe^{3+} ionic state. Minority-spin eg states lie just above the Fermi level and below t2g states, and are slightly split due to the deviations from perfect tetrahedral symmetry on the 12d sites. The Fe^{3+} ionic state provides an extra electron to fill holes in the valence band compared to each Zn atom, and explains the experimental measurements that Fe substitution causes a larger increase in resistivity for the same doping concentration as Zn [7].

The behavior with Ni doping, however, is quite different. Using DFT calculations, we find that Ni also prefers to substitute for Cu on the tetrahedral 12d sites. Our DFT band structure results for the Ni-doped compound $Cu_{11}NiSb_4S_{13}$ are shown in Fig. 7.8; similar plots are shown for the double-substituted compound $Cu_{10}Ni_2Sb_4S_{13}$ in Fig. 7.9. In our study we assume a ferromagnetic (FM) configuration of the magnetic moments since our calculations for $Cu_{10}Ni_2Sb_4S_{13}$ predict that the antiferromagnetic (AF) spin alignment is 0.1 eV higher in energy than FM. Since the Ni 3d states are only slightly higher in energy than the Cu 3d states, it can be expected that they will strongly hybridize with the valence bands of the host. The majority spin eg and t2g states of nickel indeed lie in the same energy range as the Cu 3d states and are fully occupied. In the minority spin channel, however, three partially empty acceptor-like bands exist above the Fermi level, but these bands overlap with the filled valence bands of the host and there is a finite eDOS at the Fermi level. The total spin is found to be 3/2 per formula unit of $Cu_{11}NiSb_4S_{13}$, giving $S(S + 1) = 3.75$ in good agreement with the effective magnetization values of 3.6 deduced from magnetic susceptibility measurements by Suekuni *et al.* [25] Our results for the double-

substituted $Cu_{10}Ni_2Sb_4S_{13}$ compound in Fig. 7.9 show that the band structures of $Cu_{11}NiSb_4S_{13}$ and $Cu_{10}Ni_2Sb_4S_{13}$ differ by the existence of an additional partially empty minority spin band at the Fermi level, giving a total spin S = 2. Analysis of the partial eDOS curves of the Ni-substituted compounds shows that the partially empty bands are formed by hybridizing Ni 3d states with the p-d hybridized valence bands of the host. Since the number of holes per formula unit varies from 2 for the pure compound (x=0), to 3 for x=1, and to 4 for x = 2, this suggests that each substitutional Ni introduces an additional hole state into the VB of the host. At all Ni concentrations considered, the resulting band structure remains metallic, in agreement with the experimental results of Suekuni *et al.* [26, 27] on Ni-doped tetrahedrite. For comparison, Fe in tetrahedrite acts like a regular dopant whose main effect is to shift the Fermi level, in agreement with experimental measurements [7]. At Fe concentrations x = 1, all valence band holes are filled and the compound becomes electrically insulating, while optimal thermoelectric performance is achieved near x = 0.5 [7]. Here we hypothesize that further optimization of Ni-doped tetrahedrite may be achieved by readjusting the Fermi level close to the top edge of the valence band by addition of Zn and filling the holes introduced by Ni substitution.

7.3.4 Lattice Dynamics

In order to understand the low thermal conductivity in tetrahedrites, we have performed phonon dispersion calcuations using compressive sensing lattice dynamics method and calculations of potential surface of the unstable optical mode at the Γ point and Grünoise parameters. A prominent feature of the phonon dispersion in Fig. 7.10 is the appearance of three harmonically unstable optical phonon branches. The unstable triply degenerate zone-center optical modes involves the out-of-plane vibrations of the three-fold coordinated Cu ions. Fig. 7.10 (b) shows that this mode exhibits double-well structure with symmetrically placed minima at Cu displacements of approximately 0.3 Å away from the planar 12e sites. The depth of the minima in the potential

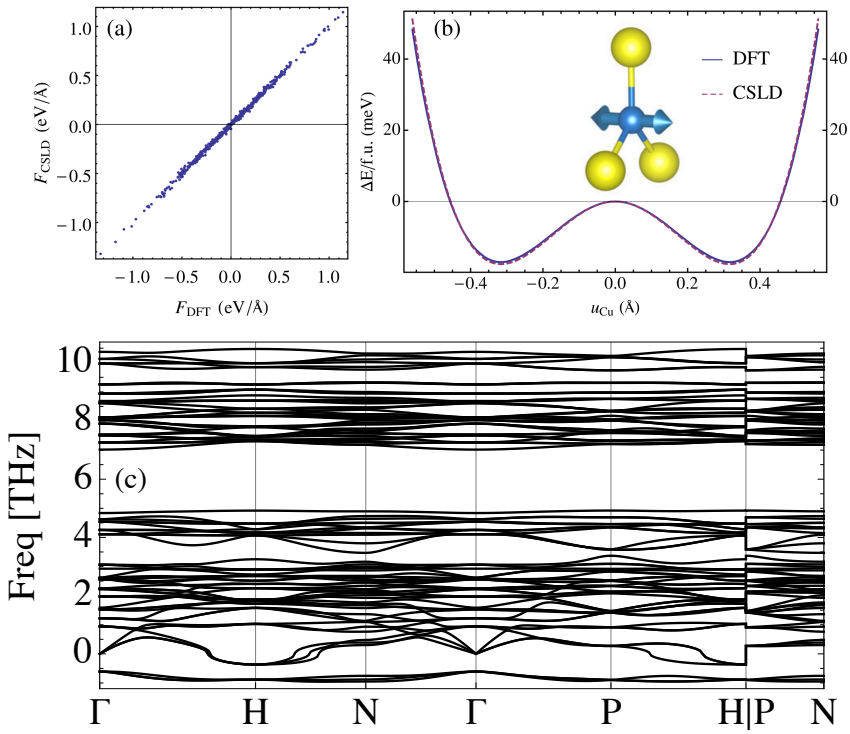

Figure 7.10: Comparison of CSLD predictions with DFT data for tetrahedrite: (a) force at 300 K, (b) relative energy per formula unit of an unstable optical mode involving out-of-plane displacements of trigonally coordinated copper atoms (blue) bonded to sulfur (yellow sphere). DFT and CSLD are shown as solid and dashed lines, respectively. (c) shows the phonon dispersion calculated by CSLD.

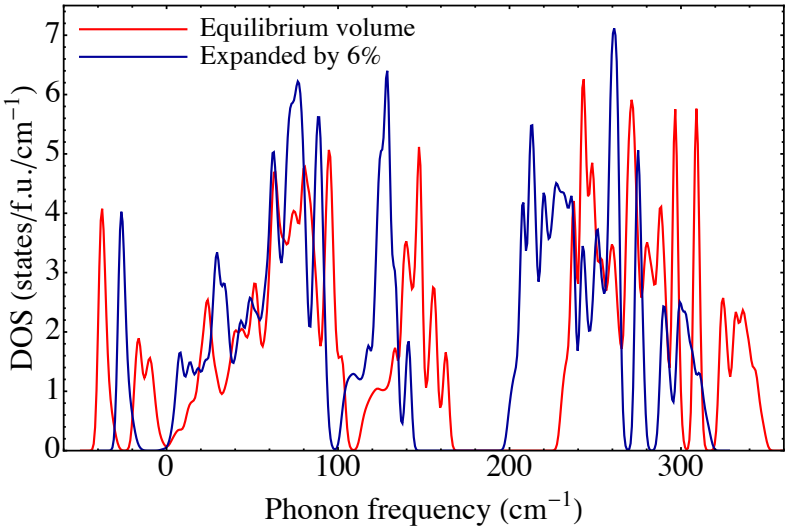

Figure 7.11: Calculated phonon density-of-states at the equilibrium volume V_0 and at $V = 1.06V_0$ for $Cu_{12}Sb_4S_{13}$

energy surface obtained by displacing atoms using the unstable mode eigenvectors are about 20 meV per formula unit. Full structural relaxation starting from the atomic configurations corresponding to these minima resulted in total energy lowering by 80 meV per formula unit, leading to a crystal structure with P1 symmetry. Furthermore, transverse acoustic (TA) branches also become harmonically unstable near the zone-boundary H points. We also computed the Grüeneisen parameter through calculating the volume-dependent vibrational frequencies in Fig. 7.11. We see that the unstable branches involving out-of-plane vibrations of the three-fold coordinated Cu atoms are partially stabilized by lattice expansion, while the higher-lying optical branches exhibit normal mode softening with increasing volume. Instabilities at the zone boundaries of the TA branches are shifted to positive frequencies by 6% volume expansion. The strong frequency shifts towards harmonic stabilization upon increasing volume manifests in high Grüneisen parameters of more than 10 for the TA branches at zone boundaries, indicating highly anharmonic behavior, strong intrinsic phonon scattering and large thermal resistance in these compounds. We hypothesize that significant structural disorder may be induced by freezing-in of those displacements at low temperatures, while at the same time leading to highly anharmonic vibrations and possible anharmonic stabilization of the cubic structure at high temperatures. Together with the possibly formed defects, we further propose that this structural disorder is a major reason for the variable-range hopping type conduction observed in tetrahedrite at low temperatures.

7.4 Conclusions

To summarize, we have carried out a first-principles study of phase stability, electronic band structure, density of states, doping effect and lattice dynamics for $Cu_{12}Sb_4S_{13}$. We found $Cu_{12}Sb_4S_{13}$ is a stable phase at 0 K with possible defects on Cu 12e sites at low temperatures. Copper atoms in $Cu_{12}Sb_4S_{13}$ are all in monovalent Cu^+ state, giving birth to two free hole states

per formula unit of the pristine compound. Zn and Fe substitutions on Cu 12d sites tend to fill the empty hole states while Ni substitution introduce additional hole into the valence band through forming ferromagnetic configuration of the magnetic moments. Calculation of phonon dispersion shows unstable modes for $Cu_{12}Sb_4S_{13}$ at 0 K that are associated with the out-of-plane vibrations of the three-fold Cu ions, which possibly can be stabilized at elevated temperatures. Calculated high Grüneisen parameter indicates the highly intrinsic anharmonicity and therefore explains the extremely low lattice thermal conductivity.

7.5 Acknowledgement

This collaborative work was supported at MSU and UCLA as part of the Center for Revolutionary Materials for Solid State Energy Conversion, an Energy Frontier Research Center funded by the U.S. Department of Energy, Office of Science, Office of Basic Energy Sciences under Award Number DE-SC0001054, and at UM as part of the Center for Solar and Thermal Energy Conversion, an Energy Frontier Research Center funded by the U.S. Department of Energy, Office of Science, Office of Basic Energy Sciences under Award No. DE-SC0000957. Calculations were done using resources of the National Energy Research Scientific Computing Center (NERSC), which is supported by the Office of Science of the U.S. Department of Energy under Contract No. DE-AC02-05CH11231.

References

[1] Steven N. Girard, Jiaqing He, Changpeng Li, Steven Moses, Guoyu Wang, Ctirad Uher, Vinayak P. Dravid, and Mercouri G. Kanatzidis. In situ nanostructure generation and evolution within a bulk thermoelectric material to reduce lattice thermal conductivity. *Nano Letters*, 10(8):2825–2831, 2010. PMID: 20698594.

[2] Bed Poudel, Qing Hao, Yi Ma, Yucheng Lan, Austin Minnich, Bo Yu, Xiao Yan, Dezhi Wang, Andrew Muto, Daryoosh Vashaee, Xiaoyuan Chen, Junming Liu, Mildred S. Dresselhaus, Gang Chen, and Zhifeng Ren. High-thermoelectric performance of nanostructured bismuth antimony telluride bulk alloys. *Science*, 320(5876):634–638, 2008.

[3] Kanishka Biswas, Jiaqing He, Qichun Zhang, Guoyu Wang, Ctirad Uher, Vinayak P. Dravid, and Mercouri G. Kanatzidis. Strained endotaxial nanostructures with high thermoelectric figure of merit. *Nat Chem*, 3(2):160–166, 02 2011.

[4] George Nolas and Glen Slack. Cagelike crystals may soon help to pump heat with electricity and to create electricity with heat. *American Scientist*, 89(2):136, 2001.

[5] D. T. Morelli, V. Jovovic, and J. P. Heremans. Intrinsically minimal thermal conductivity in cubic I-V-VI_2 semiconductors. *Phys. Rev. Lett.*, 101:035901, Jul 2008.

[6] Eric J. Skoug and Donald T. Morelli. Role of lone-pair electrons in producing minimum thermal conductivity in nitrogen-group chalcogenide compounds. *Phys. Rev. Lett.*, 107:235901, Nov 2011.

[7] X. Lu, D.T. Morelli, Y. Xia, F. Zhou, V. Ozolins, H. Chi, X. Zhou, and C. Uher. High performance thermoelectricity in earth-abundant compounds based on natural mineral tetrahedrites. *Adv. Energy Mater.*, doi: 10.1002/aenm.201200650., 2012.

[8] Fei Zhou, Weston Nielson, Yi Xia, and Vidvuds Ozoliņš. Lattice anharmonicity and thermal conductivity from compressive sensing of first-principles calculations. *Phys. Rev. Lett.*, 113:185501, Oct 2014.

[9] Xu Lu, Donald T. Morelli, Yi Xia, and Vidvuds Ozolins. Increasing the thermoelectric figure of merit of tetrahedrites by co-doping with nickel and zinc. *Chemistry of Materials*, 27(2):408–413, 2015.

[10] Xu Lu, Donald T. Morelli, Yuxing Wang, Wei Lai, Yi Xia, and Vidvuds Ozolins. Phase stability, crystal structure, and thermoelectric properties of $Cu_{12}Sb_4S_{13-x}Se_x$ solid solutions. *Chemistry of Materials*, 28(6):1781–1786, 2016.

[11] W. Kohn and L. J. Sham. Self-consistent equations including exchange and correlation effects. *Phys. Rev.*, 140:A1133–A1138, Nov 1965.

[12] P. E. Blöchl. Projector augmented-wave method. *Phys. Rev. B*, 50:17953–17979, Dec 1994.

[13] G. Kresse and J. Hafner. *Ab initio* molecular dynamics for liquid metals. *Phys. Rev. B*, 47:558–561, Jan 1993.

[14] G. Kresse and J. Hafner. *Ab initio* molecular-dynamics simulation of the liquid-metal–amorphous-semiconductor transition in germanium. *Phys. Rev. B*, 49:14251–14269, May 1994.

[15] G. Kresse and J. Furthmüller. Efficiency of ab-initio total energy calculations for metals and semiconductors using a plane-wave basis set. *Computational Materials Science*, 6(1):15 – 50, 1996.

[16] G. Kresse and J. Furthmüller. Efficient iterative schemes for *ab initio* total-energy calculations using a plane-wave basis set. *Phys. Rev. B*, 54:11169–11186, Oct 1996.

[17] John P. Perdew, Kieron Burke, and Matthias Ernzerhof. Generalized gradient approximation made simple. *Phys. Rev. Lett.*, 77:3865–3868, Oct 1996.

[18] John P. Perdew, Kieron Burke, and Matthias Ernzerhof. Generalized gradient approximation made simple. *Phys. Rev. Lett.*, 77:3865–3868, Oct 1996.

[19] S. L. Dudarev, G. A. Botton, S. Y. Savrasov, C. J. Humphreys, and A. P. Sutton. Electron-energy-loss spectra and the structural stability of nickel oxide: An LSDA+U study. *Phys. Rev. B*, 57:1505–1509, Jan 1998.

[20] Jochen Heyd, Gustavo E. Scuseria, and Matthias Ernzerhof. Hybrid functionals based on a screened coulomb potential. *J. Chem. Phys.*, 118(18):8207–8215, 2003.

[21] Jochen Heyd and Gustavo E. Scuseria. Efficient hybrid density functional calculations in solids: Assessment of the heyd–scuseria–ernzerhof screened coulomb hybrid functional. *J. Chem. Phys.*, 121(3):1187–1192, 2004.

[22] Jochen Heyd, Gustavo E. Scuseria, and Matthias Ernzerhof. Erratum: "hybrid functionals based on a screened coulomb potential" [j. chem. phys.118, 8207 (2003)]. *The Journal of Chemical Physics*, 124(21):–, 2006.

[23] B. J. Wuensch and Zeitschrift Kristall. The crystal structure of tetrahedrite, $Cu_{12}Sb_4S_{13}$. *Zeitschrift für Kristallographie*, 119(437), 1964.

[24] A. Pfitzner, M. Evain, and V. Petricek. $Cu_{12}Sb_4S_{13}$: A temperature-dependent structure investigation. *Acta Crystall*, B53(337), 1997.

[25] K. Suekuni, Y. Tomizawa, T. Ozaki, and M. Koyano. Systematic study of electronic and magnetic properties for $Cu_{12-x}TM_xSb_4S_{13}$ (TM = Mn, Fe, Co, Ni, and Zn) tetrahedrite. *Journal of Applied Physics*, 115(14), 2014.

[26] Koichiro Suekuni, Kojiro Tsuruta, Tomoki Ariga, and Mikio Koyano. Thermoelectric properties of mineral tetrahedrites $Cu_{12}Tr_2Sb_4S_{13}$ with low thermal conductivity. *Applied Physics Express*, 5(5):051201, 2012.

[27] Koichiro Suekuni, Kojiro Tsuruta, Masaru Kunii, Hirotaka Nishiate, Eiji Nishibori, Sachiko Maki, Michihiro Ohta, Atsushi Yamamoto, and Mikio Koyano. High-performance thermoelectric mineral $Cu_{12-x}Ni_xSb_4S_{13}$ tetrahedrite. *Journal of Applied Physics*, 113(4), 2013.